Institut für Festkörperphysik E13
Technische Universität München

Nuclear Resonant Scattering for the Study of Dynamics of Viscous Liquids and Glasses

Ilia Sergueev

Vollständiger Abdruck der von
der Fakultät für Physik der Technischen Universität München zur Erlangung
des akademischen Grades eines

Doktors der Naturwissenschaften (Dr. rer. nat.)

genehmigten Dissertation.

Vorsitzender:		Univ.-Prof. Dr. P. Ring
Prüfer der Dissertation:	1.	Univ.-Prof. Dr. W. Petry
	2.	Univ.-Prof. Dr. F. E. Wagner, i.R.

Die Dissertation wurde am 09.12.2003 bei der
Technischen Universität München eingereicht und durch die
Fakultät für Physik am 04.02.2004 angenommen.

Abstract

Nuclear resonant scattering of synchrotron radiation on molecular probes has been employed to study the dynamics of a glass former. Incoherent and coherent scattering have been investigated in theory and applied in experiment in the static case and in the presence of relaxation. The influence of translational and spin relaxation in the pico-to-microsecond time range on relevant observables has been characterized. The measured temperature dependence of these observables gives then information about the liquid-to-glass transition. In particular the combination of coherent and incoherent scattering allowed here to separate translational and rotational dynamics.

Zusammenfassung

Kernresonante Streuung von Synchrotronstrahlung an molekularen Sonden wurde eingesetzt um die Dynamik eines Glasbildners zu untersuchen. Inkohärente und kohärente Streuung wurden im statischen Fall und bei Relaxation theoretisch untersucht und experimentell angewandt. Der Einfluß von Translations- und Spin-Relaxation im Zeitbereich von Piko- bis Mikrosekunden auf wichtige Meßgrößen wurde charakterisiert. Das experimentell bestimmte Temperaturverhalten dieser Größen ermöglicht dann Aussagen über den Flüssig-Glas-Übergang. Insbesondere erlaubte hier die Kombination kohärenter und inkohärenter Streuung Translations- und Rotationsdynamik zu trennen.

List of Abbreviations

APD Avalanche Photo-Diode

DB Dynamical Beat

DBP Dibutyl Phthalate

DOS Density of States

DS Dielectric Spectroscopy

EFG Electric Field Gradient

ESRF European Synchrotron Radiation Facility

FC Ferrocene

FJM Finite Jump Model

HRM High Resolution Monochromator

LGT Liquid-to-Glass Transition.

MCT Mode Coupling Theory

MS Mössbauer Spectroscopy

NFS Nuclear Forward Scattering

NIS Nuclear Inelastic Scattering

NMR Nuclear Magnetic Resonance

NQR Nuclear Quadrupole Resonance

NRS Nuclear Resonant Scattering

PM Premonochromator

QB Quantum Beat

RDM Rotational Diffusion Model

SCM Strong Collision Model

SR Synchrotron Radiation

SRPAC Synchrotron Radiation based Perturbed Angular Correlation

TDI Time Domain Interferometry

TDPAC Time Differential Perturbed Angular Correlation

VFT Vogel-Fulcher-Tammann equation

Contents

1 Introduction **1**

2 Relaxation in glass-forming liquids **5**

2.1 General aspects of the liquid-to-glass transition (LGT) 5

2.2 Temperature dependence of LGT dynamics 9

2.3 Time dependence of the relaxation function 11

2.4 Description of the LGT by the mode-coupling theory 12

2.5 Slow β relaxation 16

3 Nuclear forward scattering (NFS) of synchrotron radiation (SR) **19**

3.1 The Mössbauer effect 19

3.2 Principles of NFS 20

3.3 Theory of NFS in the static case 22

3.3.1 Single resonance 22

3.3.2 Hyperfine splitting 24

3.4 Influence of spatial dynamics on NFS 26

3.4.1 General formalism 27

3.4.2 Debye relaxation 28

3.4.3 Kohlrausch relaxation 30

3.5 Time domain interferometry 34

4 SR-based perturbed angular correlation (SRPAC) **37**

4.1 Spatially coherent versus incoherent nuclear resonant scattering 37

4.2 Principle of SRPAC 40

4.3 Theory of SRPAC in the static case 42

4.4 Influence of spin dynamics on SRPAC 46

4.4.1 Slow relaxation regime 50

4.4.2 Fast relaxation regime 52

4.4.3 Intermediate relaxation regime 54

4.4.4 Short-time dynamics in restricted anglular range 54

4.5 Influence of spatial and spin dynamics on NFS 56
4.5.1 Influence of spin dynamics 56
4.5.2 Influence of spin and spatial dynamics 58

5 Experimental **61**
5.1 Experimental setup 61
5.2 Methodical aspects of SRPAC 63
5.2.1 Dependence on the geometry of the experiment 63
5.2.2 Contributions to 4π scattering produced by NFS 66

6 Study of LGT dynamics by NFS and SRPAC **71**
6.1 Previous studies of the LGT by Mössbauer spectroscopy 71
6.2 The sample 74
6.3 Experiment by SRPAC 76
6.4 Experiment by NFS 84
6.5 Results and discussion 88
6.5.1 Fast dynamics 88
6.5.2 Slow dynamics 93
6.6 Stretched exponential relaxation 97

7 Study of LGT dynamics in restricted geometry by NFS **101**
7.1 Dynamics of viscous liquids in restricted geometry 101
7.2 The sample 102
7.3 Experiment by NFS 102
7.4 Results 107

8 Conclusion and Outlook **111**

A Calculation of the NFS amplitude **115**

B Electric quadrupole interaction **119**

C Calculation of the SRPAC intensity **121**

D Calculation of $G_{22}(t)$ by the eigensystem method **125**

E Calculation of $G_{22}(t)$ by the resolvent method **131**

Chapter 1

Introduction

The understanding of the formation of glasses by slowing down the dynamics of liquids is currently seen as one of the major challenges in condensed matter physics. Moreover, the glassy products formed by this process provide a large variety of important materials which are widely used in nowadays technologies. The dynamics of the liquid-to-glass transition extends over a very wide time window from short time dynamics in the 0.1ps domain to infinitely long times, i.e. in practical terms over more than 14 decades. Different experimental techniques are employed to cover such a large time window. One of them is Mössbauer spectroscopy.

Mössbauer Spectroscopy (MS) is a high-resolution spectroscopic method widespread in solid state physics. It relies on recoilless emission and absorption of nuclear resonant γ-radiation, the probability of which is given by the Lamb-Mössbauer factor. MS is sensitive to dynamics in a ns-μs time window and on a sub-Ångstrom to Ångstrom length scale. These features make it a powerful tool to study the liquid-to-glass transition. The method was successfully applied to study dynamics in soft matter, e.g. in organic glasses, polymers and biological compounds.

After synchrotron radiation (SR) was introduced as a new tool for scientific research, it was suggested to use it for the excitation of Mössbauer nuclei. The first successful nuclear resonant scattering experiment using synchrotron radiation was performed in 1985 in Bragg reflection. Later on, the method of Nuclear Forward Scattering (NFS) was developed which is the coherent analogue of MS on the time scale. It is particularly suited to investigate hyperfine interactions and dynamics. The next step in the development was nuclear inelastic scattering where information about the density of states is directly obtained. Both methods have become highly attractive nowadays due to the excellent, continuously improving characteristics of the available SR sources. Intense X-ray beams with extreme brilliance and almost completely linear polarization allow us to investigate tiny sample volumes and samples under special conditions. Due to the possible small

sample sizes combinations of high pressures, low temperatures and high magnetic fields can be realized, which enable us to investigate the magnetic and electronic properties of solid state matter down to nanoparticles.

However, both MS and NFS are restricted to investigations of materials with non-vanishing Lamb-Mössbauer factor. In particular, the liquid-to-glass transition can be approached by these methods only from the glassy state. This restriction can be overcome by a new method, Synchrotron Radiation based Perturbed Angular Correlation (SRPAC). SRPAC relies on spatially incoherent nuclear resonant scattering of SR and can be considered as a scattering variant of Time Differential Perturbed Angular Correlation (TDPAC). However, in SRPAC the investigated nuclear level is populated not 'from above' (via a cascade as in TDPAC) but 'from below', i.e. from the ground state. The absence of the cascade increases the amount of isotopes which can be investigated. In particular, SRPAC can be applied to the Mössbauer isotopes like ^{57}Fe, ^{119}Sn, ^{61}Ni.

Being single-nucleus scattering, SRPAC does not depend on recoilfree emission and absorption, and not on translational nuclear motion. Therefore SRPAC allows one to continue Mössbauer investigations of hyperfine interactions and rotational dynamics into regions where the Lamb-Mössbauer factor vanishes, i.e. in very soft matter and viscous liquids. It also opens the possibility to investigate high-energy Mössbauer transitions which are otherwise often inaccessible at ambient temperatures due to a vanishing Lamb-Mössbauer factor.

The main aim of this work was to develop the method of SRPAC and to apply the combination of SRPAC and NFS to study dynamics of viscous liquids. This aim includes several tasks:

- Theoretical
  - *Formulation of SRPAC in the static case.* In principle, the theory of angular correlation can be used to describe SRPAC. However, a different way of formation of the investigated nuclear level and the linear polarization of SR require modifications of the theory.
  - *Formulation of the influence of rotational dynamics on SRPAC for the ^{57}Fe nucleus.* The influence of dynamics on angular correlation was studied theoretically very extensively in the 70's in application to TDPAC. However, the large development of the physics of viscous liquids during the last two decades introduced new theoretical approaches, which have to be included. Dynamical aspects of SRPAC are similar to those of nuclear magnetic resonance. The models used in this method can be successfully applied to SRPAC. Further, the spin quantum number of the used isotope can give the possibility to simplify the general theory and sometimes to reduce its results to analytical expressions.

  - *Formulation of the influence of Kohlrausch relaxation on NFS.* The essential property of the dynamics of viscous liquids is the stretching of relaxation. It is usually described by a Kohlrausch relaxation function. The influence of this relaxation on NFS has to be analyzed.

- Experimental

  - *Methodical study of SRPAC.* The experimental realization of SRPAC is completely different compared to TDPAC. A methodical experimental study of SRPAC has to be performed and the optimal experimental setup for studying dynamics has to be found.
  - *Use of SRPAC to study dynamics of the liquid-to-glass transition.* Experiments which show the perspectives and restrictions of SRPAC to study dynamics have to be performed.
  - *Separation of dynamics into pure rotation and translation of the center of mass.* The combination of SRPAC which is sensitive only to the rotational molecular dynamics and NFS which is sensitive to both rotational and translational molecular dynamics gives in principle the possibility to separate these two types of dynamics. A comparison of the translational and rotational molecular motions gives new information about the liquid-to-glass transition.
  - *Study of the liquid-to-glass transition in restricted geometry by NFS.* The study of liquid dynamics in confinement has attracted much interest nowadays. It is believed that confinement may help to address fundamental questions about bulk dynamics. The realization of such an experiment is presented in this work.

The arrangement of this work is the following. Chapter 1 gives a short introduction to the physics of the liquid-to-glass transition. The main features are described and the fundamental mode coupling theory is introduced. Chapter 2 describes NFS. The influence of the relaxation driven by exponential and Kohlrausch relaxation functions on NFS is described. Chapter 3 is dedicated to the theory of SRPAC. Here the static case and the influence of dynamics are described. Additionally, the influence of molecular rotation on NFS which is similar to that on SRPAC is shown. Chapter 4 is dedicated to the description of the experimental setup and to methodical aspects of SRPAC. A study of a glass forming liquid by a combination of SRPAC and NFS is presented in Chapter 5. The obtained results are discussed. The influence of confinement on the liquid-to-glass transition is presented in Chapter 6. Here the same glass forming liquid is used as in the bulk sample. A difference between dynamics in confinement and in the bulk is found and discussed. In Chapter 7 the results are summarized and perspectives of SRPAC are discussed.

Chapter 2

Relaxation in glass-forming liquids

Glass, in the popular and basically correct conception, is a liquid that has lost its ability to flow [Ang95]. However, while glasses form an extremely important class of materials and the glass-forming ability is shared by many different substances, the phenomena underlying the liquid-to-glass transition (LGT) and the nature of the glassy state are not yet fully understood. The main questions that physicists try to solve are:

- Why do certain substances or solutions suddenly undergo a dramatic "slowing down" in the diffusive motions of their particles?
- Why do glasses not form a precisely ordered crystalline material, at some precisely defined freezing point, like other, more "normal" substances?

Those questions also motivated the experiments described in this thesis. A short review will be given in this chapter, describing the following features: general aspects of the LGT, temperature dependence of the dynamics of the LGT, time dependence of the relaxation function, description of the LGT in the mode-coupling theory (MCT) and the slow β relaxation.

2.1 General aspects of the liquid-to-glass transition

The usual way to obtain a glass is fast cooling (quenching) of a liquid. If no crystals are formed during this process, the glassy state is entered when the liquid passes through the liquid-to-glass transition, which is a range of temperatures over which the system "falls out of equilibrium" (In strict equilibrium thermodynamics the viscous liquid is already below melting temperature in a non-equilibrium state). The clearest signature of the approach to the LGT is a huge increase in the viscosity η. Whereas $\eta \simeq 10^{-2} \ldots 10^{-1}$ poise is a typical value for a normal liquid, the glass transition temperature T_g is usually defined as the temperature where η reaches 10^{13} poise [Ang95].

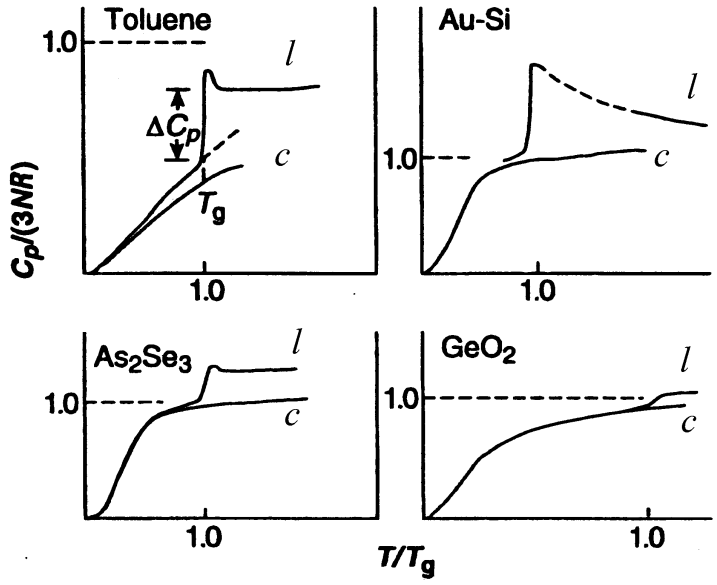

Figure 2.1: Different forms of heat capacity for liquid (l) and crystal (c) phases of several glass formers [Ang95].

In a narrow temperature range around T_g, certain properties of the liquid such as specific volume, enthalpy and heat capacity change abruptly. The dependence of the heat capacity C_p on temperature is shown in Fig. 2.1 for several glass formers [Ang95]. It is seen that the heat capacity changes from a liquid-like to a crystal-like value at the region around T_g. This phenomenon can be used for another definition of T_g as the temperature of a discontinuity of C_p. For slow cooling rates or typical observation time of $100 - 1000$ s both definitions give similar values for T_g. Therefore T_g is also called the caloric glass transition temperature. The first conclusion from the behavior of the heat capacity would be that there is a second-order phase transition at T_g. However, no discontinuity in the behavior of the viscosity is observed at this temperature. To explain this contradiction we consider qualitatively the dynamics of a liquid during cooling. A normal liquid can be visualized as a large collection of tiny particles that are in a state of ceaseless violent motion. Chaotic trajectories bring particles into collision with neighboring particles. On the average, the collisions result in a reversal of the trajectories of the particles, so they appear to be rattling in the cage formed by their neighbors with a characteristic time τ_l. But sometimes changes of the relative positions occur and the particle jumps out from the cage to another position that becomes the new center of the rattling motion. Such a structural relaxation or diffusive motion occurs with a characteristic time τ_r. In the normal liquid the rattling motion and the structural relaxation occur with similar characteristic times. It is difficult to separate them, therefore it is reasonable to assume that the particles are undergoing continuous diffusion.

As the temperature decreases below the melting temperature T_m, the liquid becomes supercooled. The packing becomes more dense and the particle spends more time rattling in the cage. Structural relaxation requires that an increasing number of neighbors has to cooperate in order to enable the particle to jump out of the cage. While the characteristic rattling time τ_l changes only slightly, the structural relaxation time τ_r increases drastically. The essential feature of the LGT is that an enormous gap opens between τ_l and τ_r. The difference between these two time scales can change by up to ten orders of magnitude in the temperature range from 1.1 T_g to T_g.

The reaction of the substance to external stress, which is a value that is measured in experiments, consists of two parts well separated in time: crystal-like reaction in time τ_l and liquid-like reaction in time τ_r. Each experiment has a characteristic time scale, given by the time t_e, to probe the system and to observe the results. For heat capacity measurements, t_e may be of the order of 100 s. The result of the experiment depends on the ratio between t_e and τ_r. If t_e is long compared with τ_r, then a liquid-like reaction will be seen in the experiment, in the opposite case a crystal-like behavior will be observed. From the point of view of heat capacity measurements we can say that T_g is defined as the temperature where the structural relaxation time becomes larger than 100 s. Viscosity, on the other hand, depends only on structural relaxation and can be observed as such on any time scale. That is why no abrupt change of the temperature dependence of the viscosity is observed in the region of T_g.

The main result of these considerations is that the LGT is not a phase transition but rather a kinetic transition to the state where the system is not in equilibrium any more. In statistical mechanics the idea of ergodicity is introduced for such systems. When a system is in the thermodynamical equilibrium it is called ergodic, otherwise it is called non-ergodic.

As one can see T_g is not only a characteristic feature of a substance but strongly depends on the experiment. The question is, whether any temperature exists that separates crystal-like and liquid-like states of the substance, thus being a characteristic property of the substance. The results of this thesis may help to answer that question.

One of the possible candidates for such a universal temperature results from thermodynamic considerations. It is the Kauzmann temperature T_K, which appears in the behavior of the thermodynamical parameters of a substance, e.g. of the entropy. The entropy of a supercooled liquid has a larger value than that of the corresponding crystal state at the same temperature. The excess entropy, called the entropy of fusion, comes from the additional freedom of motion in a liquid as compared to a crystal. The dependence of the entropy of fusion on temperature is shown in Fig. 2.2. It decreases with decreasing temperature. It is not possible to measure the equilibrium liquid entropy below T_g, but the extrapolation shows that below some temperature the entropy of fusion

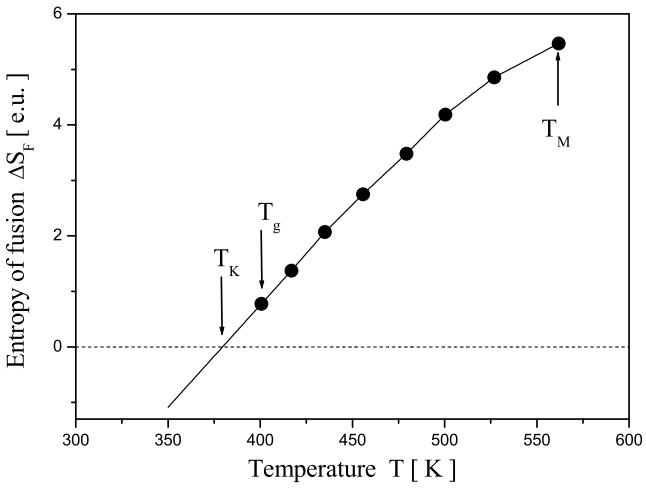

Figure 2.2: Difference between liquid and crystalline state entropy for lithium acetate as a function of temperature [WA76].

becomes negative. The vibrational and rattling contribution to the entropy of a glass and the vibrational contribution to the entropy of a crystal are nearly the same, and the entropy of a glass can not be smaller than that of a crystal. As a consequence the entropy must deviate significantly from the extrapolation line through data shown in Fig. 2.2. The temperature where the entropy of fusion apparently becomes negative is called the Kauzmann temperature T_K [Kau48, Ang95].

Another possible universal temperature is obtained from kinetic considerations. It is the crossover temperature T_c first introduced by Goldstein [Gol69] in 1969 and now strongly reinforced by mode-coupling theory [GS92, Göt99]. T_c is located in the supercooled region above T_g. When particles in a liquid are packed more closely with decreasing temperature, the transport of a particle out of the cage becomes more and more difficult. At the crossover temperature structural relaxation and rattling in the cage decouple and seen from the time scale of rattling the particle is frozen inside the cage. For $T < T_c$ another mechanism of diffusion becomes important. It is the thermally activated hopping that defines structural relaxation below T_c. One experimental evidence for the significance of the crossover temperature is the decoupling of different modes of motion below T_c. There is no reason for the activation energy for diffusion connected with hops of a single particle to be the same as the activation energy for the viscosity, which is related to the motion of many particles. Fig. 2.3 shows an example of such decoupling in the organic glass former o-terphenyl. The translational diffusion coefficient, which is proportional to the corresponding relaxation time, is shown together with the viscosity scaled to have the same behavior in the normal liquid regime [FGSF92]. The crossover temperature T_c for

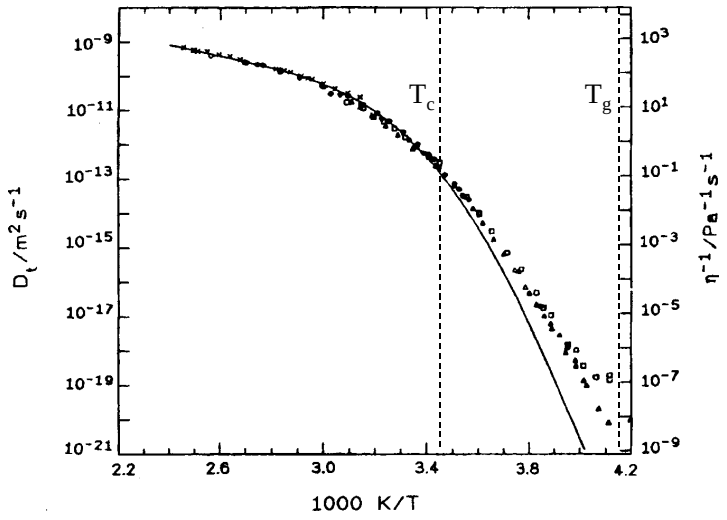

Figure 2.3: Translational diffusion coefficient measured by various techniques (•, △, □, △) and the inverse viscosity (solid line) as functions of temperature for o-terphenyl [FGSF92]; $T_c = 290$ K, $T_g = 240$ K.

this system was determined independently by neutron scattering [PBF$^+$91]. The viscosity and the translational diffusion constant coincide in the high temperature region, so they are governed by the same transport mechanism. But near T_c they decouple, and at T_g their difference becomes two orders of magnitude. The same phenomenon was demonstrated recently in metallic glasses [ZRFM03].

2.2 Temperature dependence of LGT dynamics

The main parameter of the LGT dynamics is the structural relaxation time τ_r which is associated with transport or relaxation processes. The viscosity η is a measure of the liquid response to a suddenly imposed shear stress and is related to the corresponding relaxation time by the so-called Maxwell equation [CLH$^+$97]:

$$\eta = G_\infty \tau_r \tag{2.1}$$

where G_∞ is the high-frequency shear modulus, an elastic property of a liquid. Therefore the temperature dependences of viscosity and relaxation time are the same for an appropriate scaling factor G_∞.

The easiest way to introduce a temperature dependence of relaxation is to consider relaxation as a thermally activated process. The particle can jump from one site to another if its thermal energy exceeds the energy barrier between two sites. The simplest approach to describe the relaxation time for such thermally activated process is

$$\tau_r = \tau_l \exp(\Delta E / k_B T) \tag{2.2}$$

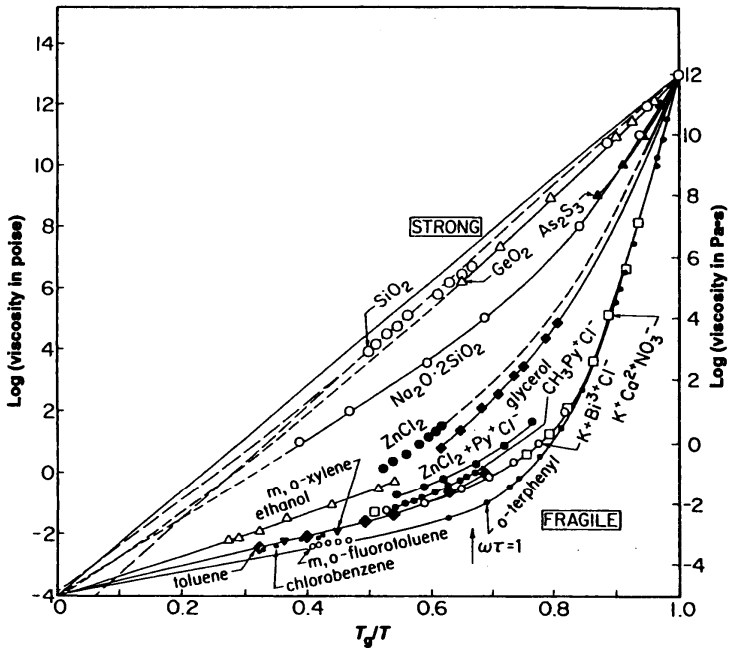

Figure 2.4: T_g scaled Arrhenius plots for viscosities of different glass-forming liquids showing the spread of the data between the strong and fragile extremes [ANM+00].

where ΔE means the barrier energy, k_B is the Boltzmann factor and τ_l is the characteristic relaxation time in a normal liquid. This is the universal Arrhenius law of diffusion that is used in many thermodynamic applications.

As it was observed in many glass-forming liquids, the temperature dependence of the viscosity deviates from the Arrhenius behavior as it is seen in Fig. 2.4 [ANM+00] where all substances are scaled in temperature by T_g (so called Angell plot of viscosity). Open network liquids like SiO_2 show Arrhenius variation of the viscosity (or structural relaxation time) between T_g and the high temperature limit and provide the "strong" liquid extreme of the pattern. Other glass forming liquids, characterized by simple non-directional Coulomb attractions or by van der Waals interactions, mainly organic liquids, provide the other extreme, "fragile" liquids. In fragile liquids, the viscosity varies in a strongly non-Arrhenius fashion between the high and low limits. The strong/fragile-liquid pattern is used as a basis to classify glass-forming liquids.

The most frequently applied equation to describe the deviation of the temperature dependence of the structural relaxation time from an Arrhenius law is the phenomenological Vogel-Fulcher-Tammann(VFT) equation

$$\tau_r = \tau_l \exp[DT_0/(T - T_0)] \tag{2.3}$$

where D and T_0 are phenomenological parameters. The VFT equation often fits τ_r over a considerably wide temperature range, but in almost no case over the full temperature

range from T_g to T_b (boiling temperature). Choosing an appropriate fitting range T_0 can be found to be within 2% of the Kauzmann temperature [Ang91]. The parameter D controls how closely the system obeys the Arrhenius law which corresponds to $T_0 \to 0$ and $DT_0 \to \Delta E/k_B$. D for a set of different glass-forming liquids is given in [BNAP93], it varies from 150 for the strongest network liquids SiO_2 and GeO_2 to 1.5 for polymer melts.

MCT derives another equation to describe the transport properties or the structural relaxation time

$$\tau_r = A\left(\frac{T - T_c}{T_c}\right)^{-\gamma} \tag{2.4}$$

where γ will be defined in the section 2.4. This equation is applied for liquids in the highly fluid to moderately viscous regime near the crossover temperature T_c (see section 2.4).

2.3 Time dependence of the relaxation function

Next in importance to the characteristic time of structural relaxation τ_r is the function which describes the relaxation process. Usually in spectroscopic methods the self-correlation function $F_s(t)$ is used for this purpose:

$$F_s(t) = \langle A(0)A(t)\rangle \tag{2.5}$$

It describes the relaxation of the dynamical variable $A(t)$ (a quantum operator in general) between time zero and a later time t. Physically, $F_s(t)$ measures the relaxation time over which the variable A retains its own memory until this memory is averaged out by statistical randomness. The position of a molecule or its orientation can be chosen as A. In the simplest case the structural relaxation function is an exponential, and a unique time τ_r characterizes the process. In viscous liquids and glasses, however, exponential responses are stretched to longer times, and the process has to be characterized by a more complex function. The most common way to describe the time dependence of the structural relaxation is the Kohlrausch function [Koh47]

$$F_s(t) = f\exp\left[-(t/\tau_r)^{\beta}\right] \tag{2.6}$$

where β is a stretching parameter with $0 < \beta \leqslant 1$ and f is a scaling factor that reflects the presence of faster processes which precede the structural relaxation. This function is empirical, and the physical meaning of β and its correlation with D are under debate. Another important question is whether β is a universal feature of the substance and whether it stays constant with temperature or not. The time-temperature superposition principle, introduced by Ferry [Fer50] and reinforced by MCT, says that changing T or other control parameters like density results in changing only the scale τ_r of the structural

relaxation process but not its functional form. Then the relaxation functions for different temperatures can be collapsed to one master curve

$$F_T(t) = \hat{F}_s(t/\tau_r(T)) \tag{2.7}$$

For the case of a Kohlrausch function, that implies that β stays constant with changing temperature.

From another point of view, there are some experiments showing that β increases monotonically with increasing temperature and approaches unity in the normal liquid regime [DWN+90, ANM+00].

2.4 Description of the LGT by the mode-coupling theory

Mode coupling theory, an outgrowth of the kinetic theory of liquids, was first proposed in 1984 [BGS84, Leu84] to explain the LGT. MCT is a fundamental physical theory that describes the behavior of glass-forming liquids and explains many properties of the LGT (for a review see [GS92, Göt99]).

As it was mentioned before, the motion of a particle in a liquid can be separated into two parts: the rattling inside the cage and the diffusion out of the cage (structural relaxation). This separation is defined by the time scale. At a short time scale a free particle rattles in a cage with the characteristic time of the liquid dynamics $\tau_l \simeq 10^{-12} \dots 10^{-14}$ s. This one-particle process is described by an exponential decay of the relaxation function. Coming from one particle to clusters of particles, one can consider their dynamics in the cage of their neighbors. This is again a local process, since there is no transport of particles out of the cage. Such cluster dynamics is presented as a long-time, stretched tail of the one-particle rattling. This process is called fast β relaxation and is defined by the time τ_β. The diffusion out of the cage requires cooperative motion of the neighbors of the particle. It results in the structural α relaxation with characteristic time τ_r. This process is not exponential and, as it was mentioned before, can empirically be described by a Kohlrausch stretched-exponential function. As a result the relaxation function consists of two steps: the microscopical relaxation towards the fast β relaxation tail and the structural α relaxation (see Fig. 2.5).

In the normal liquid regime, no cages can be formed during time τ_l and α and fast β relaxations have the same time scale. With decreasing temperature (increasing the packing density of particles) time scales start to diverge from each other. There is a critical temperature T_c, and that is the main point of the basic version of MCT, where this divergence becomes infinite. The particles would be frozen in their cages. Therefore

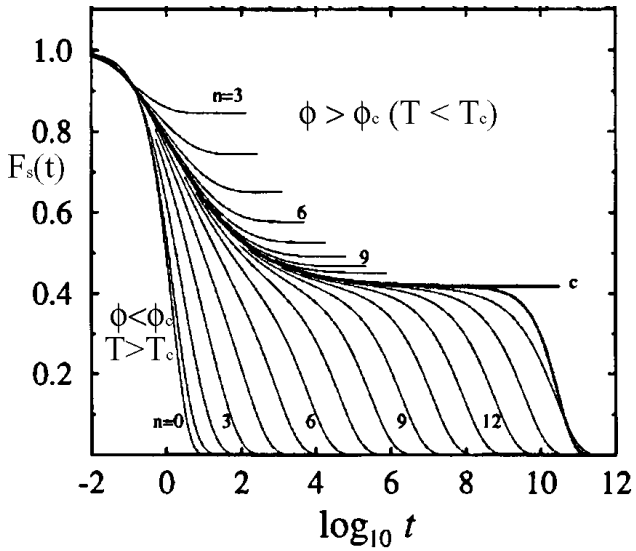

Figure 2.5: Relaxation function as function of $\log_{10} t$ calculated for different packing fractions ϕ [FFG+97] which can be associated with temperatures T [FFG+97]. The thick curve labels the critical fraction ϕ_c. Number n shows deviation from ϕ_c from both sides: $\phi = \phi_c(1 \pm 10^{-n/3})$.

at $T \leqslant T_c$ the relaxation function decays not to zero but to some finite value defined by fast β relaxation (see Fig. 2.5). This value is called the glass form factor or non-ergodicity parameter f. It can be identified with the Debye-Waller factor f_Q or the Lamb-Mössbauer factor f_{LM}. Above but near the critical temperature the step connected with α-relaxation exists, and it is well separated from the step connected with fast β-relaxation by a plateau of height f with a width that decreases with increasing temperature. Here f can be identified with the Debye-Waller factor as measured on inelastic neutron spectrometers with an energy resolution in the order of μeVs or with the Lamb-Mössbauer factor in Mössbauer spectroscopy since it does not take into account the long-time α relaxation. The temperature behavior of f near T_c depends on the deviation of the temperature from T_c and can be described using $\sigma = (T_c - T)/T_c$ as

$$f = \begin{cases} f^c + h\sqrt{\sigma} & T < T_c \\ f^c & T > T_c \end{cases} \tag{2.8}$$

where f^c is a critical glass form factor defined mainly by the experimental scattering vector and h is a critical amplitude. An experimental observation of the temperature behavior of the Debye-Waller factor is shown in Fig. 2.6 [TSWF97]. The square root anomaly is seen for various values of the scattering vector at the same temperature $T_c \approx 290$ K.

MCT predicts a fractal time dependence of the relaxation function in the region close

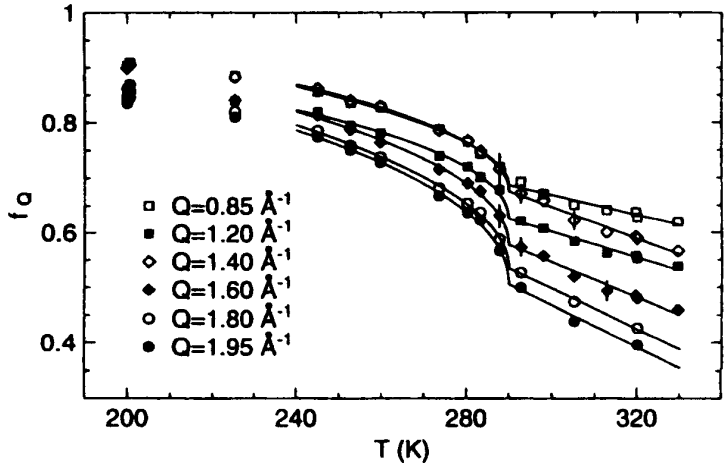

Figure 2.6: Effective Debye-Waller factors f_Q of o-terphenyl as functions of temperature T for various wave vectors Q by coherent neutron scattering spectroscopy [TSWF97]. The curves indicate fits leading to a critical temperature $T_c \approx 290$ K.

to the plateau for both steps of relaxation:

$$F_s(t) \approx f + h\left(\frac{t}{\tau_\beta}\right)^{-a} \text{ for } \tau_0 \ll t \ll \tau_r \tag{2.9}$$

$$F_s(t) \approx f - h\left(\frac{t}{\tau_r}\right)^{b} \text{ for } \tau_\beta \ll t \text{ and } T > T_c \tag{2.10}$$

where a and b are critical exponents. They are determined by the system-dependent parameter λ as

$$\lambda = \frac{\Gamma^2(1-a)}{\Gamma(1-2a)} = \frac{\Gamma^2(1+b)}{\Gamma(1+2b)} \tag{2.11}$$

where Γ denotes the gamma function. One can see that the time-temperature superposition principle is valid for both steps of relaxation. Relaxation functions for different temperatures can be collapsed to one master curve for fast β relaxation and separately for α relaxation. The characteristic times for both steps of relaxation are determined by the relative deviation σ from T_c and by the critical exponents

$$\tau_\beta \propto |\sigma|^{-1/2a} \tag{2.12}$$

$$\tau_r \propto |\sigma|^{-\gamma},\ \gamma = \frac{1}{2a} + \frac{1}{2b} \tag{2.13}$$

The second equation has been presented already in connection with the temperature dependence of structural relaxation. The fit of the temperature dependence of the viscosity, which is proportional to τ_r, by a power law is shown in Fig. 2.7. The important result of the MCT is that both the temperature dependence of the relaxation times and the time dependence of the relaxation function are determined by two system-dependent parameters: λ and T_c.

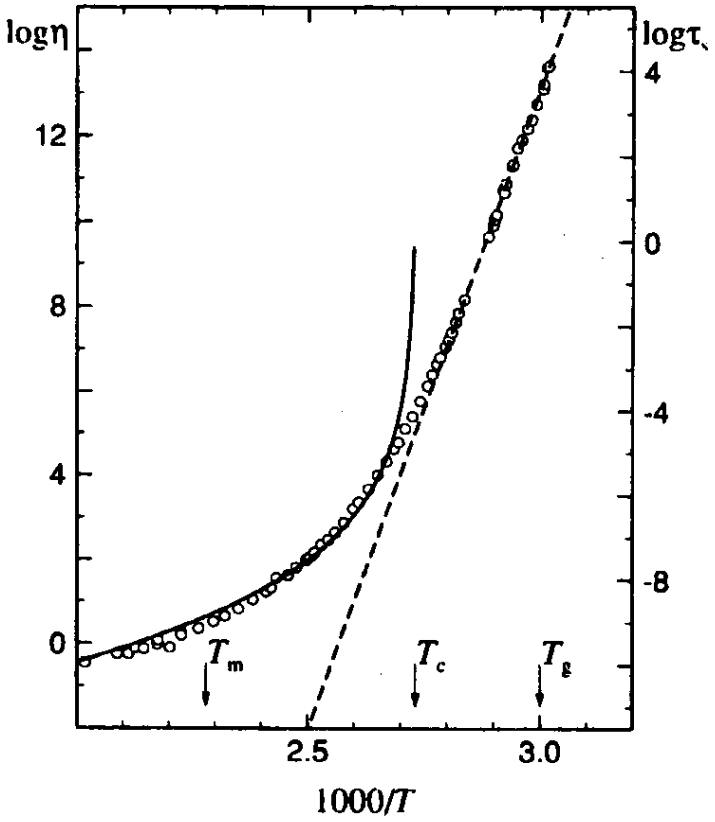

Figure 2.7: Arrhenius plot of viscosity η in Poise of the mixed salt $0.4Ca(NO_3)_2 \cdot 0.6KNO_3$. The dashed line is a fit by an Arrhenius law. The full line represent a power law (see text) with $\gamma = 4.06$. Experimental data was obtained by [WBM69] and fit was done by [GS92].

A weak point of the basic MCT is that it predicts a complete arrest of α relaxation for temperatures below T_c which is not observed in experiments. Extended versions of MCT were elaborated to avoid these difficulties. In this theory the particle can participate, together with kinetic motion, in thermal hopping diffusion which results in avoiding the critical behavior at T_c. The ratio of hopping and kinetic mobility defines the behavior of the supercooled liquid at the region around T_c. Below T_c only thermally activated diffusion has to be taken into account. Then the temperature dependence of the characteristic relaxation times can be qualitatively described by an Arrhenius law for $T < T_c$(see Fig. 2.7). The hopping mobility defined by the energy barrier could be different for different types of motion, resulting in the absence of a universal time scale for the region below T_c.

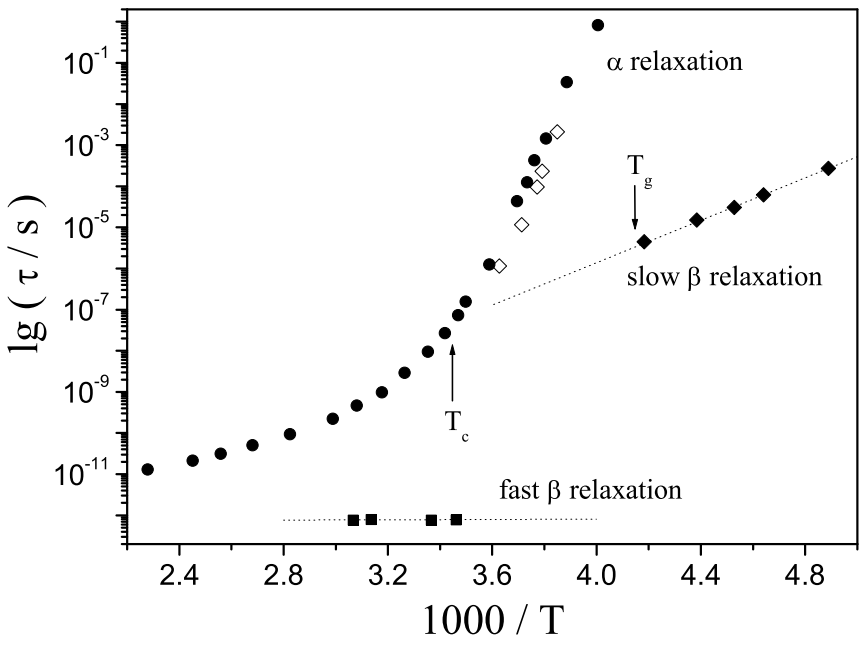

Figure 2.8: Temperature dependence of the various relaxation times for o-terphenyl. α relaxation: dielectric relaxation (◊), nuclear magnetic resonance (•); slow β relaxation: dielectric relaxation (⧫); fast β relaxation: neutron scattering (■). Lines are guides for the eye. Data were taken from [EAN96].

2.5 Slow β relaxation

In addition to the structural relaxation, another relaxation process was found at temperatures near and below T_g. This process, slow β relaxation, was observed for many glass formers including polymers and organic low-molecular weight compounds. The β process is observed usually in the kHz frequency range. Its temperature dependence is well described by an Arrhenius law. The temperature dependence of the relaxation rate of the slow β relaxation is shown in Fig. 2.8 for the typical glass former o-terphenyl.

The origin of slow β relaxation is not yet understood. Several authors suggest intramolecular motion as a source of the β process [Wu91, EAN96, ARCF96]. This explanation works well in the case of polymers. However, it can not explain the β process in glass formers consisting of rigid molecules. The systematic study of simple molecular glass formers by Johari and Goldstein [JG70, Joh73] let them conclude that the slow β relaxation is an intrinsic property of glasses. They considered it to be due to localized motions in the regions of loose packing of molecules in the disordered structure. This model assumes that slow β relaxation is a precursor of structural α relaxation. This idea

was used in MCT together with the name "β relaxation". However, the experimental study shows that the fast β relaxation which is observed in the GHz frequency range and slow β relaxation are different processes and the explanation which was suggested by Johari and Goldstein corresponds to the fast β relaxation. The understanding of the molecular nature of slow β relaxation is therefore still an open question.

The experimental study of the slow β relaxation is difficult due to a lack of proper experimental techniques to access various types of molecular dynamics with microscopic space resolution and sensitivity to slow dynamics. The most commonly used dielectric spectroscopy and NMR follow mainly the reorientation of molecules and do not provide an atomic-scale space resolution. Complementary information on translational relaxation on a molecular length scale can be obtained with neutron scattering. However, it hardly can access the time region above $\sim$1 ns, therefore only few measurements have been reported [ARCF96].

Chapter 3

Nuclear forward scattering (NFS) of synchrotron radiation (SR)

The purpose of this chapter is to introduce the method of nuclear forward scattering (NFS). At first the Mössbauer effect, which is the basis of nuclear resonant scattering, is described. Then the principles of NFS are introduced. NFS in the static case, when the evolution of the nuclear ensemble is governed by a time independent Hamiltonian, is described in the third part. The next section is devoted to the influence of spatial dynamics on NFS. In particular, the influence of Kohlrausch relaxation has been developed. In the last part the application of NFS to study dynamics in non-resonant samples is briefly described.

3.1 The Mössbauer effect

The Mössbauer effect is the recoil-free emission or absorption of nuclear gamma radiation. It was discovered by Rudolf L. Mössbauer in 1958 [Mös58]. A γ-quantum emitted in the de-excitation of a nucleus bound in a solid can be absorbed by another nucleus of the same kind and excite it in a resonant way.

The classical point of view implies that the emission of a γ-quantum is connected with a recoil of the nucleus in order to conserve momentum. If E_0 is the energy of the excited state then the energy of the γ-quantum is $E_\gamma = E_0 - E_R$. From energy and momentum conservation the recoil energy E_R of a free nucleus can be calculated as

$$E_R = \frac{E_\gamma^2}{2Mc^2} \tag{3.1}$$

where M is the mass of the nucleus. Similarly, when a γ-quantum is absorbed it loses the energy E_R due to recoil of the nucleus. In order to find whether resonant absorption will occur in spite of the losses due to recoil, the energy gap $2E_R$ has to be compared to the

sharpness Γ_0 of the absorption (emission) process. This value is related to the life time τ_0 of the excited state by Heisenberg's uncertainty principle:

$$\Gamma_0 = \frac{\hbar}{\tau_0} \tag{3.2}$$

Typical values for the life time are $10^1 - 10^3$ ns ($\tau_0 = 141$ ns for the ^{57}Fe), and accordingly Γ_0 is of the order of $10^{-7} - 10^{-9}$ eV. The recoil energy depends strongly on the energy of the γ-quantum, which is rather large ($E_\gamma = 14.4 \cdot 10^3$ eV for the ^{57}Fe). Then the energy shift $2E_R$ is of the order of $10^{-3} - 10^{-2}$ eV, which is five orders of magnitude larger than the line width Γ_0. Consequently, the resonance condition can not be fulfilled for free nuclei.

The situation is different when emitter and absorber nuclei are bound in a solid. As the binding energy E_B of atoms is of the order of eV, the nuclei cannot recoil freely ($E_R \ll E_B$), but only with creation or annihilation of phonons. The quantum mechanical concept implies that there is a probability for the nuclei to emit (absorb) γ-quanta without phonon excitations and, as a consequence, without change of energy. The energy of the γ-quantum is $E_\gamma = E_0$, the same for emission and absorption, and the resonance process can occur. The probability of the emission without recoil is called the recoilless fraction or Lamb-Mössbauer factor f_{LM}. Recoilless (zero-phonon) emission, absorption, and scattering of nuclear γ radiation is used in Mössbauer spectroscopy (MS).

3.2 Principles of NFS

The main line of development of MS was absorption spectroscopy. Here the ensemble of nuclei manifests itself as a set of independent scatterers. Therefore no information about the collective state of the nuclei (relative phases of the nuclei in the ensemble) can be obtained. Nevertheless, the unique small ratio of line width of the excited level Γ_0 to the transition energy E_0 attracted attention to the possibility of realizing coherent effects in the ensemble of Mössbauer nuclei. It demands another type of experiment - the scattering of γ-quanta by an ensemble of nuclei. The theory of nuclear resonant scattering (NRS) was introduced and developed mainly by Kagan, Afanas'ev and Kohn and Trammell and Hannon in the 60's and 70's; for recent reviews see [Kag99, HT99]. The first attempts to observe coherent phenomena in an ensemble of nuclei were done with traditional Mössbauer sources; for a review see [Smi86]. After synchrotron radiation (SR) was introduced as a new tool for scientific research, it was suggested by Ruby [Rub74] to use it for exciting Mössbauer nuclei. The first successful nuclear resonant scattering experiment using SR was performed by Gerdau et al. [GRW$^+$85] in 1985. This experiment was done in Bragg reflection geometry from a single crystal of yttrium iron garnet.

During the next 6 years investigations of resonant scattering in Bragg and Laue geometry attracted worldwide interest. These measurements, however, required single crystals of high quality, enriched in the Mössbauer isotope (e.g. ^{57}Fe), and exhibiting pure nuclear Bragg reflections. These restrictions on the sample material were removed by using nuclear forward scattering (NFS). NFS was observed for the first time by Hastings et al. [HSvB$^+$91] in 1991. NFS opens the way to study a wide range of materials. In particular relaxation and diffusion were investigated in crystalline, biological and glassy samples [MFW$^+$97, TW99, LW99, VS99, ASF$^+$01].

Nuclear resonant scattering of SR by a single nucleus is a process which can be separated into two stages. Due to the short duration of the SR pulse compared to the excited state lifetime τ_0, the pulse creates an excited nuclear state. The second stage is the decay of this state with re-emission of radiation. The time evolution of the observed scattered radiation is described by a natural decay, i.e., an exponential decay with the lifetime τ_0. Time-independent hyperfine interactions (electric quadrupole interaction and magnetic dipole interaction) between the nucleus and the surrounding electrons split the nuclear states into several sub-levels, which lead to indistinguishable scattering paths. This results in a modulation of the exponential decay of the scattered intensity by a temporal interference pattern called quantum beat (QB).

The scattering by an ensemble of nuclei becomes more complicated. An incoming photon can now interact with any nucleus in the ensemble. In the case of elastic scattering of a photon, where the intrinsic state of the scattering system stays unchanged, it is impossible to ascertain which nucleus in the ensemble was excited. As a consequence, a collective state of the ensemble is involved in the scattering process. The collective state formed after absorption of the photon is called nuclear exciton. The nuclear ensemble behaves like a macroscopic resonator whose properties differ qualitatively from those of the individual nuclei. This shows up by changes of the time and space distribution of the scattered intensity.

When the excitation is distributed over the entire nuclear ensemble, interference between wavelets re-radiated by the nuclei occurs and a coherent radiation field is built up. The scattering of the photon by the entire nuclear ensemble is the spatially coherent channel of scattering, whereas the incoherent channel is formed by scattering on the individual nuclei. Due to the usual property of the coherent scattering, the intensity of scattering is proportional to the square of the number of nuclei. Another property is that an angular interference pattern of scattering appears. Fully constructive interference occurs in the case of an ordered ensemble of nuclei in all directions where the wavelets are in phase. In the case of the disordered ensemble of nuclei, like glasses and liquids, which are subject of interest in this work, constructive interference appears only in the forward direction of scattering. The spatially coherent nuclear resonant scattering in the forward direction is

called nuclear forward scattering.

3.3 Theory of NFS in the static case

Usually the amplitude (intensity) of NFS is calculated in the frequency domain [KAK79]. Here the scattering amplitude is defined as a function of energy. After that, using the δ-function shape of the SR pulse, the Fourier transformation of the scattering amplitude can be performed resulting in the time-dependent amplitude of the scattered radiation. However, in order to emphasize the dynamical aspects of NFS, we use a method which allows to calculate the amplitude straightforward in the time domain. This method has been developed by Shvyd'ko [Shv99a, Shv99b]. The intensity equals to the square of the scattered amplitude which can be written as a sum (see eq. (2.34) in [Shv99b])

$$E(t) = \sum_{k=1}^{\infty} (-1)^k \frac{\xi^k}{k!} E^{(k)}(t) \tag{3.3}$$

where $\xi = \sigma_0 N_0 L/4$ is named the effective thickness in this work. It is proportional to the resonance cross section σ_0, the number of the resonant nuclei per unit volume N_0, and the real thickness L of the target. Each term $E^{(k)}(t)$ corresponds to a channel of scattering with k collision events between the photon and the nuclear ensemble. This term is given by the recursion relation (see eq. (2.36) in [Shv99b])

$$E^{(1)}(t) = \frac{E_0}{\tau_0} K(t,0) \tag{3.4}$$

$$E^{(k+1)}(t) = \frac{1}{\tau_0} \int_0^t \mathrm{d}\tilde{t} \cdot E^{(k)}(\tilde{t}) \cdot K(t,\tilde{t}) \tag{3.5}$$

where $E_0 = \sqrt{I_0/\Delta\omega}$ is the amplitude of the electromagnetic wave coming to the target from the SR source within the frequency band $\Delta\omega$ determined by the monochromator, I_0 is the corresponding intensity and $K(t,\tilde{t})$ is the self-correlation function which takes into account the change of spin and spatial states of the nuclear ensemble in the scattering event. In this work we assume that the time evolution of the nuclei is governed by time-independent or stochastic forces. Then, the exact dependence of the self-correlation function on t and $\tilde{t}$ reduces to the dependence on their difference $K(t,\tilde{t}) \to K(t-\tilde{t})$.

3.3.1 Single resonance

In this section we assume that the nuclear ensemble is in the static state, i.e., the spatial position of each nucleus is fixed and does not change with time. If we also assume the absence of hyperfine interactions (single resonance case) then the self-correlation function

reduces to (see eq. (2.42) in [Shv99b])

$$K(t) = \mathrm{e}^{-t/2\tau_0} \tag{3.6}$$

that reflects the decay of the excited state. Inserting this expression for the self-correlation function into eqs. (3.4) and (3.5) gives the possibility to obtain the amplitude of the scattered radiation. At first, we consider the single scattering (kinematical) approximation of the amplitude which is very convenient for the analysis of physical problems. This approximation is obtained by retaining only the first term in the general solution (3.3). The intensity, which is the square of the amplitude, is given as

$$I(t) = \frac{I_0}{\Delta\omega}\,\frac{\xi^2}{\tau_0^2}\,\mathrm{e}^{-t/\tau_0} \tag{3.7}$$

The time evolution of the delayed intensity is described by a natural decay with the lifetime τ_0.

Also an exact analytical solution of eq. (3.3) which takes into account multiple scattering of the photon by the nuclear ensemble, can be obtained for the single resonance. The integration in eq. (3.5) can be done analytically and one obtains for the amplitude the well known result [KAK79]

$$E(t) = E_0\,\frac{\xi}{\tau_0}\mathrm{e}^{-t/2\tau_0}\sigma(\xi t/\tau_0) \tag{3.8}$$

$$\sigma(x) = \frac{J_1(2\sqrt{x})}{\sqrt{x}} \tag{3.9}$$

where $J_1(x)$ is the Bessel function of first kind and first order. This amplitude oscillates around zero with time while decaying exponentially. The zero points of this oscillations corresponding to $\xi t/\tau_0 = 3.7,\ 12.3,\ \ldots$ are defined by the roots of the Bessel function. Such a beat is called dynamical beat (DB). The time dependence of the NFS intensity can then be obtained as a square of the amplitude:

$$I(t) = \frac{I_0}{\Delta\omega}\mathrm{e}^{-\mu_e L}\frac{\xi^2}{\tau_0^2}\mathrm{e}^{-t/\tau_0}\sigma^2(\xi t/\tau_0) \tag{3.10}$$

where the decrease of intensity due to the electronic absorption in the sample with the absorptions length μ_e is taken into account. Some characteristic features of the DB are [vB99]: the DB is aperiodic, the apparent periods increase with time; the DB periods decrease with increasing effective thickness; the initial decay is sped up proportionally to the effective thickness.

If the value $\xi t/\tau_0$ is relatively small (small effective thickness of the sample or short experimental time window) then a solution is obtained, which is called quasi-kinematical approximation in this work. The function $\sigma(\xi t/\tau_0)$ can be approximated by an exponent $\sigma(\xi t/\tau_0) \approx \exp(-\xi t/2\tau_0)$ so that the intensity is replaced by [vBSH$^+$92]

$$I(t) = I(0)\mathrm{e}^{-(1+\xi)t/\tau_0} \tag{3.11}$$

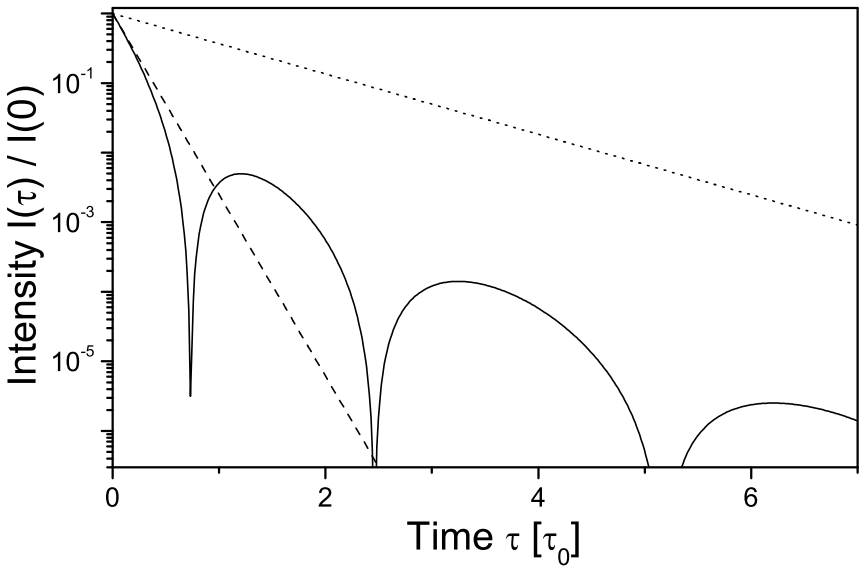

Figure 3.1: Time evolution of the NFS intensity (solid line), its kinematical (dotted line) and quasi-kinematical (dashed line) approximation. The state of the nucleus is assumed to be unsplit and the effective thickness is $\xi = 5$.

This approximation is valid for $\xi t/\tau_0 \lesssim 0.75$. One can estimate the characteristic decay time as

$$\tau_d = \frac{\tau_0}{1+\xi} \tag{3.12}$$

so that with increasing effective thickness the characteristic decay time decreases. This phenomenon, called speed-up effect, is a property of the coherent superposition of multiple scattering processes. The time dependence of the NFS intensity in full form, kinematical and quasi-kinematical approximation are shown in the Fig. 3.1. One easily sees that the full NFS intensity decays faster than the one in the kinematical approximation even at small times. One can conclude that for $\xi \sim 1$ the kinematical approximation is unrealistic and one has to use the quasi-kinematical approximation.

3.3.2 Hyperfine splitting

Time-independent hyperfine interactions lead to an additional factor in $K(t)$. We limit our consideration to the quadrupole interaction defined by an axially symmetric electric field gradient (EFG). This type of the interaction is described in Appendix B. The quadrupole interaction splits the excited state of the ^{57}Fe nucleus into two sub-levels. Also we assume that the EFG is isotropically distributed over the nuclear ensemble. Then the

self-correlation function $K(t)$ can be written as

$$K(t) = \mathrm{e}^{-t/2\tau_0} \cdot \cos(\Omega t/2) \tag{3.13}$$

and the intensity in the kinematical approximation is given by

$$I(t) = \frac{I_0}{\Delta\omega} \frac{\xi^2}{4\tau_0^2} \mathrm{e}^{-t/\tau_0}(1 + \cos(\Omega t))/2. \tag{3.14}$$

The time evolution of the intensity is described by a natural decay modified by a quantum beat (QB) which is periodic in time. The effective thickness is decreased by a factor of two compared with the single resonance case (see eq. (3.7)). Phenomenologically one can explain such a behavior by separating all nuclei into two equal fractions with the resonant energies $E_0+\hbar\Omega/2$ and $E_0-\hbar\Omega/2$, respectively. Two indistinguishable scattering channels appear and scattering of a photon through each of them results in a wavelet of a single energy. The interference of the wavelets leads to a QB.

By contrast to the single resonance case, the general solution for the amplitude (see eq. (3.3)) in presence of hyperfine interactions can not be obtained analytically. Numerical calculations based on the iterative procedure given by eqs. (3.4),(3.5) have to be performed. However, there is an analytical approximation which is valid for small values of $\xi/\Omega\tau_0$. This approximation is important for the experiments presented in this work. The parameter of approximation can be explained as following. The absorption/emission probability of each sub-level is described in the energy domain by a Lorentzian with line width Γ_0. This leads to the overlap of the probabilities of two sub-levels separated by $\hbar\Omega$. The area of the overlap region is proportional to $\Gamma_0/\hbar\Omega = 1/\Omega\tau_0$. This overlap gives the possibility for a photon scattered by one sub-level be re-scattered by another one. This process called cross-scattering becomes stronger with increase of multiple scattering which is proportional to the effective thickness ξ. Combining the two proportionalities we obtain the parameter $\xi/\Omega\tau_0$. In the first order of the parameter the intensity can be approximated as

$$I(t) \simeq \frac{I_0}{\Delta\omega}\mathrm{e}^{-\mu_e L} \cdot \frac{\xi^2}{4\tau_0^2} \cdot \mathrm{e}^{-t/\tau_0}\, \sigma^2(\xi t/2\tau_0) \cdot (1 + \cos(\Omega t + \xi/2\Omega\tau_0))/2 \tag{3.15}$$

The expression for the intensity factorizes into a term describing the single resonance intensity (see eq. (3.10)) with half effective thickness and into a QB term with additional phase shift. This shift of the QB was confirmed in experiments in Laue geometry diffraction [CSZ+92] and in NFS [vBSH+92]. The validity of this approximation is checked in Fig. 3.2. Here the numerical simulation of the intensity according to eqs. (3.3)-(3.5) is presented for various values of $\xi/\Omega\tau_0$. One can see that the minimum positions of the QB are shifted to smaller times with increasing of the thickness. Additionally, the single-resonance intensity with the effective thickness $\xi/2$ is shown. This intensity, according to

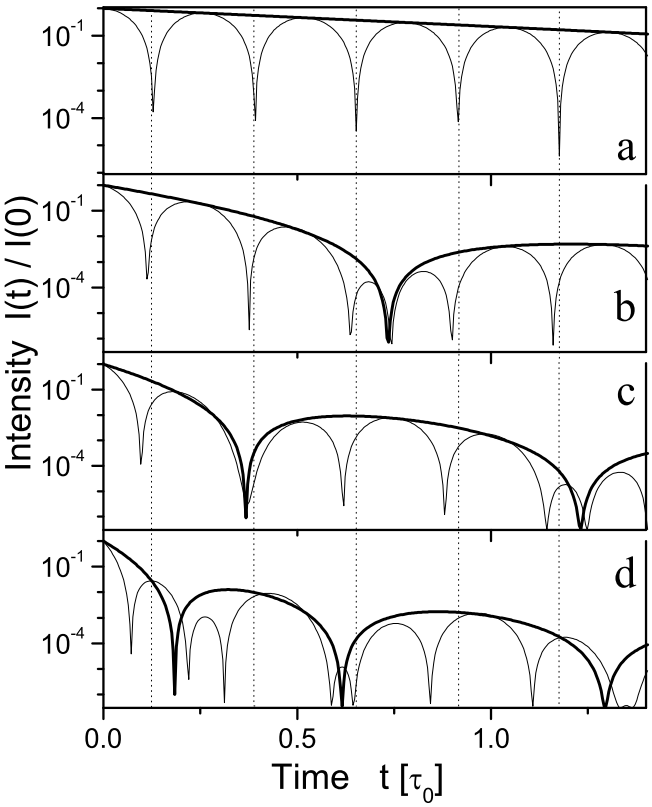

Figure 3.2: Time evolution of the NFS intensity. The solid line represents the numerical simulation of the intensity for the sample with quadrupole splitting and effective thickness ξ. The thick solid line represents the single resonance intensity (see eq. (3.10)) with effective thickness $\xi/2$. The parameter of the quadrupole splitting $\hbar\Omega$ is chosen as $24\Gamma_0$. The effective thickness is $\xi = 0.5$ (a), 5 (b), 10 (c) and 20 (d). The vertical dotted lines show the positions of the QB minima for (a).

eq. (3.15), has to be an envelope of the numerical simulation. It is seen that this is valid for $\xi/\Omega\tau_0 = 0.02, 0.2, 0.4$. However, when $\xi/\Omega\tau_0$ becomes comparable to 1 ($\xi/\Omega\tau_0 = 0.83$ in the figure) the approximation fails. In this case the interaction of QB and DB structures changes strongly the shape of the intensity.

3.4 Influence of spatial dynamics on NFS

Two important features of NFS are exploited in order to obtain information about condensed matter dynamics. NFS is a nuclear spectroscopy technique, like nuclear magnetic resonance (NMR), nuclear quadrupole resonance (NQR) and MS. Being such NFS observes the time evolution of the hyperfine field at the nucleus via the time evolution of

the nuclear spin. The relaxation processes which involve the hyperfine field are reflected in the spin relaxation and, consequently, in the shape of the scattered intensity. On the other hand, the very small width of the resonance makes NFS as well as MS sensitive to the atomic motion in the time scale up to μs - diffusive motion. This sensitivity to the time dependence of the atom's position makes NFS similar to quasi-elastic neutron scattering.

In MS these two dynamical processes are often considered separately. However, it was pointed out in [Dat75], that in the case of liquid dynamics it is important to take into account both spin relaxation and diffusive motion. In this work we will call the diffusive motion spatial relaxation in order to emphasize that the molecular motion in a glass forming liquid does not obey the classical diffusion law.

3.4.1 General formalism

Using the density matrix formalism one can write the self-correlation function $K(t)$ as [Dat75]

$$K(t) = \mathrm{e}^{-t/2\tau_0} \cdot Tr(\rho \hat{A}(0) \mathrm{e}^{i\mathbf{kR}(0)} \hat{A}^{+}(t) \mathrm{e}^{-i\mathbf{kR}(t)}) \tag{3.16}$$

where $\hat{A}(t)$ is an operator which acts only on the nuclear spin state at time t and defines the intensity and the polarization of the emitted or absorbed radiation, $\mathbf{R}(t)$ is the coordinate of the center of mass of the nucleus at time t and ρ is the equilibrium density matrix for the entire system which can be factorized into the density matrix of the nuclear spin states ρ_n and the density matrix of the surroundings ρ_s. The self-correlation function can be influenced by two different relaxation mechanisms: relaxation in the spin space is seen by the operator $\hat{A}(t)$ and spatial relaxation is seen via the position of the nucleus $\mathbf{R}(t)$. If the nuclear spin dynamics is completely independent of the spatial dynamics, the spin and spatial operators commutate in eq. (3.16) and $K(t)$ factorizes into spatial and spin parts

$$\begin{aligned} K(t) &= \mathrm{e}^{-t/2\tau_0} \cdot Tr(\rho_n \hat{A}(0) \hat{A}^{+}(t)) \cdot Tr(\rho_s \mathrm{e}^{i\mathbf{kR}(0)} \mathrm{e}^{-i\mathbf{kR}(t)})) \\ &= \mathrm{e}^{-t/2\tau_0} \cdot G(t) \cdot F_s(\mathbf{k}, t) \end{aligned} \tag{3.17}$$

Here $G(t)$ represent the self-correlation of the nuclear spin in time and can be called perturbation factor in analogy to Time Differential Perturbed Angular Correlation as will be seen in the next chapter. $F_s(\mathbf{k}, t)$ is called van Hove self-intermediate function [vH54] and represents the evolution of the spatial position of the nucleus in time according to the theory of Singwi and Sjölander [SS60].

The absolute value of the spin is given by the nuclear state, its direction is defined by the experienced hyperfine fields. If no field is seen by the nucleus, the spin direction and its time evolution are undefined. In this case the perturbation factor $G(t)$ equals 1. When

a time-independent hyperfine field acts on the nucleus, the spin precesses around the field direction, resulting in a periodic oscillation of the perturbation factor. For quadrupole interaction, which is considered in this work, $G(t) = \cos(\Omega t/2)$. This information was already used in the Section 3.3.2. Relaxation of hyperfine fields results in spin relaxation, which is expressed by the perturbation factor. Theoretical investigation of spin relaxation applied to Mössbauer spectroscopy have been performed e.g. in [AK64, Blu68, Dat81]. A recent study of spin relaxation in NFS can be found in [LW99].

The factorization in eq. (3.17) is only allowed if spin and spatial time evolution are independent. Otherwise the general expression (3.16) for $K(t)$ has to be considered. An example of the coupling between spin and spatial relaxation will be considered in the following. In molecules the direction of the electric field gradient on the nucleus is defined by the specific molecular structure. Therefore, any rotational molecular relaxation strongly couples with the spin. If the process which governs rotational motion also leads to the change of the nuclear position $R(t)$ then this process is seen by both spin and spatial operators in $K(t)$ and the general expression has to be applied. The theoretical study of this process will be given in the Chapter 4.

3.4.2 Debye relaxation

In this section we neglect the spin part of the self-correlation function $K(t)$, assuming the absence of hyperfine interactions. Then the self-intermediate function $F_s(\mathbf{k}, t)$ defines the time-evolution of the scattered intensity. It can be factorized into parts corresponding to fast and slow nuclear motion relative to the experimental time window. The region of the observation time is limited from the short-time side by $1 \div 10$ ns for technical reasons and from the long-time side by a few μs due to the natural decay. Fast motions that happen on short (picosecond) time scales cannot be detected directly. Instead they give rise to the Lamb-Mössbauer factor f_{LM} with

$$F_s(\mathbf{k}, t) = f_{LM} \tilde{F}_s(\mathbf{k}, t) \tag{3.18}$$

where $\tilde{F}_s(\mathbf{k}, t)$ describes the slow motion of the nuclei that can be observed directly in the experimental time window. A similar factorization is used in neutron scattering where fast motions are described by the Debye-Waller factor f_Q and the momentum transfer Q is used instead of the full momentum of the scattered photon.

The absolute value of the wave vector $\mathbf{k}$ in eq. (3.18) is fixed by the energy of the excited state ($k \approx 7.3$ Å^{-1} for ^{57}Fe). Therefore we omit the dependence of the self-intermediate function on $\mathbf{k}$ and replace $\tilde{F}_s(\mathbf{k}, t)$ by $\tilde{F}_s(t)$.

The factorization in eq. (3.18) goes through the recursion relation (3.5) and results in replacing of the effective thickness ξ by ξf_{LM}. Qualitatively one can say that only a

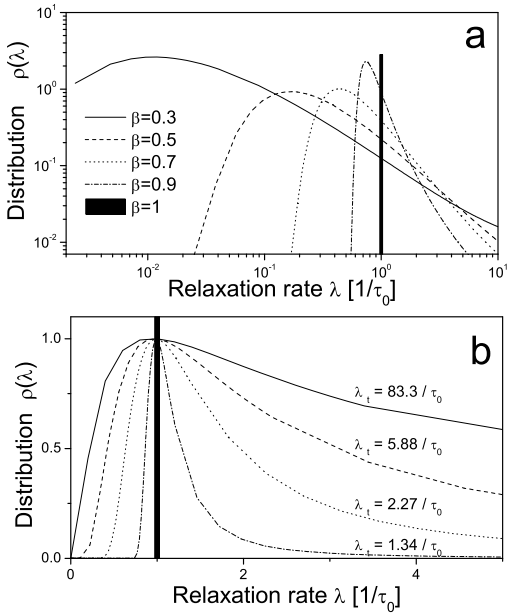

Figure 3.3: a)Distribution of Debye relaxators corresponding to a Kohlrausch relaxation function for $\lambda_t = 1/\tau_0$ and several β; b) distribution of Debye relaxators corresponding to a Kohlrausch relaxation function scaled by λ_t and area to the same position of the maximum point for different β.

fraction f_{LM} of all nuclei in the sample takes part in the scattering process.

The influence of slow motion to NFS has been theoretically investigated by Smirnov and Kohn [SK95, KS98, KS99] for several types of $\tilde{F}_s(t)$: free diffusion governed by Debye (exponential) relaxation, diffusion restricted in space, and diffusion governed by a set of Debye relaxators.

The most simple type of the intermediate function is Debye relaxation $\tilde{F}_s(t) = \exp(-\lambda_t t)$ with a characteristic relaxation rate $\lambda_t = Dk^2$ where D is the diffusion coefficient. In this case the time evolution of the intensity reduces to the analytical expression [KS99]

$$I(t) = I(0)\mathrm{e}^{-t/\tau_0} \cdot \mathrm{e}^{-2\lambda_t t}\sigma^2(\xi f_{LM} t/\tau_0) \tag{3.19}$$

where $I(0)$, the intensity at zero time, is the same as in the static case (see eq. (3.10)) multiplied by f_{LM}^2. One can see that for Debye relaxation the intensity factorizes into the relaxation and multiple scattering. The DB, which is a pronounced feature of the NFS intensity, is not influenced by relaxation. When the effective thickness or the Lamb-Mössbauer

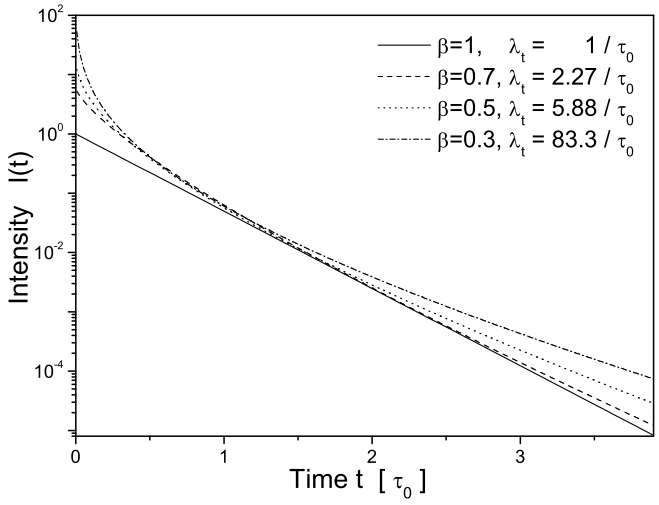

Figure 3.4: Simulation of the NFS intensity in the kinematical approximation. The relaxation is governed by the Kohlrausch relaxation function. The parameters of this function were chosen to have the same position of the main peak of the distribution of Debye relaxators for different β, similar to Fig. 3.3b.

factor of the sample is small, the expression (3.19) reduces to the quasi-kinematical approximation

$$I(t) = I(0)\,\mathrm{e}^{-(1+2\lambda_t\tau_0+\xi f_{LM})t/\tau_0} \tag{3.20}$$

The intensity decays faster than the natural decay. The additional decay is formed by the superposition of multiple scattering and relaxation. It is not possible to separate the terms associated with these two processes in the frame of quasi-kinematical approximation.

3.4.3 Kohlrausch relaxation

The description of the liquid-to-glass transition requires another type of $\tilde{F}_s(t)$, a Kohlrausch relaxation function (see eq. (2.6))

$$\tilde{F}_s(t) = \mathrm{e}^{-(t\lambda_t)^\beta} \tag{3.21}$$

which describes the final decay of the relaxation function in amorphous materials. The stretching parameter β varies in the region $0 < \beta \leqslant 1$. For this type of relaxation we have developed an special approach [SFA+02] which is presented below.

The NFS intensity in the kinematical approximation can be written as

$$I(t) = I(0)\mathrm{e}^{-t/\tau_0}\tilde{F}_s^2(t) = I(0)\mathrm{e}^{-t/\tau_0}\cdot\mathrm{e}^{-2(\lambda_t t)^\beta} \tag{3.22}$$

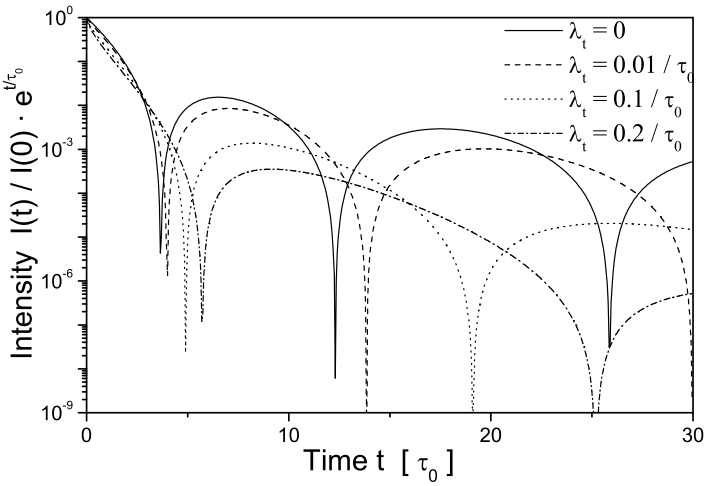

Figure 3.5: Simulation of the NFS intensity normalized to the natural decay. The relaxation is governed by Kohlrausch function with $\beta = 0.5$. The effective thickness parameter was chosen as $\xi f_{LM}/\tau_0 = 1$.

The Kohlrausch relaxation function can be written as a distribution of Debye relaxation processes [GS92]

$$\tilde{F}_s(t) = \int_0^\infty \mathrm{d}\lambda \; \mathrm{e}^{-\lambda t}\rho(\lambda) \tag{3.23}$$

where the distribution $\rho(\lambda)$ corresponds to the probability to find a process with the relaxation rate λ. The distribution $\rho(\lambda)$ is shown in Fig. 3.3a for different values of β and $\lambda_t = 1/\tau_0$. The Debye law ($\beta = 1$) corresponds to the point distribution

$$\rho(\lambda) = \delta(\lambda - \lambda_t). \tag{3.24}$$

For $\beta < 1$, the shape of the distribution is a non-symmetrical peak with a long high-frequency tail defined by the von Schweidler law $\rho(\lambda) \propto (\lambda/\lambda_t)^{-1-\beta}$ and a cut-off at the low frequency. The position of this peak shifts to lower frequencies when β decreases. To compare the influence of β, the distribution, scaled to have the same amplitude and position of the maximum for different β, is shown in the Fig. 3.3b. One can see that the high-frequency tail increases strongly with decreasing β and there is a slight increase of the low-frequency tail. Such behavior of the distribution function defines the shape of the intensity in the kinematical approximation (Fig. 3.4). The Debye relaxators with different frequencies play a role in different time regions. Close to time zero, the shape of the intensity is defined by the high-frequency part of the distribution, whereas the low-frequency part corresponds to large times. In Fig. 3.4 the values of λ_t were chosen as in Fig. 3.3b with position of the distribution maximum at $\lambda = 1/\tau_0$. This fact results in

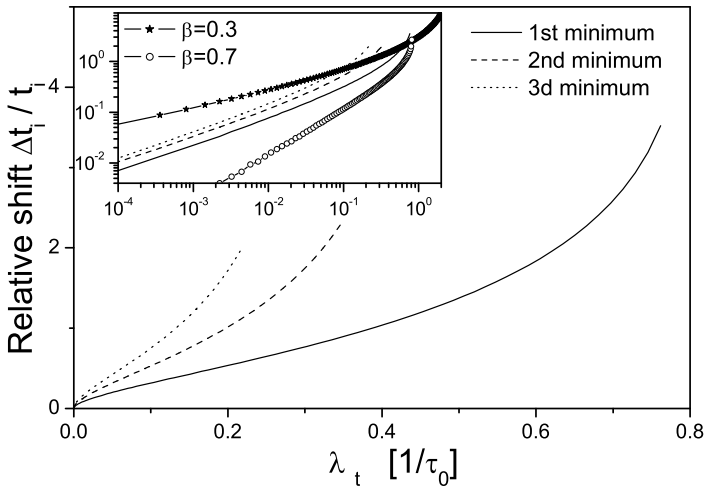

Figure 3.6: Relative shift of the DB structure minima as a function of λ_t for $\beta = 0.5$. In the inset the same curves are shown in a log-log plot. Additionally, the relative shift for the first DB structure minimum is shown for $\beta = 0.3$ and 0.7.

roughly the same slope of the intensity at the region of time around $t = \tau_0$ for different β. Before this time, the high frequency tail dominates the intensity and there is a strong decay for small values of β compared to $\beta = 1$. After $t = \tau_0$, only a weak change of the exponential slope is observed due to roughly the same position of the cut-off of the distribution in the low-frequency region. Qualitatively, the same result was obtained in [KS98] for the case of a discrete distribution of Debye relaxators which describe jump diffusion in a crystal.

The influence of Kohlrausch relaxation on the time evolution of the intensity in the general case is more complicated. It is different from the influence of the Debye relaxation where the multiple scattering factor enters multiplicatively. The numerical simulation of the intensity as a function of time is shown in Fig. 3.5 for $\beta = 0.5$ and different λ_t. As opposed to the simple exponential relaxation, the relaxation governed by the distribution of the exponential relaxators leads to a shift of the DB structure to later times. It is clearly seen from Fig. 3.5 for the Kohlrausch relaxation function. Also it has been shown in [SK95, KS98] for the diffusion described by a discrete set of the exponential relaxators.

The analysis of the influence of the relaxation governed by the Kohlrausch function to the multiple scattering factor of the delayed intensity can be done in the approximation of small values of the relaxation rate λ_t, when the Kohlrausch relaxation function reduces to the von Schweidler function. It is shown in Appendix A that the time evolution of the

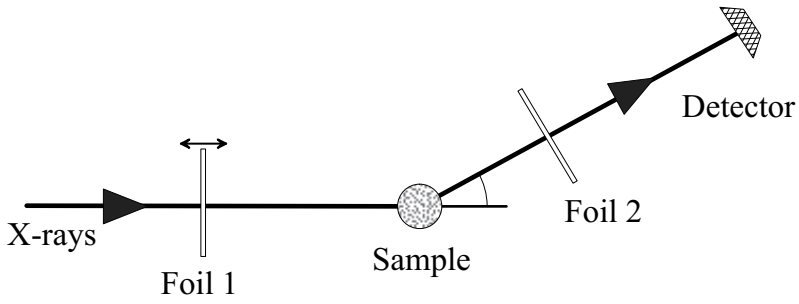

Figure 3.7: Experimental setup of TDI. Two single line resonant foils are placed before and after the sample with the first mounted on a Mössbauer drive in constant velocity mode. Detector measures the radiation scattered in angle ϑ and corresponded momentum transfer Q.

delayed intensity can be written as

$$I(t) = I(0)\mathrm{e}^{-t/\tau_0} \cdot \left(\sigma(\xi f_{LM} t/\tau_0) - (\lambda_t t)^\beta \sigma_\beta(\xi f_{LM} t/\tau_0)\right)^2 \tag{3.25}$$

where $\sigma_x(z)$ is a generalized version of the function $\sigma(z) \equiv \sigma_1(z)$. It is introduced in eq. (A.20). This expression gives the possibility to obtain the shift of the positions of the DB minima as a function of the relaxation rate. If t_i is the time corresponding to the ith minimum of the delayed intensity for the static case and Δt_i is a shift of this minimum from its static position due to the relaxation then

$$\frac{\Delta t_i}{t_i} = (\lambda_t t_i)^\beta C_i(\beta) \tag{3.26}$$

$$C_i(\beta) = \frac{\sigma_\beta(\xi f_{LM} t_i/\tau_0)}{\xi f_{LM} t_i/\tau_0 \cdot \sigma'(\xi f_{LM} t_i/\tau_0)} \tag{3.27}$$

The relative shift of the minimum position is proportional to λ_t^β with a proportionality coefficient that depends only on β. For the extremal case of $\beta = 1$ (Debye relaxation), the coefficient $C_i(1) = 0$ which corresponds to zero shift. The numerical simulation of the relative shift of the DB structure minima positions for the relaxation governed by Kohlrausch function is shown in Fig. 3.6. The inset of this figure shows the log-log plot of the region near $\lambda_t = 0$. It shows that at the region of small λ_t, the relative shifts obey eq. (3.26). When λ_t becomes comparable with $\xi f_{LM}/\tau_0$, the relative shifts begin to diverge to large times. The root-like dependence of the relative shift for small λ_t means that an infinitely small value of the relaxation rate results in a certain (not infinitely small) value of the relative shift. It gives the possibility to extract information about relaxation from multiple scattering corrections of the NFS intensity in the temperature region where the relaxation is very small.

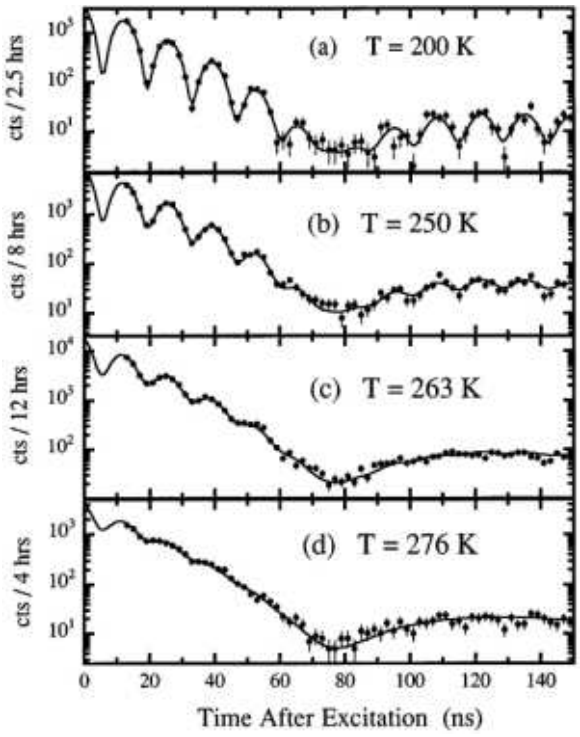

Figure 3.8: Scattering from glycerol measured in the structure factor maximum $Q = 1.5\ \mathring{A}^{-1}$ at different temperatures [BFM+97].

3.5 Time domain interferometry

At this place we would like to mention briefly that nuclear forward scattering can even be used to determine spatial relaxation in non-resonant samples, using Time Domain Interferometry (TDI). This interferometric method is the time analog of Rayleigh Scattering of Mössbauer Radiation (RSMR); for a review on RSMR see e.g. [Cha79, KGNP90]. The method was developed by Baron et al. [BFM+97] and theoretically described by Smirnov et al. [SKP01]. Fig. 3.7 shows the experimental setup of TDI. A synchrotron pulse excites a resonant foil 1, then is scattered by the sample with the momentum transfer Q, depending on angle ϑ, and excites the resonant foil 2. The resonant energies of the two single-resonance foils are shifted relative to each other by $\hbar\Omega$ using a Mössbauer drive operated in constant velocity mode. After excitation by a synchrotron pulse, nuclear scattering will show a temporal interference pattern equivalent to a QB. The sample placed between the foils stochastically perturbs the phase shift between the wavelets scattered by the two foils. This leads to a damping of the QB, which is described by the self-intermediate correlation function $S(Q,t)$ of the sample. For two identical foils and $\hbar\Omega$ larger than the resonant line width the scattering intensity can be written as [FPB99]

$$I(Q,t) \propto |R(t)|^2 \left(S(Q) + S(Q,t)\cos\Omega t\right) \tag{3.28}$$

where $S(Q)$ is the static structure factor of the sample and $|R(t)|^2$ is the intensity scattered by one resonant foil.

The results of TDI measurements on the glass forming liquid glycerol are shown in Fig. 3.8. The envelope of the QB structure is the self-intermediate function, which exhibits a stretched exponential decay. As temperature increases the characteristic relaxation rate increases and the QB becomes more strongly damped.

This technique can be used to study quasi-elastic scattering on time scales of ∼5 ns to ∼500 ns (energy scales of ∼150 neV to ∼1.5 neV) with large momentum transfer (up to 14 Å^{-1}). The inherent brilliance of SR permits one to do experiments with small (∼1 mm) samples and with extreme (μrad) collimation, which is not possible for RSMR.

Chapter 4

SR-based perturbed angular correlation (SRPAC)

This chapter is dedicated to the description of a new method in the family of NRS methods - SR-based Perturbed Angular Correlation (SRPAC). This method is based on incoherent NRS, which is described in the first section. The principles and theoretical description of SRPAC are discussed in the two following sections. The theory to describe the influence of rotational relaxation on SRPAC is developed in the next chapter. The last part explains how the same theoretical approach can be applied to explain the influence of rotational relaxation on NFS.

4.1 Spatially coherent versus incoherent nuclear resonant scattering

Incoherent NRS was studied extensively during the last 10 years in connection with the possibility to investigate lattice vibrations. Pioneering work on this method, now called nuclear inelastic scattering (NIS) were done by Seto et al. [SYK+95], Sturhahn et al. [STA+95] and Chumakov et al. [CRG+95]. This method uses incoherently scattered intensity integrated in time.

The time evolution of incoherent NRS of SR has been investigated less thoroughly. Theoretically the incoherent channel of NRS was studied by Trammell and Hannon [TH78], Iolin [Iol96] and Sturhahn and Kohn [SK99]. The first experimental observations of the time evolution of incoherent scattering were done by Bergmann et al. [BHS94] and by Baron et al. [BCR+96].

There are several possible channels of incoherent nuclear resonant scattering: nuclear resonant fluorescence, conversion electron emission and atomic fluorescence following nuclear absorption [SK99]. They are shown in Fig. 4.1. The difference between these chan-

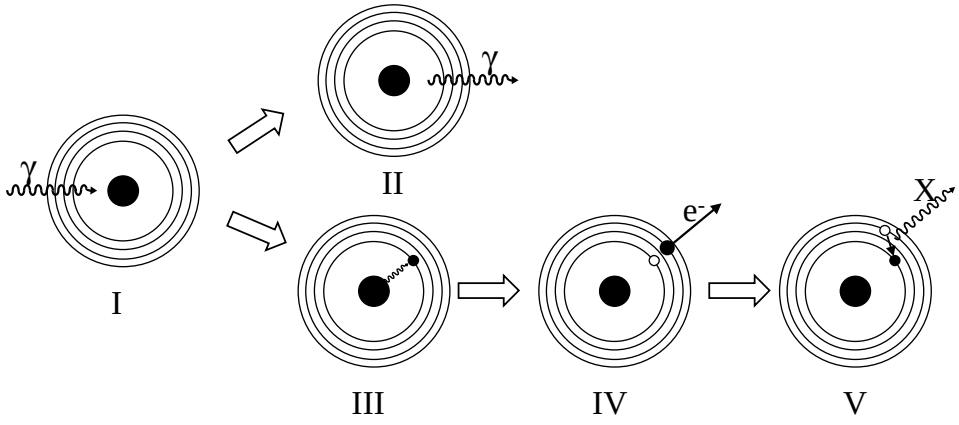

Figure 4.1: Incoherent NRS. Steps: I - resonant absorption of the γ-photon with $E_\gamma \simeq 14.4$ keV for ^{57}Fe, II - reemission of the γ-photon with $E_\gamma \simeq 14.4$ keV (nuclear resonance fluorescence), III - transfer of the excitation energy to the electron shell, IV - emission of the electron and formation of a hole, V - filling of the hole by another electron and emission of an X-ray photon.

nels is in the type of radiation following the de-excitation of the nucleus.

Nuclear resonant fluorescence corresponds to the reemission of the photon by the nucleus (II in the figure). Another channel of de-excitation, the internal conversion, is the transfer of the excitation energy to the electron shell (III). After a conversion electron has been emitted (IV), the remaining ion core will de-excite by emission of X-rays (V). The conversion coefficient α gives the ratio of internal conversion to resonance fluorescence. For ^{57}Fe $\alpha = 8.2$, and the conversion channel of the scattering is much stronger than nuclear resonant fluorescence. However, due to the complexity of the process of atomic fluorescence, X-rays lose information about the nuclear process. The conversion electrons undergo several collisions with large deflection angles before emanating from the surface and have to be averaged over all directions of emission which leads also to a loss of information about the nuclear scattering [SQTA96]. Therefore, in this study we concentrate on the nuclear resonant fluorescence and do not consider conversion channels at all. In the following the term incoherent scattering of SR will mean only nuclear resonant fluorescence.

Incoherent NRS is characterized by the possibility to identify the nucleus which scatters the photon. The necessary condition for it is that the nucleus must change its state in the scattering process and is therefore tagged. This can happen by a change of spin of the ground state (spin-flip process) or by a change of the vibrational state of the nucleus. *Coherent* scattering, by contrast, is de-localized over the whole ensemble of nuclei [TH78, KAK79]. There is no change of state of any nucleus due to scattering. An exception could be coherent inelastic scattering which has not been observed up to now

due to the short lifetime of phonons compared with the nuclear lifetime [CBR+98].

NFS is elastic scattering and is proportional to the square of the Lamb-Mössbauer factor ${f_{LM}}^2$. Incoherent scattering can happen with absorption/emission of phonons. This fact gives the possibility to measure the phonon density of states [CRG+95, STA+95] by tuning the energy of the incoming beam with respect to the nuclear resonance energy. If the energy width of the incoming beam is large enough to cover all phonon assisted processes, then incoherent scattering does not depend on f_{LM} at all.

The delocalization of coherent scattering results in a strong collimation of the scattered beam. If the target is formed by an irregular ensemble of nuclei, then scattering exists only in the forward direction. Incoherent scattering, localized on a certain nucleus, can happen in any direction. The probability of scattering under a certain angle is defined by the spins of the ground and excited states of the nucleus and the direction, the multipolarity and the polarization of the incoming photon.

Incoherent scattering is single nucleus scattering. If no hyperfine interactions exist then the time evolution of the intensity is an exponential decay with a characteristic lifetime τ_0, i.e. a natural decay. The cross-section of the resonant absorption of the photon by a single nucleus is relatively small, and one can usually neglect multiple scattering.

Another situation appears in coherent scattering. The cross-section of the absorption of a photon by the collective ensemble of nuclei is relatively high, which results in an essential contribution of multiple scattering. It changes the time evolution of scattering which exhibits a speed-up effect and dynamical beats (see preceding chapter on NFS).

When hyperfine interactions split ground and excited states of the nucleus, experimentally indistinguishable paths of scattering appear which interfere. Therefore the evolution of the scattered intensity is modulated by QB. The interference pattern is different for the coherent and incoherent channels. Incoherent scattering is sensitive only to the splitting of the excited state. Coherent scattering, on the other hand, is sensitive to both ground and excited state splitting. The QB in this case occurs between frequencies corresponding to all allowed transitions between ground and excited states. The quadrupole interaction on ^{57}Fe splits only the excited state into two sub-levels. Therefore, in both coherent and incoherent scattering channels a single frequency QB occurs only. However, magnetic interaction which splits both excited and ground states leads to different QB structures for the coherent and incoherent scattering [BCR+96].

It was shown in the previous chapter how spatial relaxation influences NFS. Incoherent scattering, in contrast, is independent of the motion of the nuclei. One can explain this as follows. The general property of the coherent scattering implies the same energy of the photon before and after the excitation. The translational diffusion gives rise to a shift of the nuclear energy during the scattering process. This shift is seen as an additional decay of the coherent scattering. The incoherent scattering is not sensitive to the energy of the

Table 4.1: Comparison of NFS and incoherent NRS.

	NFS	Incoherent NRS
Elastic/inelastic scattering	Elastic or quasi-elastic scattering, $\propto {f_{LM}}^2$	Inelastic scattering in most cases, no dependence on f_{LM}
Direction of scattering	Well collimated in forward direction	Scattering in 4π
Influence of dynamics	Spatial dynamics + spin dynamics (if hyperfine splitting exists)	Only spin dynamics (if hyperfine splitting exists)
Shape of the intensity	Combination of natural decay, QB and DB	Natural decay modulated by QB

photon and therefore is not sensitive to the translational diffusion.

4.2 Principle of SRPAC

Incoherent NRS can be applied to study hyperfine interactions. In this sense it belongs to the family of nuclear spectroscopy techniques, such as Nuclear Magnetic Resonance (NMR), Mössbauer Spectroscopy, NFS and Time Differential Perturbed Angular Correlation of γ-rays (TDPAC). Incoherent NRS can be considered as a scattering variant of the last method and can be called SR-based Perturbed Angular Correlation (SRPAC).

The probability of emission (absorption) of electromagnetic radiation depends, in general, on the angle between the expectation value of the angular momentum vector of the radiating system and the direction in which the radiation is observed. For an ordinary source of radiation, consisting of an ensemble of many radiating nuclei with their spins oriented at random, the emission of radiation is isotropic in space. In order to observe an anisotropic radiation pattern, the distribution of spins in the ensemble must favor a definite direction or directions, i.e. the ensemble of nuclear spins has to be oriented in space. Such an ensemble may be prepared by different methods [SA75]:

1. Orientation by observing a preceding emitted radiation in a well defined direction. This situation is realized in TDPAC.

2. Orientation by absorption of electromagnetic radiation of well defined direction and well defined polarization. This situation is realized in SRPAC.

At the second step, a nucleus thus oriented emits radiation anisotropically. Therefore there is an angular correlation between those photons absorbed/emitted at the first step

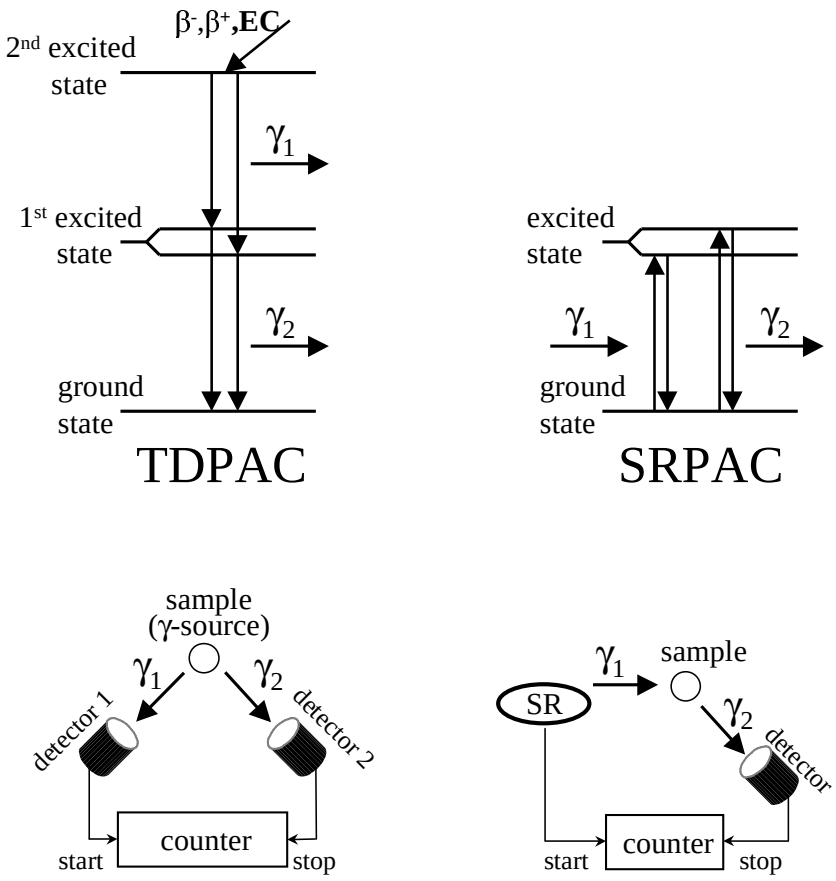

Figure 4.2: The schematic drawing of the principle and experimental setup of TDPAC (left side) and SRPAC (right side).

and those emitted at the second step. A schematic drawing for SRPAC and TDPAC is shown in Fig. 4.2.

In TDPAC (left side of Fig. 4.2) a nucleus converts to the so-called second excited state by β-decay or by an electron capture process from the mother isotope with a standard lifetime ranging from a few hours to several days. During de-excitation of the second excited state the photon γ_1 is observed by the first detector, and the nucleus goes to the first excited state. The scattering of γ_2 emitted during de-excitation of the first excited state depends on the angle between γ_1 and γ_2. Interferences between sub-levels of the excited state lead to time precession of the angular probability for emission of γ_2. The number of the γ-quanta observed by the second detector as a function of the coincidence time, e.g. the time between γ_1 and γ_2, gives the TDPAC intensity as a function of time and angle between the detectors. More information about TDPAC can be found in reviews [But96, Mah89].

In SRPAC (right side of Fig. 4.2) a nucleus gets excited via absorption of a SR photon. Directional selection and timing by the first detector in TDPAC are replaced in SRPAC by direction, polarization and timing of the incident SR flash.

The angular distribution of radiation depends on the orientation of the nuclear spin at the time the radiation is emitted. In many experimental situations the time elapsed between the formation of the oriented state and the time of emission of radiation is long enough to cause an appreciable change of the orientation of the ensemble of nuclear spins by hyperfine interactions. It leads to a time structure of the angular correlations, the shape of which depends on the type of perturbations:

1. Static interactions are caused by the coupling of the nuclear spins with static hyperfine fields, i.e., fields which are constant in magnitude and direction during the lifetime of the excited nuclear state. A constant field causes a precession of the nuclear spins that result in a periodic behavior of the radiation pattern. It is important that static interactions will not destroy the orientation of an ensemble, no matter how long the ensemble is in the excited state and no matter how strong the fields are.

2. Time-dependent (relaxation) interactions are caused by fluctuating fields, such as the fields experienced by nuclei in a liquid environment. It may result in a complete loss of orientation with time.

4.3 Theory of SRPAC in the static case

The theoretical formulation of the angular distribution and correlation of γ-rays has been developed by Frauenfelder, Steffen and Alder [FS65, SF64, SA75]. We apply their results to derive the expression for the SRPAC intensity.

A schematic drawing of the experiment is shown in Fig. 4.3. The incoming beam with wave vector $\mathbf{k}_{in}$ is polarized in the horizontal plane which is the plane of the SR storage ring with polarization vector σ. The scattered beam observed by the detector has the wave vector $\mathbf{k}_{out}$ and the detector covers the spherical angle $\Delta\Omega$. The SRPAC intensity, i.e. the intensity observed by the detector, is given as

$$I(t) = I_0 \cdot \mathrm{e}^{-t/\tau_0} \int_{\Delta\Omega} d\Omega \frac{dW(\mathbf{k}_{in}\sigma, \mathbf{k}_{out}, t)}{d\Omega} \tag{4.1}$$

where τ_0 is the lifetime of the excited state, I_0 is the intensity of the nuclear fluorescence in the entire solid angle at zero time and $dW(\mathbf{k}_{in}\sigma, \mathbf{k}_{out}, t)/d\Omega$ is the differential angular probability of scattering. The calculation of this function is done in Appendix C. The differential angular probability of scattering depends, in general, on the multipolarity of

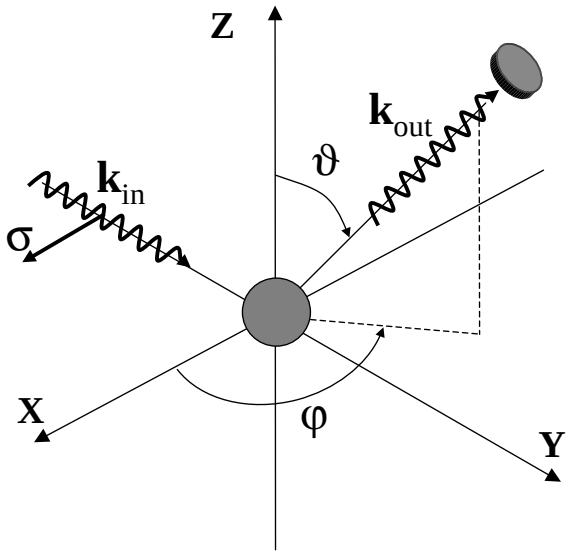

Figure 4.3: A schematic drawing of the SRPAC experiment. The incoming synchrotron radiation has the wave vector $\mathbf{k_{in}}$ and polarization vector σ in the plane of the storage ring (horizontal plane). The scattered radiation with wave vector $\mathbf{k_{out}}$ is observed by the detector without polarization analysis. The polar and azimutal angles ϑ and ϕ define the direction of scattering in the coordinate system connected with the vertical axis.

the photon, the values of the spins for the excited (I_e) and ground (I_g) states of the nucleus and the direction of the hyperfine field. We limit our consideration here to the case of ^{57}Fe as a resonant nucleus. Therefore the multipolarity of the photon is $M1$ and the spins of the excited and ground states are $I_e = 3/2$ and $I_g = 1/2$. The hyperfine fields are assumed to be isotropically distributed over the nuclear ensemble. It is convenient to choose a coordinate system where the z-axis is connected with the vertical direction, i.e. the direction perpendicular to the plane formed by wave vector and polarization of incoming photon (see Fig. 4.3). Then the angular probability is given as (see eq. (C.13))

$$\frac{dW(\vartheta;t)}{d\vartheta d\phi} = \frac{1}{4\pi} \cdot \left(1 - \frac{1}{2} P_2(\cos\vartheta) G_{22}(t)\right) \tag{4.2}$$

where ϑ and ϕ are the polar and azimuthal angles of scattering in the coordinate system connected with the vertical axis, $P_2(x)$ is a Legendre polynomial of the second order, and $G_{22}(t)$ is called the perturbation factor of second order. $G_{22}(t)$ does not depend on the geometry of the experiment and contains all the information about the dynamics of the process. It strongly depends on the type of the hyperfine interaction. If no interaction exists then $G_{22}(t) = 1$.

Inserting eq. (4.2) to eq. (4.1) one obtains the expression for the SRPAC intensity

$$I(t) = I_0 \frac{\Delta\Omega}{4\pi} \cdot \mathrm{e}^{-t/\tau_0} \left(1 - A_{22} G_{22}(t)\right) \tag{4.3}$$

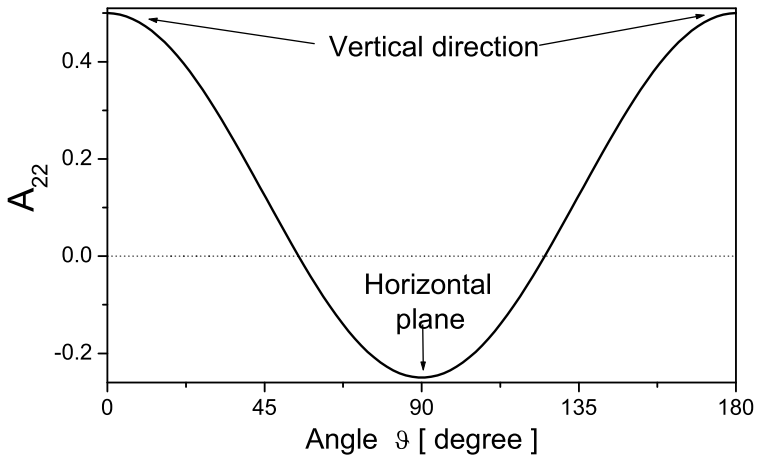

Figure 4.4: The anisotropy coefficient A_{22} as a function of the polar angle ϑ.

where

$$A_{22} = \frac{1}{2} \int_{\Delta\Omega} \frac{\mathrm{d}\Omega}{\Delta\Omega} \cdot P_2(\cos\vartheta) \tag{4.4}$$

is called the anisotropy coefficient of second order. In this expression the dynamical and geometrical features of SRPAC are separated into $G_{22}(t)$ and A_{22}. The intensity consists of two parts: an isotropic part which exponentially decays in time and an anisotropic part the decay of which is modulated by the perturbation factor. The anisotropy coefficient A_{22} is the relative weight of the anisotropic part at zero time.

The anisotropy coefficient A_{22} depends on the polar angle ϑ. The dependence is shown in Fig. 4.4 for the case of a point size detector. In the vertical direction, A_{22} has a maximum value and decreases with increasing angle. For $\vartheta \approx 54.7^o$ the anisotropy coefficient becomes zero, which means that independent on the shape of the perturbation coefficient, the SRPAC intensity follows a natural decay in time. In the horizontal plane ($\vartheta = 90^o$) A_{22} is negative, and its absolute value is equal half the value in the vertical direction. The time evolution of the anisotropy $A_{22}G_{22}(t)$ observed in the horizontal plane is an inverse image of that observed in the vertical direction scaled by a factor of two, independent of the type of interaction.

In the case of static interactions, the perturbation factor $G_{22}(t)$ can be written as [But96]:

$$G_{22}(t) = \frac{1}{5} + \sum_{m \neq m'} \begin{pmatrix} 3/2 & 3/2 & 2 \\ m' & -m & N \end{pmatrix}^2 \cos\frac{(E_m - E_{m'})t}{\hbar} \tag{4.5}$$

where E_m denotes the energy of the m-th sublevel of the excited state and the brackets is the standard notation for the Wigner 3j-symbol. The time evolution of the perturbation factor in the static case is described by periodic oscillations and an additional constant term called hardcore.

We limit our consideration to the quadrupole hyperfine interactions (see Appendix B). In this case the expression for the perturbation factor simplifies to

$$G_{22}(t) = \frac{1}{5} + \frac{4}{5}\cos\Omega t \tag{4.6}$$

where Ω denotes the quadrupole splitting. Using this expression for the perturbation factor and assuming a point size of the detector in eq. (4.4), the SRPAC intensity can be written as

$$I(t) \propto \mathrm{e}^{-t/\tau_0}\,(1 + K\cos\Omega t) \tag{4.7}$$

where

$$K = \frac{4A_{22}}{A_{22} - 5} = \frac{12\cos 2\vartheta + 4}{3\cos 2\vartheta - 39} \tag{4.8}$$

Here we introduce the experimentally observed value K - contrast of the quantum beats.

One can see that the time evolution of the SRPAC intensity shows a natural decay modulated by a single frequency QB. It is similar to the time evolution of the NFS intensity in the kinematical approximation (see eq. 3.14). However, whereas the contrast of the QB is equal to 1 for NFS, in SRPAC the contrast is less than 1 and changes with angle. The simulation of the SRPAC intensity for various polar angles ϑ is shown in Fig. 4.5. The contrast K is about -0.44 for the vertical direction and about 0.19 for the horizontal plane. Additionally the NFS intensity is shown in this figure. One can see that the QB in NFS is in anti-phase to that for SRPAC in the vertical direction and in phase in the horizontal plane.

One can compare the result for the SRPAC intensity on ^{57}Fe with the TDPAC angular correlation intensity on the same isotope. The mother isotope is ^{57}Co and two photons with multipolarity $M1$ are emitted during the following cascade of spins: $5/2 \to 3/2 \to 1/2$. Then the angular probability is given as (see eq. C.14)

$$\frac{dW(\vartheta'; t)}{d\vartheta'} \propto \left(1 + \frac{1}{20}P_2(\cos\vartheta')G_{22}(t)\right) \tag{4.9}$$

where ϑ' is the scattering angle defined by $\mathbf{k}_{in}$ and $\mathbf{k}_{out}$ and $G_{22}(t)$ has the same shape as for SRPAC. Comparing this expression with the one for SRPAC (see eq. (4.2)), one can notice that the anisotropy coefficient for TDPAC is 10 times less than for SRPAC. Also the symmetry axis for the scattered radiation changes from the z-axis for SRPAC to the y-axis for TDPAC. The maximal value of contrast K for TDPAC is obtained in the forward direction and equals ~ 0.04. Such a rather small contrast limits the TDPAC experiment with ^{57}Fe. Only test measurements have been performed [HRBL69].

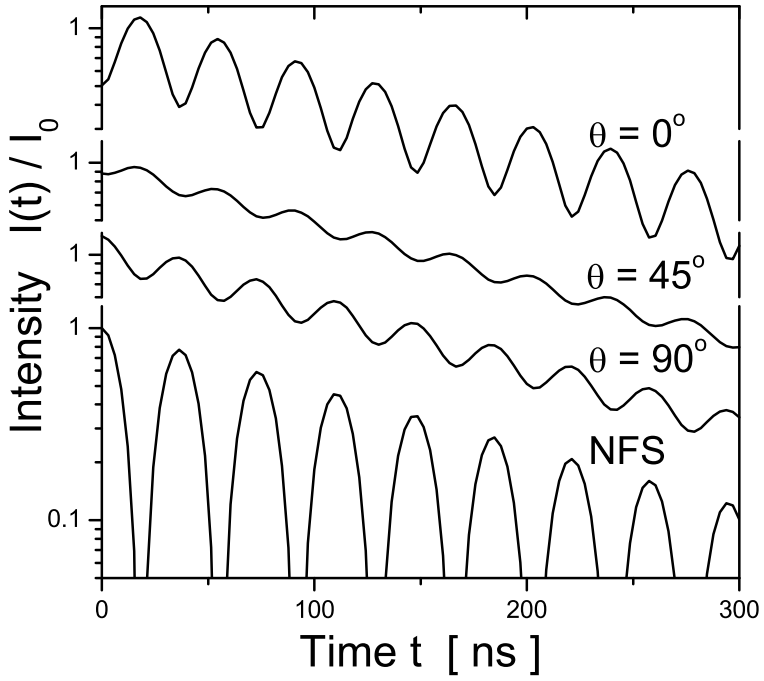

Figure 4.5: Simulation of the SRPAC intensity for various polar angles ϑ. In the bottom the kinematical approximation of the NFS intensity is shown. The quadrupole splitting was taken as $\hbar\Omega = 24\Gamma_0$.

4.4 Influence of spin dynamics on SRPAC

Here we consider the influence of time-dependent hyperfine interactions on SRPAC. This general task will be reduced to the following. We consider a molecule in which a quadrupole interaction between nucleus and the surrounding exists and the direction of the EFG, i.e. the spin quantization axis, is defined by the specific molecular structure. The molecular rotation leads here to a rotation of the EFG. The time evolution of the perturbation factor is driven by two processes: precession around the EFG with the characteristic frequency Ω and stochastic rotation of the EFG direction with a characteristic jump rate λ. The ratio of Ω and λ defines the characteristic shape of $G_{22}(t)$. If the relaxation is slow, i.e. $\lambda \ll \Omega$, the time evolution of $G_{22}(t)$ is mainly described by precession around the EFG which leads to oscillations in time. The slow averaging due to the stochastic rotation damps the oscillations. In the opposite case, when $\lambda \gg \Omega$, the change of the EFG direction is so fast that no precession appears. The ensemble of spins relaxes to the isotropic state exponentially.

In general, the calculation of the perturbation factor in the presence of relaxation is a quite complicated task. There are several ways to solve it using different approaches.

One can mention works of Sillescu [SK68, Sil71] as applied to NMR, Afanas'ev and Kagan [AK64] as applied to MS, Blume and Dattagupta [Blu68, Dat81, Dat87] as applied to MS and TDPAC, Winkler [WG73, Win76] and Lynden-Bell [LB71, LB73] as applied to TDPAC.

To calculate the expression for the perturbation factor $G_{22}(t)$ in SRPAC we use the formalism of Blume [Blu68], Lynden-Bell [LB71, LB73] and Winkler [WG73, Win76]. This formalism is based on the stochastic theory approach. In this approach one separates the full system into the probe (nucleus) and its surroundings that can be replaced by an effective medium called heat bath governed by stochastic thermal motions. Heat bath and probe are connected by hyperfine interaction. Therefore the whole heat bath can be described by one parameter (in our case the direction of the EFG), the time evolution of which is governed by the stochastic motion. This stochastic motion is assumed to be a stationary Markov process, i. e. no memory effect exists. For a precise definition of the Markov process see e.g. [vK81]. Then, in the density matrix formalism (the definition of this formalism can be found in [Blu81]), the evolution of the studied system is described by the time-evolution operator $\hat{U}(t)$ [WG73]

$$\hat{U}(t) = \exp\left[\left(-\frac{i}{\hbar}\mathcal{H}^{\times} + \hat{R}\right)t\right] \tag{4.10}$$

where $\mathcal{H}^{\times}$ denotes the Liouville operator built on the Hamiltonian of the quadrupole interaction (see Appendix B) and $\hat{R}$ is the operator of the jump probability for the stochastic state. The operator $\mathcal{H}^{\times}$ is applied only to the nuclear state and the operator $\hat{R}$ only to the stochastic state of the heat bath. However, due to the matrix form of the operators, it is not possible to factorize the time-evolution operator into stochastic and nuclear parts. If it were possibles, then the perturbation factor could be expressed as a static perturbation factor multiplied by the relaxation function. In reality the quantum mechanical nature of the quadrupole interaction leads to a more complicated time evolution of the perturbation factor. This fact is known in literature as non-secular effect [Dat87].

To solve eq. (4.10), one has to introduce a suitable assumption regarding the nature of fluctuation of the orientation of the molecules in the heat bath, i.e., to give a description of the operator $\hat{R}$. We assume that the rotational relaxation is isotropic and happens by finite angular jumps. Then the main parameter that defines the relaxation process is the average time τ during which the molecule resides in a given orientation. The corresponding frequency parameter is the jump rate $\lambda = 1/\tau$.

At first we consider the finite angular jump model (FJM) which has been developed by Ivanov [Iva64] and later by Anderson [And72]. The idea of this model is simple. The molecule resides in a given orientation for a time τ before an angular jump through an Euler angle $\hat{\alpha} = (0, \alpha, 0)$ takes place [BDHR01]. Due to the isotropical character of the

relaxation, the 3-dimensional rotation $\hat{\alpha}$ here can be reduced to one characteristic jump angle α, which is the second parameter of this model. We consider the matrix element of the jump probability operator $\hat{R}$ in the angular momentum representation $|J, \mu\kappa)$ which is defined by the normalized Wigner rotation matrix elements [Win76] $\sqrt{(2J+1)/8\pi^2} D^{(J)}_{\mu\kappa}(\hat{\alpha})$. Then due to the isotropical character of the rotational relaxation

$$(J', \mu'\kappa'|\hat{R}|J, \mu\kappa) = \lambda_J^{FJM} \cdot \delta_{JJ'} \cdot \delta\mu\mu' \cdot \delta_{\kappa\kappa'} \tag{4.11}$$

the jump probability depends only on the total angular momentum J. For FJM the jump probability is

$$\lambda_J^{FJM} = -\lambda(1 - P_J(\cos\alpha)) \tag{4.12}$$

The important limit of this model appears in the case of an infinitesimally small jump angle α. Then the FJM reduces to the well-known rotational diffusion model (RDM) introduced by Debye to describe the rotational diffusion of a Brownian particle [Deb13]. This model is defined by one parameter, the rotational diffusion coefficient d as [Win76]

$$\lambda_J^{RDM} = -J(J+1)d \tag{4.13}$$

The FJM in the limit of small α reduces to

$$\lambda_J^{FJM} \xrightarrow[\alpha\to 0]{} -\lambda \cdot J(J+1)\left(\frac{\alpha}{2}\right)^2 \tag{4.14}$$

which makes a connection between the models by

$$d = \lambda\left(\frac{\alpha}{2}\right)^2 \tag{4.15}$$

The rotational diffusion model presents an extreme case of the rotational relaxation. The opposite case is presented by the strong collision model (SCM). In this model the angular jump has a random magnitude so that after the jump the molecule can find itself oriented in any direction independent of the previous state. The jump probability matrix element for SCM can be written as [Win76]

$$\lambda_J^{SCM} = -\lambda(1 - \delta_{J0}) \tag{4.16}$$

One can see that except zero angular momentum jumps, the probability is independent of angular momentum J. This is in contrast with FJM and RDM, where λ_J strongly depends on J. Combining all three models one can write

$$(J', \mu'\kappa'|\hat{R}|J, \mu\kappa) = -\lambda_J \cdot \delta_{JJ'} \cdot \delta\mu\mu' \cdot \delta_{\kappa\kappa'} \tag{4.17}$$

where the specific shape of λ_J is defined by the model. The physical meaning of λ_J can be understood if we introduce the rotational correlation function $C_J(t)$ [Dat87, BDHR01]

$$C_J(t) = \sum_\mu < D^{(J)^*}_{0\mu}(\hat{\alpha}(t)) D^{(J)}_{0\mu}(\hat{\alpha}(0)) > = < P_J(\cos(\hat{\alpha}(t) - \hat{\alpha}(0))) > \tag{4.18}$$

where the isotropical character of the relaxation is taken into account. This function is important in many experimental techniques, e.g. nuclear magnetic resonance, dielectric spectroscopy. Due to the Markov property of the rotational relaxation this function is exponential and can be written as [BDHR01]

$$C_J(t) = \exp(-\lambda_J t) \tag{4.19}$$

One can see that the quantity λ_J which appears in the calculation of the perturbation factor is the relaxation rate of the rotational correlation function of angular momentum J.

The time-evolution operator $\hat{U}(t)$ in the shape of eq. (4.10) together with the defined model for the rotational relaxation gives a formal answer to the question about the time evolution of the perturbation factor. But there is a still open question about the practical solution of this equation. There are several ways to do it: resolvent method [Dat87], series expansion method [WG73], eigensystem method [LB73, Win76]. Also one should notice that not for every model there is an analytical solution for the perturbation factor. For the straightforward numerical calculations we found quite convenient the eigensystem method which has been developed by Winkler in application to the TDPAC with spin $I = 5/2$ [Win76]. The procedure of the calculation of the perturbation factor $G_{22}(t)$ for the spin $I = 3/2$ is presented in Appendix D. One can notice that in our case the eigensystem problem reduces to the diagonalization of a 6×6 matrix. Also it is seen that the influence of the rotational relaxation to the perturbation factor reduces to 2 parameters λ_2 and λ_4 which are the relaxation rates of the second and the forth angular momentum correlation functions. Since both λ_2 and λ_4 are proportional to the jump rate in the considered models, it is convenient to replace them by another pair of parameters λ_2 and $q \equiv \lambda_4/\lambda_2$. The parameter q does not depend on the jump rate λ and describes the model of the relaxation. It is equal to 1 for SCM and 20/6 for RDM. The dependence of q on the jump angle α in FJM is shown in Fig. 4.6.

In general there is no analytical presentation of $G_{22}(t)$. However, for $q = 1$ (SCM) an analytical answer can be obtained. For this purpose the resolvent method which was developed by Dattagupta is quite convenient. In Appendix E we obtain the analytical expression for $G_{22}(t)$ in the SCM using this method.

As it was mentioned at the beginning of this section, the time evolution of the perturbation factor strongly depends on the ratio between the characteristic jump rate and the quadrupole splitting. Therefore we can separately consider the behavior of $G_{22}(t)$ in three regimes: the slow relaxation regime where $\lambda_2 \ll \Omega$, the fast relaxation regime where $\lambda_2 \gg \Omega$ and the intermediate regime where $\lambda_2 \sim \Omega$.

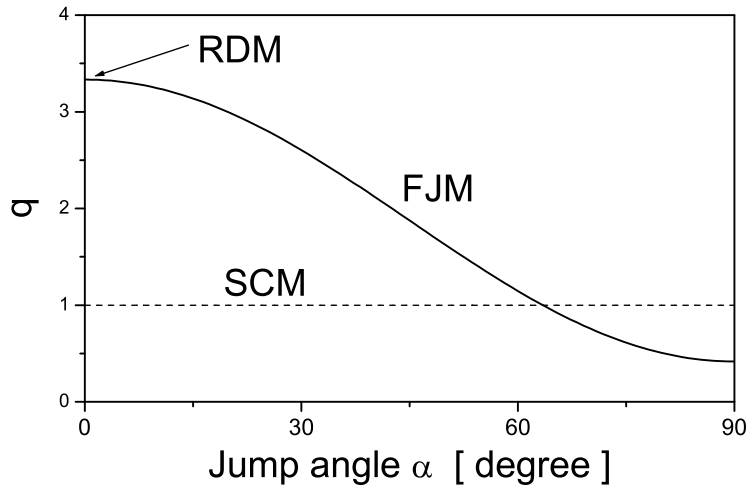

Figure 4.6: The parameter q as a function of jump angle α in the FJM. Additionally, the values of q for the SCM and the RDM are shown.

4.4.1 Slow relaxation regime

At first we consider the slow relaxation regime. The simulation of $G_{22}(t)$ for different values of λ_2 and q is shown in Fig. 4.7. In the case of $q = 1$ (SCM) the analytical approximation of the perturbation factor for $\lambda_2/\Omega \ll 1$ can be written as (see eq.(E.19))

$$G_{22}^{SCM}(t) \simeq \frac{1}{5}\mathrm{e}^{-4\lambda_2 t/5} + \frac{4}{5}\mathrm{e}^{-3\lambda_2 t/5}\cos(\Omega_e t - \phi) \tag{4.20}$$

$$\Omega_e = \Omega\left(1 - \frac{4\lambda_2^2}{25\Omega^2}\right) \tag{4.21}$$

$$\phi = \frac{4\lambda_2}{5\Omega} \tag{4.22}$$

One can see that the expression for $G_{22}(t)$ is similar to the static case (see eq.(4.6)) but due to the relaxation both terms are exponentially damped. Additionally the QB changes its frequency and phase. The damping rate is proportional to λ_2 with different proportionality coefficients for the hard core and for the oscillatory term. This is a consequence of the non-secular effect discussed above.

The time evolution of the spin is mainly governed by the precession around a quantization axis, so that the scattered signal is a periodic oscillation. The quantization axis is defined by the direction of the incoming radiation at time zero. With increasing time the orientation of the axis becomes distributed due to the molecular rotation. As result the amplitude of the oscillation decreases with time. The decrease is described by the correlation between the orientation at time zero and at time of reemission. In our case this

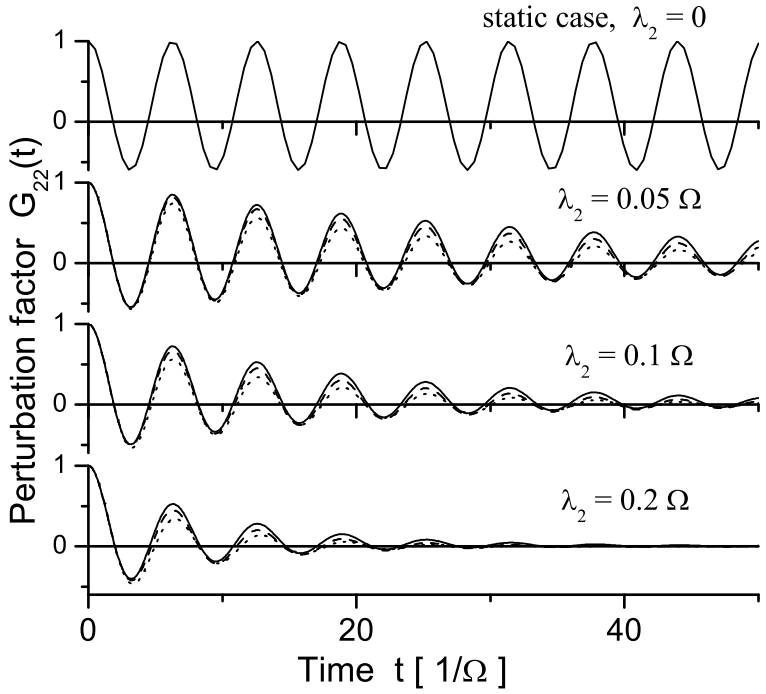

Figure 4.7: Simulation of the perturbation factor $G_{22}(t)$ in the static case and for various small values of λ_2. The solid line corresponds to $q = 0.2$, the dashed line to $q = 1$ (SCM) and the dotted line to $q = 20/6$ (RDM).

correlation function is an exponential function with rate proportional to λ_2. Therefore, the perturbation factor is the static perturbation factor describing the spin precession multiplied by an exponential decay describing the effect of rotation. However, due to the quantum mechanical nature of the spin variable, the change of the direction of the quantization axis additionally results in a mixing of the population of the spin states. This leads to different values of the exponential rates for the two terms in the perturbation factor. While both of them are proportional to λ_2, their ratio gives information about the characteristic jumps (model of the reorientation).

It is shown in Appendix D that in the general case the slow relaxation approximation of $G_{22}(t)$ can be written as

$$G_{22}(t) \simeq \frac{1}{5}\mathrm{e}^{-p_h t} + \frac{4}{5}\mathrm{e}^{-p_o t}\cos(\Omega_e t - \phi) \tag{4.23}$$

where the damping coefficients depend on q and λ_2 as

$$p_h = \lambda_2\left(\frac{2}{7} + \frac{18}{35}q\right) \tag{4.24}$$

$$p_o = \lambda_2\left(75 + 37q - \sqrt{1009q^2 - 450q + 225}\right)/140 \tag{4.25}$$

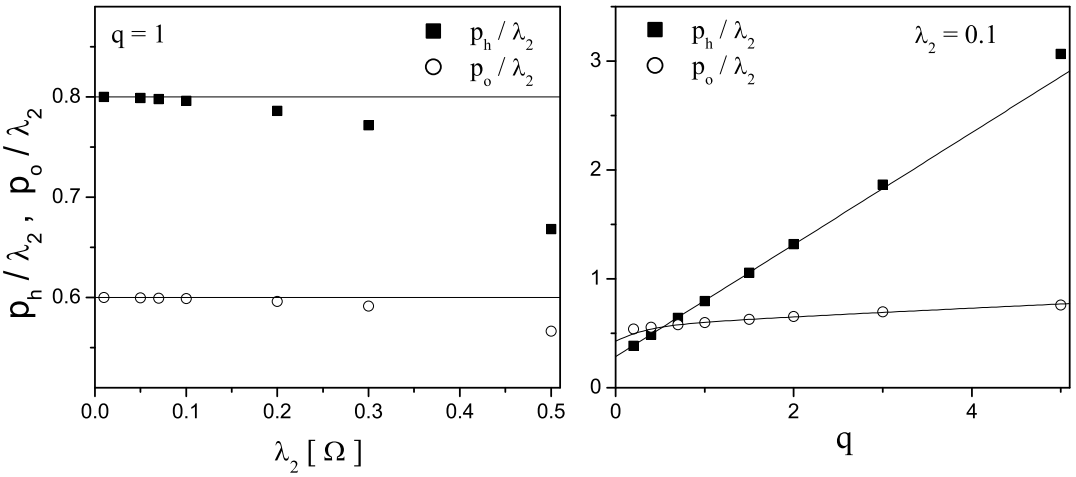

Figure 4.8: The values of p_h/λ_2 and p_o/λ_2 obtained from the fit of the perturbation factor by eq. (4.23). The perturbation factor was simulated by the procedure described in Appendix D with different values of λ_2 and q. The left side shows the linear dependence of p_h and p_o on λ_2 up to $\lambda_2 \lesssim 0.3$. The right side shows the dependence of p_h/λ_2 and p_o/λ_2 on q. The lines show the approximation of eqs. (4.24),(4.25).

The range of parameters where this approximation is correct was checked by fitting the numerical simulation of $G_{22}(t)$ according to Appendix D by eq. (4.23) with free parameters p_h and p_o . The obtained p_h and p_o, scaled by λ_2, are shown in Fig 4.8 as functions of λ_2 and q. The solid lines show the dependences obtained by eqs. (4.24),(4.25) . One can see that in the region of $\lambda_2/\Omega < 0.3$ and $0.2 < q < 5$ the approximation (4.23-4.25) works quite well. As a consequence one can say that the measurement of the damping of hard core and oscillatory term are necessary to obtain information about the relaxation rate and the mechanism of the relaxation. The ratio p_h/p_o is independent on λ_2 and is defined by the model of the rotational relaxation.

4.4.2 Fast relaxation regime

The fast relaxation regime is defined by $\lambda_2/\Omega \gg 1$. The simulation of the perturbation factor is shown in Fig. 4.9. One can see that the oscillations disappear and the time evolution of $G_{22}(t)$ is described by an exponential decay with a decay rate that decreases with increasing λ_2.

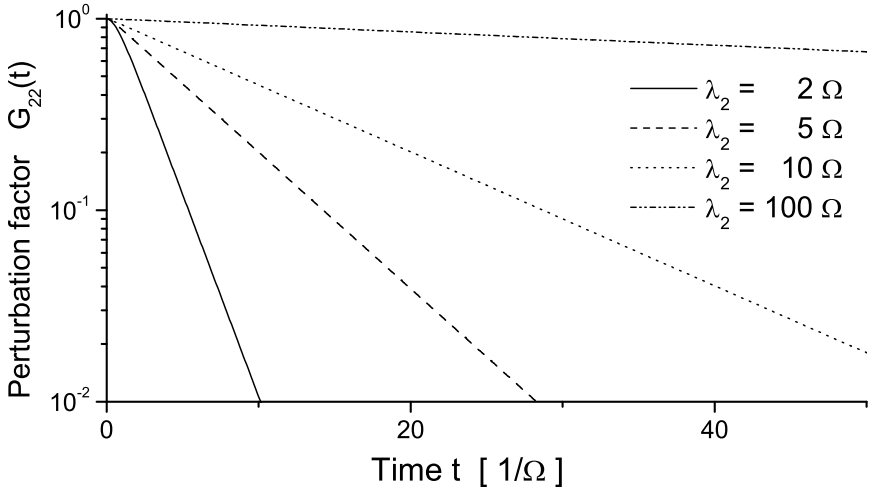

Figure 4.9: Simulation of the perturbation factor for various high values of λ_2/Ω.

The general solution for SCM reduces in the fast relaxation regime to (see eq. (E.20))

$$G_{22}^{SCM}(t) \simeq \exp\left(-\frac{4\Omega^2}{5\lambda_2}t\right) \tag{4.26}$$

The nucleus finds itself at time zero in a state with a certain direction of the quantization axis. Its spin starts to precess around this axis, but, since the jump rate is very fast, it can hardly precess at all before the axis jumps to a new direction. Since the nuclear spin can not follow such a rapid relaxation it sees an averaged EFG. With increase of the jump rate the averaged EFG decreases and therefore the rate of the spin motion decreases as well. As result the loss of the anisotropy which is produced by the spin motion slows down. In the case of an infinitively large value of the jump rate the ensemble of spins is frozen in the initial position and the perturbation factor stays at constant value.

The eq. (4.26) is consistent with the general result obtained by Abragam and Pound [AP53] in the fast relaxation regime, also called Abragam-Pound limit. For perturbations governed by quadrupole interaction and assuming that the relaxation does not change the absolute value of the EFG, one can write the perturbation factor for spin $I = 3/2$ in the fast relaxation regime as (see eqs. (13.291) and(13.294) in [SA75])

$$G_{22}(t) \simeq \exp\left(-\frac{4}{5}\Omega^2 < \tau_2 > t\right) \tag{4.27}$$

$$< \tau_2 > = \int_0^\infty \mathrm{d}t \cdot C_2(t) \tag{4.28}$$

where $< \tau_2 >$ is the usual definition of the mean relaxation time for the rotational correlation function $C_2(t)$. Taking into account the expression for $C_2(t)$ (see eq. 4.19) one obtains that $< \tau_2 >= 1/\lambda_2$ which reduces eq. (4.27) to eq. (4.26). The general expression for $G_{22}(t)$ is valid even in models of non-exponential decay of the rotational relaxation, like the stretched exponential relaxation with correct definition of $< \tau_2 >$. However, the dependence of $G_{22}(t)$ on λ_4 which was observed in the slow relaxation regime disappears in this regime. Therefore the information about the type of relaxation can not be obtained in the fast relaxation regime.

4.4.3 Intermediate relaxation regime

The intermediate regime is characterized by the relation $\lambda_2 \sim \Omega$. The behavior of the perturbation factor changes in this regime from damped oscillations to an exponential decay. The simulation of the perturbation factor in this regime is shown in Fig. 4.10 for various values of λ_2 and q.

It is shown above that the appearance of the rotational correlation function in $G_{22}(t)$ in the slow and fast relaxation regime is completely different. Whereas for the slow relaxation regime the correlation function is observed straightforward in time (taking into account the non-secular effect), only the integral of this function appears in the perturbation factor in the fast relaxation regime. In this sense we can consider the intermediate regime as a regime where the slow relaxation behavior is already overdamped and the fast relaxation behavior does not yet appear. Such a point of view corresponds to the fact that only the rather short-time region is important at this regime. The long-time tail of $G_{22}(t)$ approaches zero.

4.4.4 Short-time dynamics in restricted anglular range

Till now we considered a long-time (structural) relaxation that describes an irreversible dynamical processes. Now we consider the influence of fast rotational dynamics on the time evolution of the perturbation factor. This dynamics is presented by a rotation of the molecule in a restricted angular range around the equilibrium position, the libration. This process is reversible and qualitatively differs from the long-time dynamics. The effect of the short-time dynamics on $G_{22}(t)$ can be calculated precisely in the fast relaxation regime. An additional prefactor reflecting the decrease due to the fast librations appears in the rotational correlation function $C_2(t)$. This prefactor, which we call f_{rot}, is equivalent to the Lamb-Mössbauer factor and can be calculated as

$$f_{rot} =< P_2\left(\cos(\tilde{\alpha}(t) - \tilde{\alpha}(0))\right) >=< P_2\left(\cos(\tilde{\alpha}(t))\right) >= \frac{1}{4} + \frac{3}{4}\exp\left[-2 < \alpha^2 >\right] \quad (4.29)$$

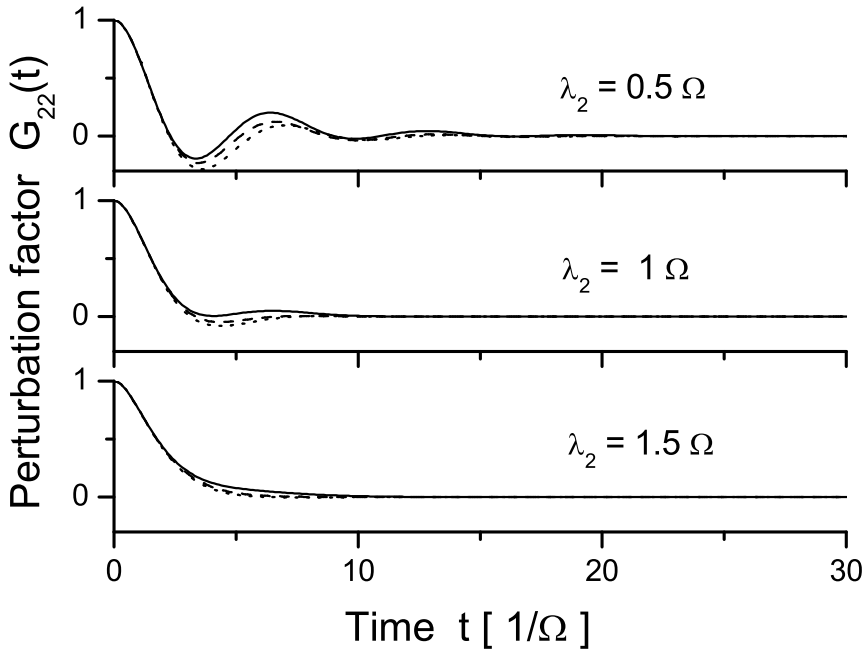

Figure 4.10: Simulation of the perturbation factor in the intermediate relaxation regime. The solid line corresponds to $q = 0.2$, the dashed line to $q = 1$ (SCM) and the dotted line to $q = 20/6$ (RDM).

where we assume that $\tilde{\alpha}(0) = 0$ is the equilibrium position and where we use for the angular motions the relation [LFC02]

$$< \mathrm{e}^{\imath c\alpha} >= \exp\left[-\frac{1}{2}c^2 < \alpha^2 >\right] \tag{4.30}$$

$< \alpha^2 >$ is the mean square angular displacement from equilibrium. Inserting this prefactor into $C_2(t)$ in eq. (4.28), we obtain $G_{22}(t)$ in the fast relaxation regime as

$$G_{22}(t) \simeq \exp\left(-\frac{4\Omega^2 f_{rot}}{5\lambda_2}t\right) \tag{4.31}$$

where f_{rot} describes the short-time dynamics and λ_2 describes the long-time final decay of the correlation function. Physically, the reversible uncorrelated in time fast angular motions in a restricted angle lead to an average of the quadrupole interactions over this angle. Therefore the influence of the short-time dynamics can be reduced to the scaling of the quadrupole splitting value as $\Omega = \Omega_0\sqrt{f_{rot}}$ where Ω_0 is the static value of the quadrupole splitting. We assume that this result is valid not only in the fast relaxation regime but in the slow relaxation regime as well. Taking into account small values of α

one can write

$$\Omega = \Omega_0 \cdot \left(1 - \frac{3}{4} < \alpha^2 >\right) \tag{4.32}$$

A similar result was obtained in NMR [BDHR01] and in electron spin resonance [Dzu96].

4.5 Influence of spatial and spin dynamics on NFS

4.5.1 Influence of spin dynamics

In Chapter 3 we have considered the influence of spatial dynamics on NFS. It was pointed out there that also time-dependent hyperfine interactions lead to a modification of the time evolution of NFS. Here, we present the theoretical description of this influence. Like in the case of SRPAC we consider a molecule in which a quadrupole interaction between nucleus and surroundings exists and where the direction of the EFG is defined by the molecular structure. The time evolution of the quadrupole interaction is defined by the rotation of the molecule and, respectively, by the rotation of the EFG. The approach used to explain the influence of the rotation on SRPAC can also be used in application to NFS. One can introduce the perturbation factor $G(t)$ which describes the time evolution of the density matrix, as done in eq.(2.27) of [Dat81]. The difference with respect to SRPAC is that in SRPAC only the perturbation of the excited state is considered whereas NFS is influenced by the simultaneous perturbation of excited and ground states. Correspondingly, the NFS density matrix is formed by both excited and ground states. Also by contrast to SRPAC the perturbation factor describes the time evolution of the amplitude of scattering. Nevertheless the time evolution of the density matrix is defined by the same eq. (4.10), only the action of the Liouville operator representing the quadrupole interaction on the density matrix will be different.

The self-correlation function $K(t)$ of NFS which was introduced in eqs. (3.4) and (3.16) is given as

$$K(t) = \mathrm{e}^{-t/2\tau_0} \cdot G(t) \tag{4.33}$$

This function also gives the time evolution of the NFS amplitude in the kinematical approximation.

In the static case the quadrupole interaction results in a simple expression for the perturbation factor (see eq. (3.13))

$$G(t) = \cos(\Omega t/2) \tag{4.34}$$

The influence of rotation on $G(t)$ has been calculated in [DB74, Dat76] for the RDM and the SCM by the resolvent method. The result was obtained as a Laplace image $G(p)$.

Making the inverse Laplace transformation we obtain the expression for $G(t)$ which can be written for both models as

$$G(t) = \mathrm{e}^{-\lambda_2 t/2} \cos\left(\frac{\Omega_e t}{2} - \phi\right) \tag{4.35}$$

$$\phi = \arctan\left(\frac{\lambda_2}{\Omega_e}\right) \tag{4.36}$$

$$\Omega_e = \Omega\left(1 - \lambda_2^2/\Omega^2\right)^{1/2} \tag{4.37}$$

where λ_2 is the same as in SRPAC and is defined by the model of rotation as in the previous section. The corresponding expression for the NFS intensity in kinematical approximation is given as

$$I(t) = I(0) \cdot \mathrm{e}^{-t/\tau_0} \cdot \mathrm{e}^{-\lambda_2 t} \cdot \left(1 + \cos(\Omega_e t - 2\phi)\right)/2 \tag{4.38}$$

The time evolution of the perturbation factor and the NFS intensity are shown in Fig. 4.11 for several values of the relaxation parameter λ_2. The time evolution of the NFS intensity in the static case is defined by a natural decay modified by a QB. This time evolution is similar to that of SRPAC with the contrast $K = 1$ in eq. (4.7).

Similar to SRPAC, the time evolution of the NFS intensity behaves differently for small and large values of the relaxation rate λ_2 - slow and fast relaxation regimes can be defined. In the slow relaxation regime, the time evolution is characterized by a QB damped in time. When λ_2 becomes larger than Ω, Ω_e becomes complex and the cosine function goes to a hyperbolic cosine. The QB is not seen any longer, and in the fast relaxation regime, where $\lambda_2 \gg \Omega$, eq. (4.38) is approximated by an exponential decay

$$I(t) \simeq I(0) \cdot \mathrm{e}^{-t/\tau_0} \cdot \exp\left(-\frac{\Omega^2}{2\lambda_2} t\right) \tag{4.39}$$

One can see that the influence of spin relaxation on SRPAC and NFS is similar but differs in details. The SRPAC intensity consists of isotropic and anisotropic contributions, the first one does not depend on relaxation. On the other hand, NFS includes only an anisotropic contribution and all intensity is damped due to relaxation. The NFS perturbation factor does not include a hard core term, only a QB term is present. As result, one can not get information about the model of rotation, which was possible in SRPAC from comparison of the damping rate of the hard core and QB terms. Besides that, the effective frequency Ω_e of the QB which decreases relative to Ω due to relaxation, decreases differently in SRPAC and in NFS. As a result, different QB frequencies are seen in NFS and SRPAC.

Eq. (4.39) gives the kinematical approximation for the NFS intensity. The general expression can not be obtained analytically. The procedure developed in Appendix A has to be used in order to take into account multiple scattering. However, the exponential

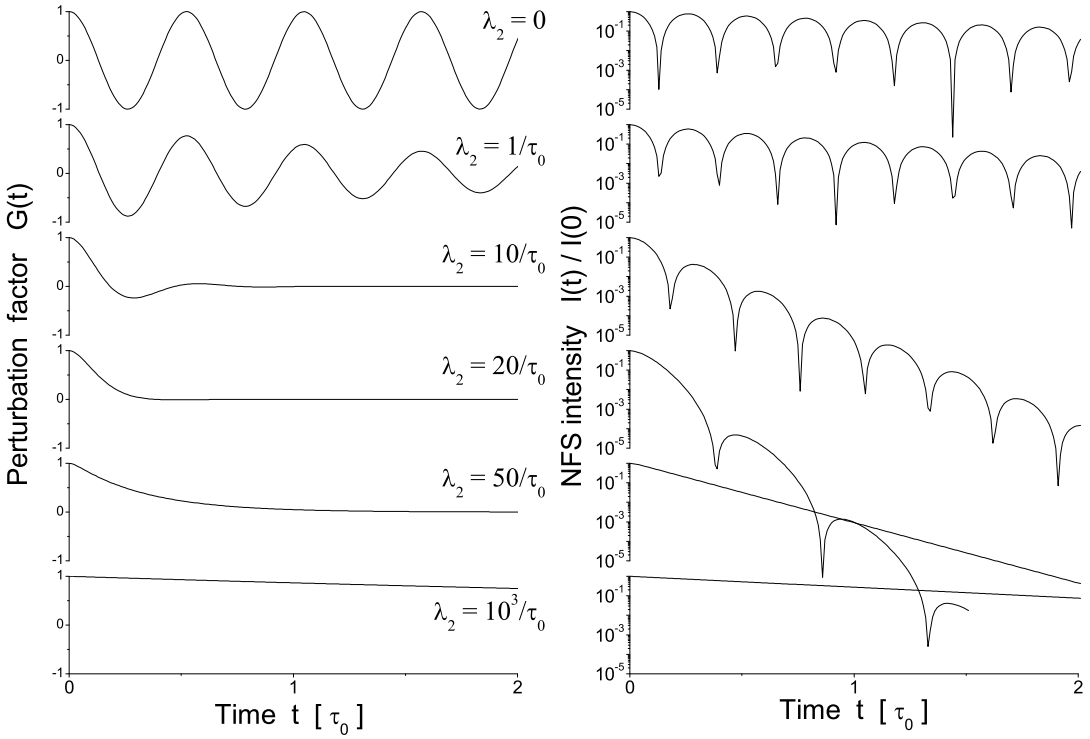

Figure 4.11: Simulation of the time behavior of the perturbation factor and of the NFS intensity in kinematical approximation for several values of the relaxation rate λ_2. The quadrupole splitting was chosen as $\hbar\Omega = 24\Gamma_0$.

character of the damping of $G(t)$ in both the slow and the fast relaxation regime leads to factorization of the multiple scattering and damping terms similar to eq. (3.19). The cosine part of $G(t)$ in the slow relaxation regime can be extracted from the multiple scattering correction in the way presented in eq. (3.15). However, this approximation is valid for $\xi/\Omega_e\tau_0 < 1$. In the intermediate relaxation regime, where $\lambda_2 \sim \Omega$, $\Omega_e \sim 0$ and the last approximation is not valid. Then the intensity has to be calculated numerically.

4.5.2 Influence of spin and spatial dynamics

It was assumed till now that the molecules experienced only one type of motion: translation or rotation. In general one has to consider the time evolution of the nuclear ensemble governed by both types of motion. This task has been solved by Dattagupta [Dat75, Dat76] who applied the following model of relaxation. The nucleus resides in a given state for a time τ. The corresponding relaxation rate is $\lambda = 1/\tau$. It jumps instantaneously to a new site in space and in angle. The angular jump is described by the model

of rotation which is discussed in Section 4.4 and is defined by λ_2. The jump in space is introduced in a similar way. The spatial analogue of the FJM represents the jump of the molecule over a distance a. The corresponding jump probability in the momentum space can be introduced as [Dat75]

$$\lambda_t(k) = \lambda \left(1 - \frac{\sin ka}{ka}\right) \tag{4.40}$$

This value represents the decay rate of the exponential van-Hove self-intermediate function $F_s(t)$. The momentum k is fixed by resonance energy, $k = 7.31$ Å^{-1} for ^{57}Fe, and in the following we omit the dependence of λ_t on k.

The eq. (4.40) simplifies in the hydrodynamical approximation where a is assumed to be small. Then

$$\lambda_t \simeq \lambda k^2 a^2/6 = Dk^2 \tag{4.41}$$

where the diffusion coefficient D is introduced. This approximation is similar to the RDM for the rotational motion.

The model presented above depends on three parameters which describe the jump frequency and the characteristic jump angle and distance. We introduce these parameters via λ, λ_2 and λ_t. The NFS intensity in the kinematical approximation can be obtained from [Dat75, Dat76] by Laplace transformation and proper replacement of the variables that results in

$$I(t) = I(0) \cdot \mathrm{e}^{-t/\tau_0} \cdot \mathrm{e}^{-2\lambda_{NFS} t} \left(1 + \cos(\Omega_e t - 2\phi)\right)/2 \tag{4.42}$$

$$\lambda_{NFS} = \lambda_t + \tilde{\lambda}_2/2 \tag{4.43}$$

$$\phi = \arctan\left(\frac{\tilde{\lambda}_2}{\Omega_e}\right) \tag{4.44}$$

$$\Omega_e = \Omega \left(1 - \frac{\tilde{\lambda}_2^2}{\Omega^2}\right)^{1/2} \tag{4.45}$$

$$\tilde{\lambda}_2 = \lambda_2 \left(1 - \frac{\lambda_t}{\lambda}\right) \tag{4.46}$$

This set of equations is similar to the one obtained for pure rotational relaxation (see eqs. (4.35)-(4.38)). The difference is an additional exponential damping due to the translational relaxation and the effective decrease of λ_2 to $\tilde{\lambda}_2$. This decrease can be explained as follows. The spatial motion of the molecule leads to the cancelation of the contribution of the corresponding wavelet to the coherent scattering. Therefore, any subsequent molecular rotation has to be excluded from the consideration.

The main feature of the NFS intensity which will be considered in the experiment is the additional decay with decay rate $2\lambda_{NFS}$. This parameter can be rewritten as

$$2\lambda_{NFS} = \lambda_2 + \lambda_t \left(2 - \frac{\lambda_2}{\lambda}\right) \tag{4.47}$$

The value of λ_2/λ depends on the model of rotation. For the two extremal cases of the RDM and SCM it is equal to 0 and 1. Therefore, the coefficient of λ_t can vary in the range from 2 to 1 depending on the model of rotation. We can assume that the variation of λ_t with temperature occurs much faster than the temperature variation of the rotational model. As result, we can say that the additional decay rate of the NFS intensity is formed by sum of the rotational relaxation rate λ_2 and the effective translational relaxation rate $\tilde{\lambda}_t$ which is proportional to the real rate of translation λ_t with the scaling coefficient between 1 and 2. In the following we will make no difference between λ_t and $\tilde{\lambda}_t$ and will use following equation

$$2\lambda_{NFS} = \lambda_2 + 2\lambda_t \tag{4.48}$$

with corresponding definition of λ_t. Also it is important to notice that for any model of rotation $2\lambda_{NFS}$ in eq. (4.47) will be larger than the sum of λ_2 and λ_t. If λ_2 derived from SRPAC is equal to $2\lambda_{NFS}$ derived from NFS it unambiguously means that $\lambda_t = 0$.

The presented result was derived in the model where both translational and rotational dynamics are defined by the same jump frequency. However, the eq. (4.48) is valid also in the general case of the different frequencies. The jump frequency λ is significant for the rotational dynamics since the time evolution is described by the new operator after each jump. On the other hand, the operation of the spatial jump commutates with the time evolution. Therefore, all equations above are valid also for the case when the translational dynamics is defined by other frequency λ'. Here, the eq. (4.41), for example, is rewritten as

$$\lambda_t = \lambda' k^2 a^2/6 = \lambda \cdot \frac{\lambda'}{\lambda} k^2 a^2/6. \tag{4.49}$$

where $(\lambda'/\lambda)k^2a^2/6$ is the effective jump probability increased/decreased due to the difference in the frequencies.

The generalization of the kinematical approximation of eq. (4.42) which takes into account multiple scattering can be done in the way discussed in the previous section.

Chapter 5

Experimental

In this chapter the setups for the NFS and SRPAC measurements are introduced and components are described. Several methodological aspects of SRPAC are discussed: the influence of the coherent scattering on SRPAC; different ways to obtain pure incoherent scattering; the dependence of SRPAC on the geometry of the experiment.

5.1 Experimental setup

In both NFS and SRPAC experiments one studies the time dependence of the delayed scattered intensity following the excitation of a nuclear ensemble by the short X-ray pulse (typically 100 ps). Both scattering channels can be measured in parallel. In Fig. 5.1 the typical setup is shown.

The undulator produces an X-ray beam with an energy width $\Delta E \approx 300$ eV. Radiation with energy outside a μeV window centered at resonance energy E_0 does not undergo resonant interaction with the nuclei of the target. Therefore this part of radiation should be eliminated as much as possible in order to reduce the load on the detectors. This monochromatization is achieved in two steps. A high-heat-load premonochromator (PM) has the task of handling the heat load of the "white" radiation produced by the undulator and reducing the energy bandwidth of the radiation to the eV region. This is achieved with two Si(1 1 1) reflections arranged in a non-dispersive setting [RC96]. A second step of monochromatization is achieved with a high resolution monochromator (HRM) which typically reduces the energy bandwidth down to $1 - 10$ meV. A nested design of the HRM was used with four successive reflections on two nested channel-cut crystals. The Si(4 2 2) reflection for the outer crystal and Si(12 2 2) for the inner one give an energy bandwidth $\Delta E \approx 6.4$ meV [IYI$^+$92]. Another setup uses only the outer crystal of the HRM in reflection Si(8 2 2) which gives $\Delta E \approx 150$ meV.

After the interaction with the sample, the scattered photons have to be detected. As

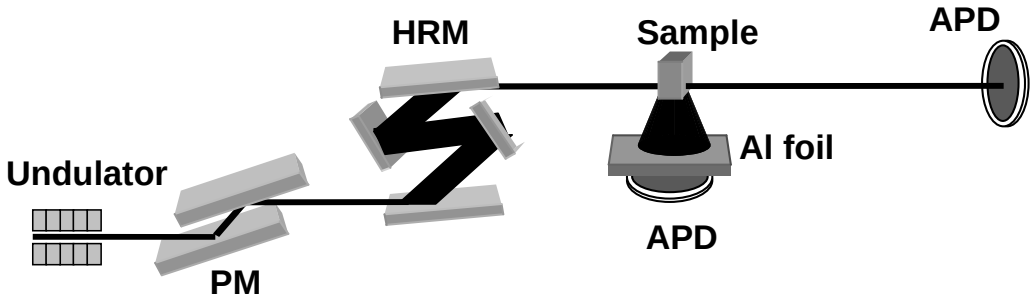

Figure 5.1: Typical setup for NFS/SRPAC measurements. The flash of SR light generated by the electrons in the undulator is monochromatized in two steps by a high-heat-load pre-monochromator (PM) and a high resolution monochromator (HRM). The signal scattered by the sample is recorded by fast detectors formed by avalanche photo-diodes (APD). The NFS signal is observed by a detector in the forward direction, and the SRPAC signal is observed by a detector below the sample. According to Fig. 4.3 this corresponds to $\vartheta = 0°$. The second detector is covered by an Al foil.

the nuclear scattering has to be separated in time from the electronic one, fast detectors are required (with time resolution of ∼1 ns). Moreover these detectors should have a fast recovery time, to be able to stand a rather intense pulse of X-rays (the prompt pulse, typically of the order of $10^7 \div 10^9$ photons/s) and a few ns later to count the delayed photons with much lower intensity (typically $10^{-1} \div 10^3$ photons/s). Avalanche photo-diodes (APD) are normally used for this purpose [BRM97], as they have the required characteristics together with a very low background ($\sim 10^{-2}$ Hz).

The NFS signal is recorded by the detector in the forward direction far away from the sample (∼1 m). As the coherent scattering is well collimated in forward direction no loss of the signal due to divergence of the beam occurs. At the same time the part of the 4π halo formed by incoherent scattering does practically not contribute to the signal recorded by this detector.

The SRPAC intensity is recorded by a detector situated close to the sample (5÷30 mm) usually in 90^o geometry below the sample. The choice of the detector position is defined by the optimum flux of the useful signal and will be discussed in the next section. The SRPAC detector is covered by an Al foil. The nuclear resonant fluorescence with 14.4 keV energy of the scattered photons is accompanied by atomic fluorescence whose probability is 8 times higher for ^{57}Fe. This process mainly occurs through emission of 6.4 keV photons. This part of the scattered radiation is eliminated by introducing the Al foil. The attenuation lengths for these two energies are $l_{6.4} \approx 40$ μm and $l_{14.4} \approx 440$ μm, respectively. An Al foil with thickness 320 μm transmits ∼ 50 % of the nuclear fluorescence and only ∼ 0.03 % of

the atomic fluorescence. This gives us the possibility to neglect the atomic fluorescence signal.

Standard fast timing electronics [Bar01] is used to process the signal from the APDs. A reference signal from the radio frequency system of the storage ring provides the synchronization of the electronics with the incoming pulse.

5.2 Methodical aspects of SRPAC

Whereas NFS and NIS were studied extensively during the last decade, SRPAC is a new method that requires methodological experimental studies. In this section two aspects of this method are analyzed experimentally: the dependence of the scattering on position and size of detector and sample and the influence of NFS to SRPAC. The experiments were performed with a glass former dibutylphthalate doped by ferrocene (DBP-FC), which will be described in Chapter 5. The nuclei in the sample experience a static quadrupole interaction which is isotropic over the sample.

5.2.1 Dependence on the geometry of the experiment

It was shown in the theoretical section that the essential part of SRPAC, the anisotropy $A_{22}G_{22}(t)$, can be extracted from the scattered intensity I(t) as (see eq. (4.3))

$$A_{22}G_{22}(t) = 1 - I(t)/\tilde{I}_0 \cdot \mathrm{e}^{t/\tau_0} \tag{5.1}$$

where $\tilde{I}_0 = I_0\Delta\Omega/4\pi$ can be easily obtained from the fit. The anisotropy is factorized into the perturbation factor and the anisotropy coefficient. The perturbation factor, $G_{22}(t)$, describes the time evolution of scattering and does not depend on the geometry of the experiment. Therefore, the time evolution of the anisotropy is the same in every direction taking into account the anisotropy coefficient A_{22}. In the following we check this feature in experiment.

The SRPAC intensity was measured at two temperatures, 200 and 296 K, which correspond for the investigated sample to the slow and fast relaxation regimes, respectively. For each temperature two measurements were performed with the detector in 90 degrees to the beam in vertical and horizontal directions. With respect to Fig. 4.3 this corresponds to the polar angle $\vartheta = 0°$ and 90° respectively. The results of the measurements are shown in Fig. 5.2. At $T = 200$ K quantum beats are seen in the time evolution of the intensity which are in antiphase for the horizontal and vertical directions. The perturbation factor extracted from the intensity is the same for both directions within experimental error. The corresponding anisotropy coefficients are $A_{22}^{ver} = 0.38$ and $A_{22}^{hor} = -0.2$. They are not the same as in the ideal case $A_{22}^{ver} = 0.5$ and $A_{22}^{hor} = -0.25$ due to the finite sizes of the

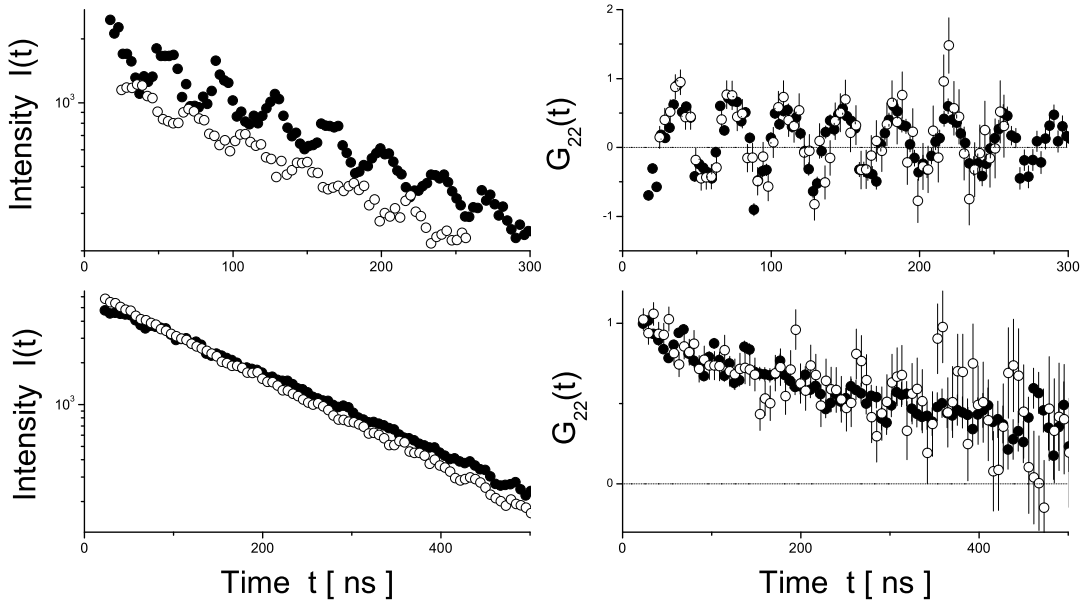

Figure 5.2: Comparison of the SRPAC intensity $I(t)$ (left side) and perturbation factor $G_{22}(t)$ (right side) on DBP-FC for the detector being at 90^o to the incoming SR and in the horizontal (open circles) and vertical (solid circles) position with respect to the plane of the synchrotron. The upper part corresponds to $T = 200$ K where almost static perturbations are observed, the lower part corresponds to $T = 296$ K where fast relaxation is observed.

detector and the sample. At $T = 296$ K the quantum beats are overdamped. A slow transition of the signal into a final natural decay at large times is here the characteristic feature of the intensity recordered by both detectors. This transition occurs via deceleration of the decay for scattering in the horizontal direction and via acceleration of the decay for scattering in the vertical direction. The perturbation factor again follows the same time evolution for both directions. The obtained anisotropy coefficients are $A_{22}^{ver} = 0.38$ and $A_{22}^{hor} = -0.24$. Here the experiments demonstrate that different geometrical conditions yield nevertheless the same perturbation factor $G_{22}(t)$.

This independence of the perturbation factor of the scattering direction allows one to put the detector in any position around the sample. Most convenient setup is the vertical direction since the maximum anisotropy is observed at this scattering angle. This position of the detector was used in the following experiments.

The second geometrical parameter that appears in the expression for the SRPAC intensity (eq. (4.3)) is the solid angle $\Delta\Omega$ subtended by the detector on the sample. If the size of the detector is fixed then $\Delta\Omega$ is defined by the distance between the detector

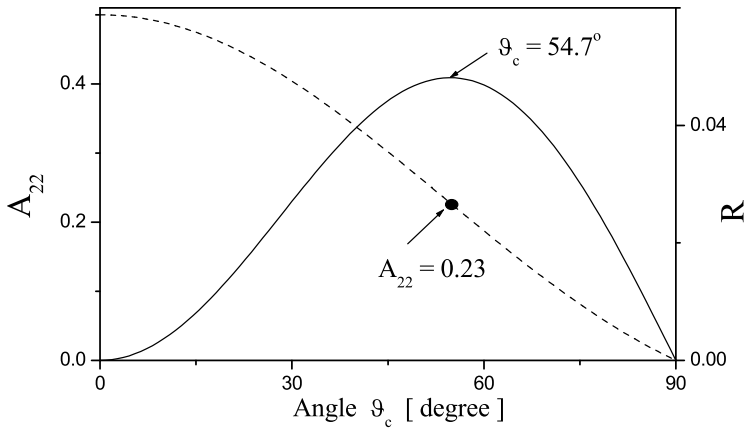

Figure 5.3: The dependence of the anisotropy coefficient A_{22} (dashed line) and of the efficiency function R (solid line) on the polar angle ϑ_c covered by the detector.

and the sample. When the detector is far away from the sample, $\Delta\Omega \sim 0$, the observed countrate will be close to zero and no SRPAC signal will be detected. In the opposite case, when the detector is close to the sample, $\Delta\Omega \sim 2\pi$, the countrate will be maximal but the anisotropy coefficient is $A_{22} \sim 0$ due to spatial average. Therefore, between these two extreme cases an optimal angle (distance) exists. The part of the scattered intensity connected with the perturbation factor in eq. (4.3) is proportional to

$$R = \frac{\Delta\Omega}{4\pi} A_{22} \tag{5.2}$$

which can be considered as an efficiency function.

For simplification let us consider a detector of cylindrical form with its axis lying along the vertical axis. Then, the setup will be symmetrical around the vertical axis and the solid angle $\Delta\Omega$ can be written as $\Delta\Omega = 2\pi(1 - \cos\vartheta_c)$, where the polar angle ϑ_c is the angle between vertical axis and the direction to the border of the detector. Inserting this condition to the expression for A_{22} (4.4) we obtain

$$A_{22} = \frac{\cos\vartheta_c(1 + \cos\vartheta_c)}{4} \tag{5.3}$$

$$R = \frac{\cos\vartheta_c(1 - \cos^2\vartheta_c)}{8} \tag{5.4}$$

The dependence of A_{22} and R on the angle ϑ_c is shown in Fig. 5.3. One can see that the anisotropy coefficient has a maximal value 0.5 for $\vartheta_c = 0$ and decreases when ϑ_c increases. The efficiency R is zero for the extremal angles and shows a maximum at $\vartheta_{cr} \simeq 54.7^o$. This angle corresponds to an anisotropy coefficient $A_{22} \simeq 0.23$.

The obtained optimum angle was calculated assuming a detector of cylindrical form and a point-like sample. The real experimental situation requires to take into account the

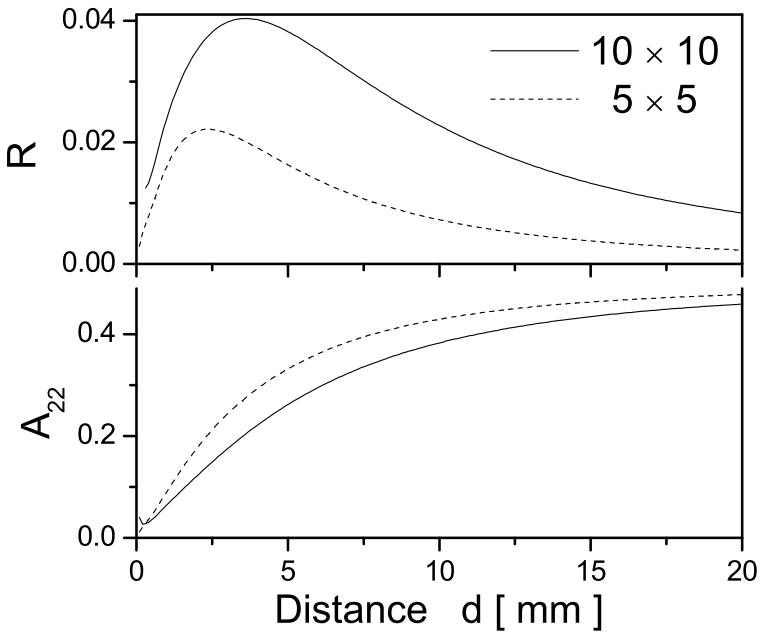

Figure 5.4: The dependence of the anisotropy coefficient A_{22} and of the efficiency function R on the distance d between detector and sample for the 5×5 mm^2 and 10×10 mm^2 detectors.

sizes of sample and detector. The sample has the surface 10×2 mm^2 where 2 mm is the horizontal width of the beam. Detectors of square areas 5×5 mm^2 and 10×10 mm^2 were used in the vertical direction. The dependence of A_{22} and R on the distance d between detector and sample is shown in Fig. 5.4. One can see that the maximum efficiency corresponds to the distance $2-5$ mm depending on the type of detector. The characteristic anisotropy coefficient for the optimal distance is around 0.25 which agrees with the simple case presented in figure 5.3

For the experimental study of the dynamics the detector 10×10 mm^2 was chosen and the distance between detector and sample was $d = 10 \pm 1$ mm. The anisotropy coefficient for these conditions is $A_{22} = 0.38 \pm 0.015$.

5.2.2 Contributions to 4π scattering produced by NFS

The incoherent nuclear scattering is not the only channel of scattering which produces delayed radiation into 4π. Also the combination of NFS and subsequent Rayleigh scattering can direct delayed radiation into the full solid angle [SK95]. This additional contribution can be so strong that it completely overshadows the SRPAC signal. Its strength is proportional to the NFS signal.

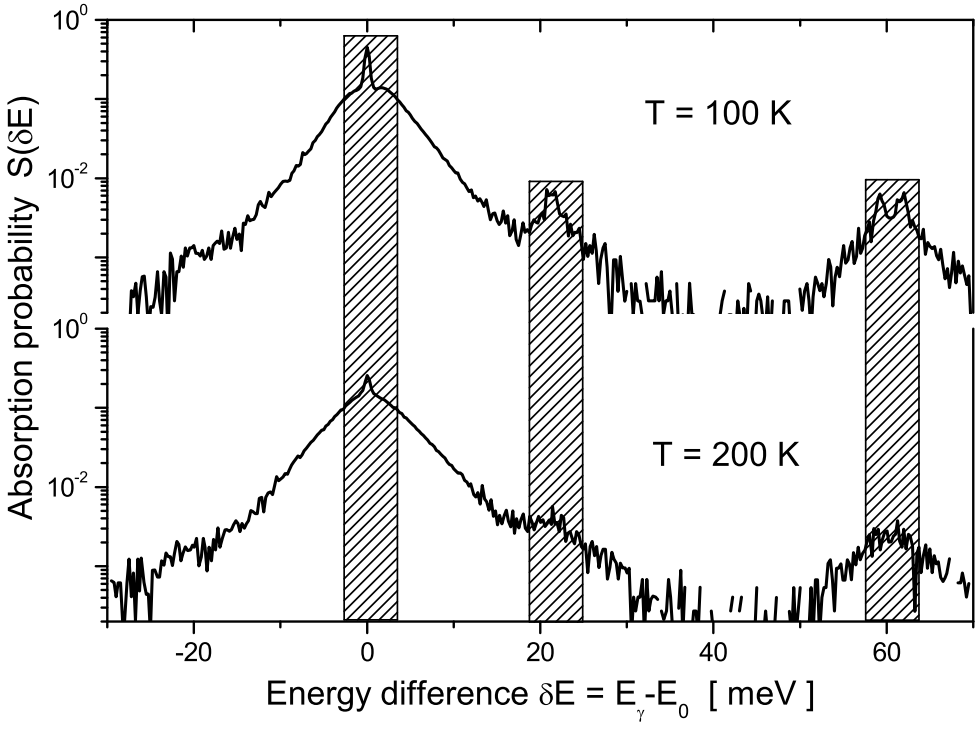

Figure 5.5: The probability of the resonance absorption $S(\delta E)$ as a function of the energy difference δE between energy of the incoming photon E_γ and resonant energy E_0. The hatched rectangles show the positions of the HRM used in the present experiment.

There are several cases when pure SRPAC is observed. The first and evident case is when no NFS exists. Since the NFS intensity is proportional to f_{LM}^2, this case is realized when $f_{LM} \sim 0$. By this way one can favorably apply SRPAC to studies of soft condensed matter. It is particularly suited for investigation of glass formers in the temperature range where MS and NFS are not applicable.

When f_{LM} is not zero and NFS is dominant, another way to see pure SRPAC has to be explored. This way had been used first by Baron [BCR+96]. The energy of the incoming radiation is tuned out of resonance by $10 \div 100$ meV. The resonant absorption occurs with creation/annihilation of phonon, which prohibits nuclear coherent scattering.

The glass former DBP-FC is a convenient sample to study how strong can be the contribution into 4π connected with NFS. The Lamb-Mössbauer factor drastically decreases with temperature so that measuring the incoherent signal at several temperatures one can obtain completely different contributions of NFS-Rayleigh scattering. Two temperatures were chosen: 100 and 200 K. An almost static quadrupole interaction describes the perturbation of the nuclear ensemble for both temperatures. At the same time, the

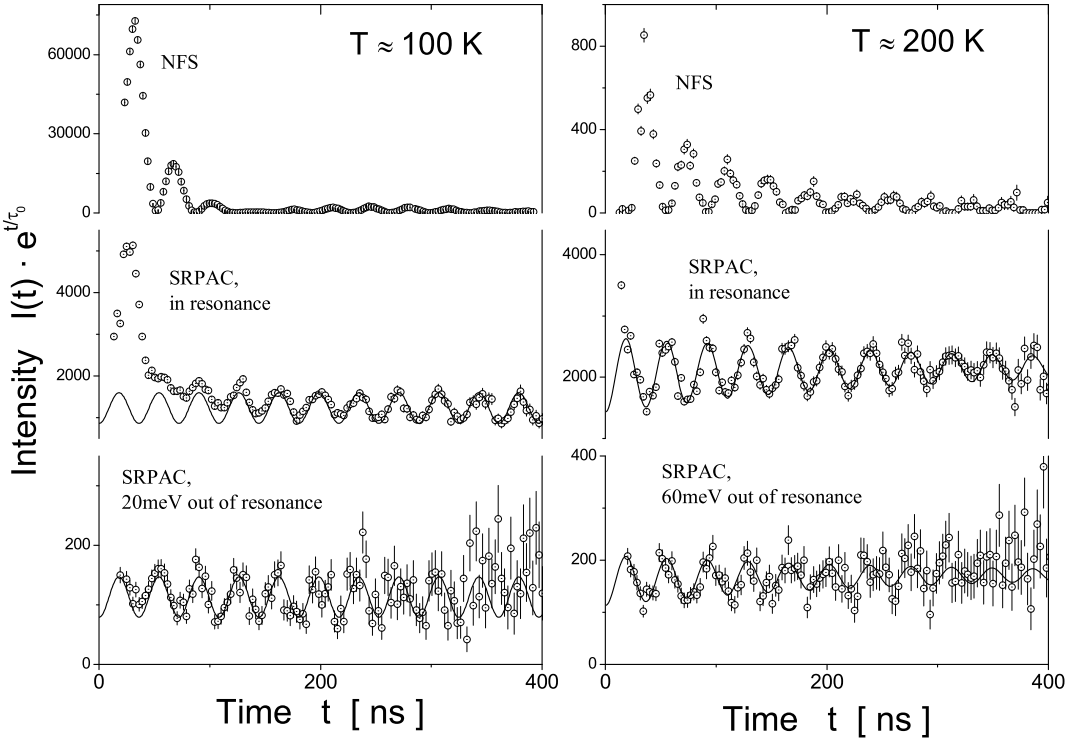

Figure 5.6: Comparison of the delayed intensity divided by natural decay measured by three methods: NFS, SRPAC in resonance and SRPAC out of resonance. The left side shows data at 100 K ($f_{LM} \approx 0.36$) and the right side shows data at 200 K ($f_{LM} \approx 0.004$). The solid lines show fits of the SRPAC intensity according to theory.

Lamb-Mössbauer factor is 0.36 for 100 K and 0.004 for 200 K, i.e. decreases by a factor of ~ 100. The energy of the incoming radiation was chosen "in resonance" and "out of resonance".

The probability of the resonant absorption $S(\delta E)$ as a function of the energy difference δE between energy of the incoming photon E_γ and the resonant energy E_0 is shown in Fig. 5.5 for DBP-FC at 100 and 200 K. The peak at $\delta E = 0$ corresponds to the elastic and quasielastic absorption. Its amplitude slows down with temperature. The other part of $S(\delta E)$ represents the absorption with creation/annihilation of phonons. A pronounced feature of the absorption probability is the existence of two peaks at $\delta E \sim 20$ meV and $\delta E \sim 60$ meV. The hatched rectangles in Fig. 5.5 show the positions of the HRM used in the experiment. The position "in resonance" is centered at E_0 and covers ~ 50 % of the absorption probability. The other positions "out of resonance" are adjusted to the energy of the side peaks and cover $1 - 2$ % of the absorption probability.

Fig. 5.6 shows for two temperatures three types of scattering which were measured:

NFS, incoherent scattering "in resonance" and incoherent scattering "out of resonance" which is pure SRPAC. The incoherent scattering in resonance is the sum of SRPAC the strength of which is a constant with temperature and NFS-Rayleigh scattering the strength of which decreases with temperature as f_{LM}^2. At 200 K, where f_{LM} is small, the incoherent scattering "in resonance" consists of pure SRPAC. On the contrary, at 100 K, the contribution of NFS-Rayleigh scattering is relatively large which is clearly seen in the figure. However, this contribution mainly appears at early times, below 150 ns in the figure. This is due to the redistribution of NFS scattering to smaller times for a large effective thickness. This fact allows us to measure SRPAC "in resonance" using a time window which is cut at small times. As it is seen in the figure, the beginning of this time window has to be where the base line of the QB becomes a constant.

Chapter 6

Study of LGT dynamics by NFS and SRPAC

This chapter is dedicated to the application of SRPAC and NFS to the study of dynamics of the LGT. In the first section a review of MS studies of the LGT is presented and questions, which have to be clarified, are pointed out. The used glass former is described in Section 6.2. After that the study by SRPAC and NFS is presented and the treatment of the data is explained. The obtained results are discussed in the next section and are compared with results of dielectric spectroscopy. The last section is dedicated to the extraction of information about the stretching of the relaxation function from NFS measurements.

6.1 Previous studies of the LGT by Mössbauer spectroscopy

The sensitivity of MS to dynamics on the time scale up to μs (down to neV on the energy scale) and on the Ångstrom length scale makes it a convenient tool to study relaxation processes in viscous liquids. This was recognized immediately after the discovery of the Mössbauer effect [CS63, BEHW63]. However, the nuclear resonance measurements require a resonant isotope in the sample, for practical purposes this means a decent amount of iron in the sample. This strongly restricts the selection of suitable systems. The problem can be overcome by dissolving a small amount of iron-containing molecules in a glass-forming liquid. Such molecules can be considered as a probe inserted to the glass former, or as the second component of a binary mixture. This method was widely used to study dynamics in organic glass formers. One of the often used systems is the ferrous ion Fe^{2+} dissolved in a glycerol-water mixture [CS63, AM72, CHR75, NFP91]. Another class of glass formers was obtained by dissolving ferrocene in organic glass formers: dibutyl

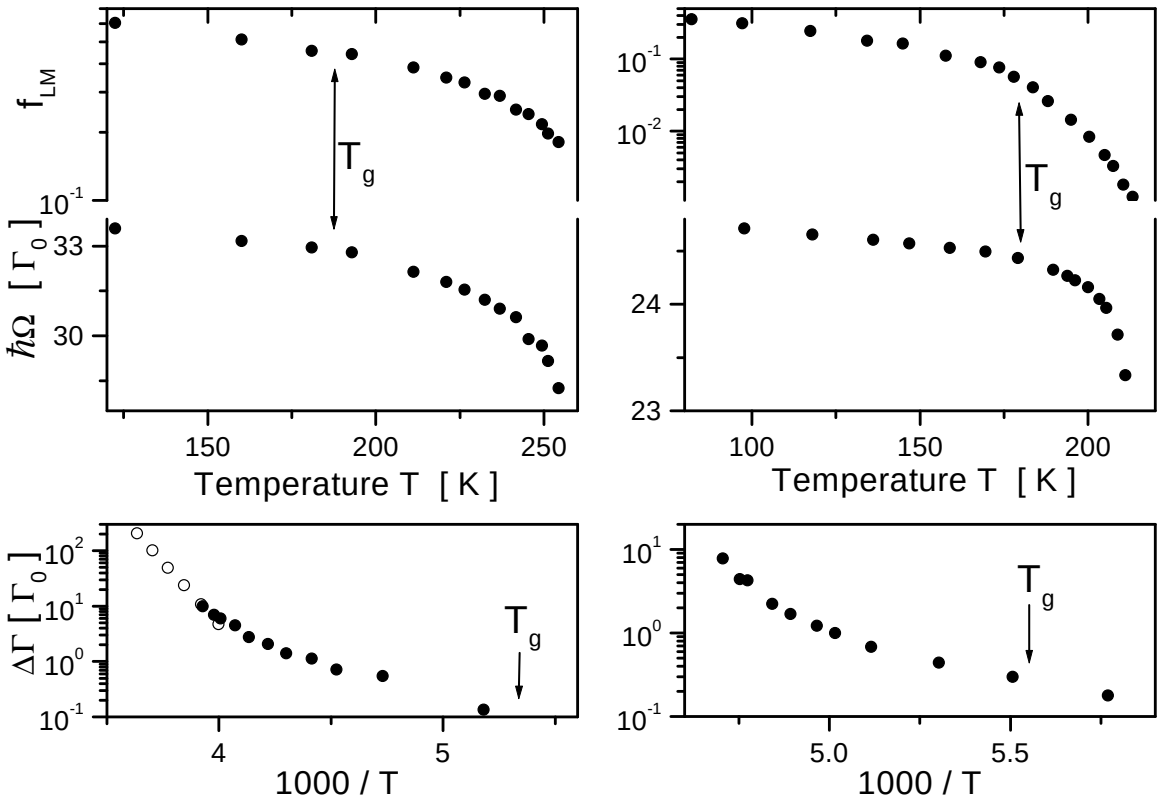

Figure 6.1: Study of the LGT by MS: Fe^{2+} in glycerol (left side) studied in [AM72](•) and in [NFP91](○); ferrocene in dibutyl phthalate [RZF76] (right side). The Lamb-Mössbauer factor f_{LM} (top) and the quadrupole splitting $\hbar\Omega$ (middle) are shown as functions of temperature, and the line broadening $\Delta\Gamma$ (bottom) is shown as a function of inverse temperature. The data for $\Delta\Gamma$ and $\hbar\Omega$ were scaled by $\Gamma_0 = 0.097$ mm/s. f_{LM} for Fe^{2+} in glycerol is obtained by scaling data from [AM72] to the known value of f_{LM} at 130 K [Chu03].

phthalate [RZF76] and o-terphenyl [VF80]. Also, MS was applied to study dynamics of iron-containing polymers [GHL+98] and biomolecules [CHK+96].

Three pronounced features of MS data can identify the LGT: an anharmonic decrease of the Lamb-Mössbauer factor f_{LM}, a broadening $\Delta\Gamma$ of the lines, and a noticeable decrease of the quadrupole splitting $\hbar\Omega$. The temperature dependences of these three parameters are shown in Fig. 6.1 for Fe^{2+} in glycerol [AM72, NFP91] and for ferrocene in dibutyl phthalate [RZF76].

The Lamb-Mössbauer factor describes the fast dynamics on the time scale up to a few ns (in the energy scale down to 200-1000 neV). In solids it is usually defined by lattice vibrations which occur with characteristic times in the fs-ps time region . In harmonic approximation and at temperatures above the Debye temperature the Lamb-Mössbauer

factor can be approximated by

$$f_{LM} \simeq \exp(-aT) \tag{6.1}$$

where the coefficient a is defined by the lattice vibrations. This approximation is also valid for the glassy state of the glass former as seen in the figure. However, around and above T_g a futher decrease of the Lamb-Mössbauer factor occurs which means a strong deviation of $\ln f_{LM}$ from the linear temperature dependence. Whereas such a behavior was always observed in the studies of LGT by MS, a fundamental explanation has been given only by the MCT. This theory predicts the existence of a relaxational process on the picosecond time scale, the fast β relaxation, which leads to the anharmonic decrease of f_{LM}.

Another parameter which was studied in MS is the line broadening $\Delta\Gamma$. It appears due to relaxation on the ns time scale and is proportional to the relaxation rate λ_{NFS}. The data sets which are presented in Fig. 6.1 show two common features: $\log \Delta\Gamma$ is inverse proportional to T at low temperatures (Arrhenius relation) and deviates from this dependence at high temperatures. Abras and Mullen [AM72] explain the turn of the temperature dependence of $\Delta\Gamma$ by assuming that diffusion consists of two distinct processes which additively contribute to the line broadening. The main contribution at low temperatures is a thermally activated diffusion process which is described by an Arrhenius temperature dependence. With an increase of temperature the second contribution becomes important which is due to liquid-like diffusion and is proportional to viscosity. However, both processes were assumed to be due to spatial relaxation. The contribution of spin dynamics to the line broadening was ignored. The influence of spin relaxation has been studied by Ruby et al [RZF76], who tried to separate spin and spatial relaxation contributions to the line broadening. However, this was impossible in the frame of MS. For this reason, it was either assumed [LRK77] or vaguely concluded [RZF76] that only diffusion (spatial relaxation) gives rise to the line broadening $\Delta\Gamma$.

In several works [GHL$^+$98, NFP91, CHK$^+$96] it was obtained that the line shape of the Mössbauer spectra can not be described by a simple exponential diffusion law, but requires a distribution of exponential relaxators. Kohlrausch-like relaxation functions were used and characteristic stretching parameters were obtained.

The last parameter which we consider here is the value of the hyperfine field experienced by the nuclear spin. For the presented studies there is the quadrupole interaction between the nucleus and its surroundings inside a molecule. The temperature dependence of the quadrupole splitting $\hbar\Omega$ is shown in Fig. 6.1 (middle). Whereas in the glassy state a slight gradual decrease of $\hbar\Omega$ is observed, a rapid falloff of the quadrupole splitting occurs during the glass-to-liquid transtion, in the temperature range where also the two other parameters exhibit a deviation from the low temperature behaviour. This supports

the idea that the falloff in $\hbar\Omega$ is connected with the LGT and has a dynamical origin, as was pointed out in [AM72, RZF76]. However, a clear explanation of this phenomenon had not been given.

The discussion given above leads us to several open questions:

- How strong is the contribution of the spin relaxation to the line broadening? Can one neglect this contribution?
- What is the origin of the change of the temperature dependence of the line broadening?
- How one can explain the falloff of the quadrupole splitting in the region of the LGT?

Nuclear resonant scattering of SR allows us to answer these questions. The combination of NFS and SRPAC applied in parallel to investigate dynamics of a glass-forming liquid extends the studied temperature range and allows one to separate spin and spatial dynamics. The last feature leads to a separation of rotational and translational motions in case of suitable probe molecules.

6.2 The sample

As a model substance we have chosen the molecular glass former dibutyl phthalate (DBP) doped by 5% (mol) of ferrocene (FC) enriched by ^{57}Fe. This system, (DBP-FC) has been studied by MS [RZF76] (see Fig. 6.1) and by NFS [MFW$^+$97, SFA$^+$02].

Dibutyl phthalate (DBP) is a molecular glass former of medium fragility ($D = 11$) with a glass transition temperature $T_g = 179$ K [BNAP93] and a melting temperature $T_m = 238$ K [BGCF02]. The characteristic volume per molecule is $V_{DBP} = 441$ Å^3 as obtained from density. The structural formula is $C_6H_4[COO(CH_2)_3CH_3]_2$. A schematic representation of the molecular structure is shown in Fig. 6.2 (left side).

Ferrocene (FC) or biscyclopentadienyl iron, $Fe(C_5H_5)_2$, is a sandwich compound in which the iron atom is located between two five-membered aromatic hydrocarbon rings. The characteristic volume is 196 Å^3 as obtained from density. A schematic representation of the molecular structure is shown in Fig. 6.2 (right side). X-ray analysis of crystals of FC [DOR56] gives that the Fe-C distance is 2.0 Å and the C-C distances around the ring are 1.4 Å. One can estimate that the Fe-ring distance is 1.6 Å. As investigated by EXAFS [KF01] dissolving FC in DBP does not change the Fe-C distance.

The electric field gradient is formed at the iron nucleus by π-bonding ligands and directed perpendicular to the planes of the rings. The EFG produces a relatively large quadrupole splitting, which for ferrocene powder is equal to ~ 2.38 mm/s ($24.5\Gamma_0$) at 80 K [GH68].

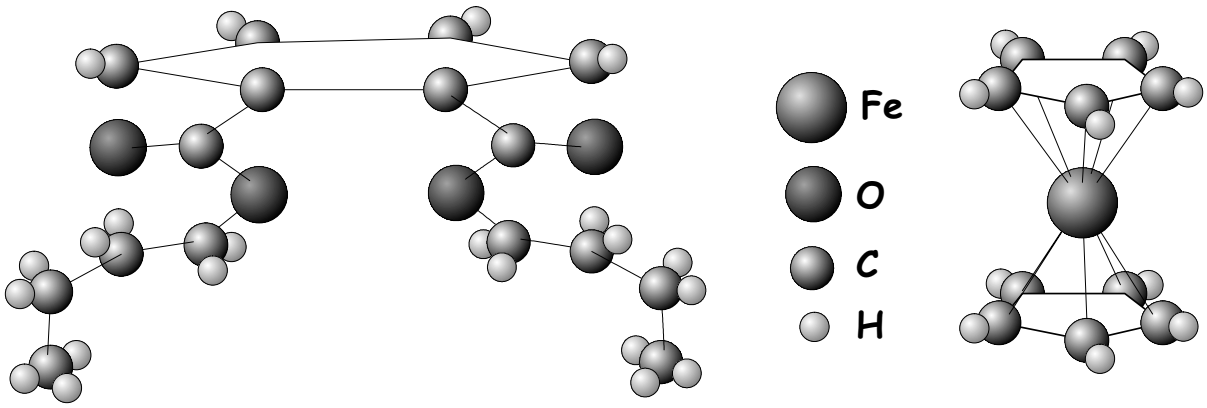

Figure 6.2: Schematic representation of a molecule of dibutyl phthalate (left side) and ferrocene (right side).

Usually the spatial motions of an atom are separated into three contributions: the intermolecular vibrations, the molecular rotation and the translational, center-of-mass molecular motion. The first contribution occurs with a characteristic time much faster than the typical relaxation time. The advantage of the FC molecule is that the iron atom is in the center of mass. Therefore, its position does not change when the molecule rotates. The spatial dynamics of the iron atom unambiguously corresponds to the translational, center-of-mass molecular dynamics. At the same time, the direction of the nuclear spin on the iron site is defined by the structure of the FC molecule. The rotation of this molecule around axes different than ring-Fe-ring axis is seen via the nuclear spin dynamics. Thus, the spatial dynamics of the iron atom in the FC molecule corresponds to translational molecular dynamics and the spin dynamics of the iron atom corresponds to molecular rotation.

Ferrocene enriched to 95% in ^{57}Fe was prepared as follows. In a first step, $FeCl_3$ was obtained in 81% yield by the reaction of an enriched iron sheet with a Cl_2 gas stream in a quartz tube. After dissolving in diethyl ether, a solution containing a stochiometric excess of freshly prepared cyclopentadienyl lithium (LiC_5H_5) in tetrahydrofuran was added under a dry nitrogen atmosphere. Working up the product after stirring overnight and subsequent sublimation gave an overall yield of 71% pure $^{57}Fe(C_5H_5)_2$, which was dissolved in dibutyl phthalate with purity 98% obtained from Sigma to give a 5% (mol) solution. Such a concentration corresponds to 1 FC molecule per 19 molecules of DBP. The obtained solution was inserted into a copper holder with size $10 \times 4 \times 2$ mm^3 sealed with Kapton windows. The temperature measurements were performed using a closed-cycle cryostat having a stability better than ± 0.5 K. Temperatures below 160 K were achieved by fast cooling to reach the glassy state. All measurements were done during heating sequences.

The caloric glass transition temperature of DBP-FC $T_g = 178 \pm 1$ was determined by

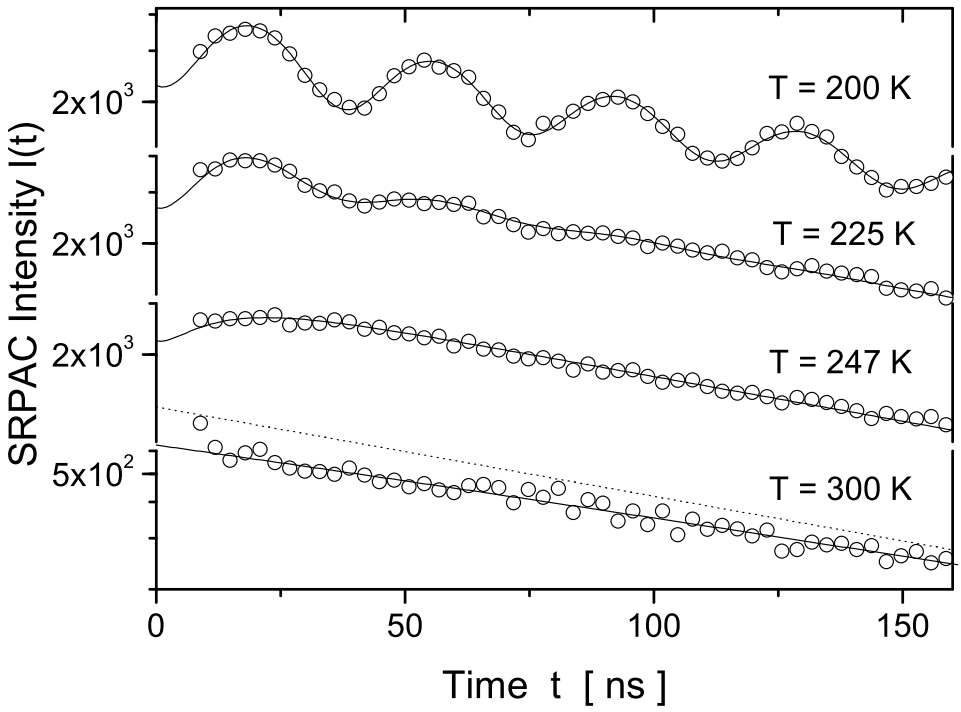

Figure 6.3: Time evolution of the SRPAC intensity measured in the 16 bunch mode. The solid line is the fit by the SCM. The dashed line denotes the natural exponential decay with lifetime of 141.1 ns.

differential scanning calorimetry (with a heating rate of 10 K/min) in [MFW+97]. The value of T_g coincides with the one for pure DBP.

6.3 Experiment by SRPAC

The measurements have been carried out at the European Synchrotron Radiation Facility, Nuclear Resonance beamline ID18.

The first measurements have been performed in the 16 bunch mode (time window $\sim$ 171 ns). The temperature range was 180-250 K, and a reference measurement was performed at 300 K. The setup of the experiment is presented in Section 5.1. The energy bandwidth of the high resolution monochromator was 150 meV covering the entire range of elastic and inelastic nuclear excitations. The detector (area 5x5 mm^2) was placed in 90^o scattering geometry, at 30 mm below the sample. The countrate was 1-2 Hz. Typical time spectra are shown in Fig. 6.3. At 200 K the time evolution is characterized by a natural decay modulated by a pronounced quantum beat (QB) which corresponds to the

quadrupole splitting of ferrocene. The beat exhibits only a weak damping, indicating slow relaxation. At 247 K the QB is largely overdamped due to the rotation of the FC molecules. At 300 K the slow approach of the natural decay (dashed line) is characteristic of fast relaxation. In brief those spectra give an overview on SRPAC influenced by relaxation.

In order to make a systematic study of relaxation the experimental setup was modified in three important points. In order to increase the countrate, a larger detector (area 10x10 mm^2) was placed in 90^o scattering geometry at 10 mm below the sample, yielding a gain in the countrate by a factor of ∼36. A slight decrease of the contrast due to angular average had to be tolerated. In order to reduce the load of the prompt radiation on the detector, the bandwidth of the incident beam was reduced to 6 meV. In order to increase the sensitivity, the experiment was performed in the single bunch mode (time window ∼2.8 μs), allowing for a large observation window. This permits to push both limits of the dynamic range: the lower limit of slow relaxation, where a very weak damping of the quantum beat modulation has to be observed, and the upper limit of fast relaxation, where a very slow approach of the decay to the natural decay has to be followed. Both effects are better seen over a large time window. Using this setup measurements have been performed in the temperature range from 160 K (20 K below T_g) where DBP-FC is in the glassy state, up to 330 K (90 K above melting temperature) where DBP-FC is in the normal liquid state. The entire range from glass to normal liquid state was covered by the measurements. Additionally, a reference measurement was performed at 100 K.

The obtained SRPAC intensities are shown in Fig. 6.4 for several temperatures. The time evolutions are different at low and high temperatures corresponding to the static case and to the slow and the fast relaxation regimes. The anisotropy $A_{22}G_{22}(t)$, which was extracted from the intensity according to eq. (5.1) is shown in Fig. 6.5 for the temperature range $160 - 231$ K and in Fig. 6.6 for the temperature range $240 - 330$ K.

Below 200 K the time evolution of the anisotropy is described by a QB slightly damped in time. The baseline of the beat is shifted up from zero due to the constant contribution of the hard core (compare eq. 4.20). Additionally, at early times SRPAC is overshadowed by the contribution of NFS-Rayleigh scattering (see section 5.2.2). This contribution decays faster than the natural decay. In the anisotropy it is seen as a downward deviation of the baseline at early times. The probability of NFS-Rayleigh scattering is proportional to f_{LM}^2. Therefore, this contribution becomes smaller with increasing temperature and vanishes above 195 K. Below this temperature the data sets were fitted only in the time windows above the times marked by arrows in Fig. 6.5.

At 200-235 K the anisotropy is described by a sum of the QB term and the hard core term both damped in time, so that the anisotropy approaches zero at large times. The envelope of the QB corresponds to the rotational correlation function, which is seen here

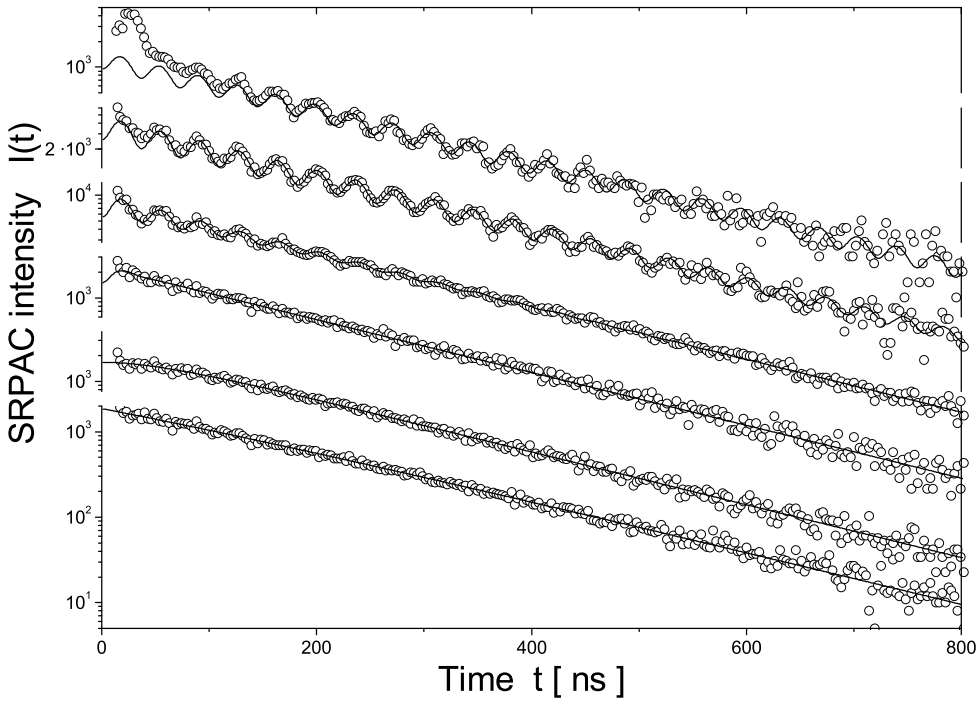

Figure 6.4: Time evolution of the SRPAC intensity for temperatures (from top to bottom): 100, 180, 211, 231, 263 and 296 K. The solid line is the fit by the SCM.

directly in time. The ratio between the decays of the QB and of the hard core is defined by the model of rotation, i.e. by the characteristic jump angle. At 231 K the anisotropy becomes overdamped, so that no QB is seen anymore. A fast decay from the initial value to zero describes the anisotropy here.

The time evolution of the anisotropy in the fast relaxation regime ($T > 235\ K$) is characterized by an exponential decay from the initial value, which is A_{22}, to zero at infinite time. This decay is fast for $T = 242$ K and becomes slower with increasing temperature. The decay rate here is proportional to the mean relaxation time. Therefore, only the integral of the correlation function influences the anisotropy in this regime.

In order to extract information about dynamics from SRPAC data one has to find the value of the anisotropy coefficient A_{22}. Due to the fixed experimental setup and therefore fixed geometry of the experiment, this coefficient has to be the same for all temperatures. It is not reasonable to fit it as a free parameter for each data set. The theoretical calculation of A_{22} as a function of distance d between the detector and the sample, which was done in Section 5.2.1, gives $A_{22} = 0.38 \pm 0.015$ for $d = 10 \pm 1$ mm

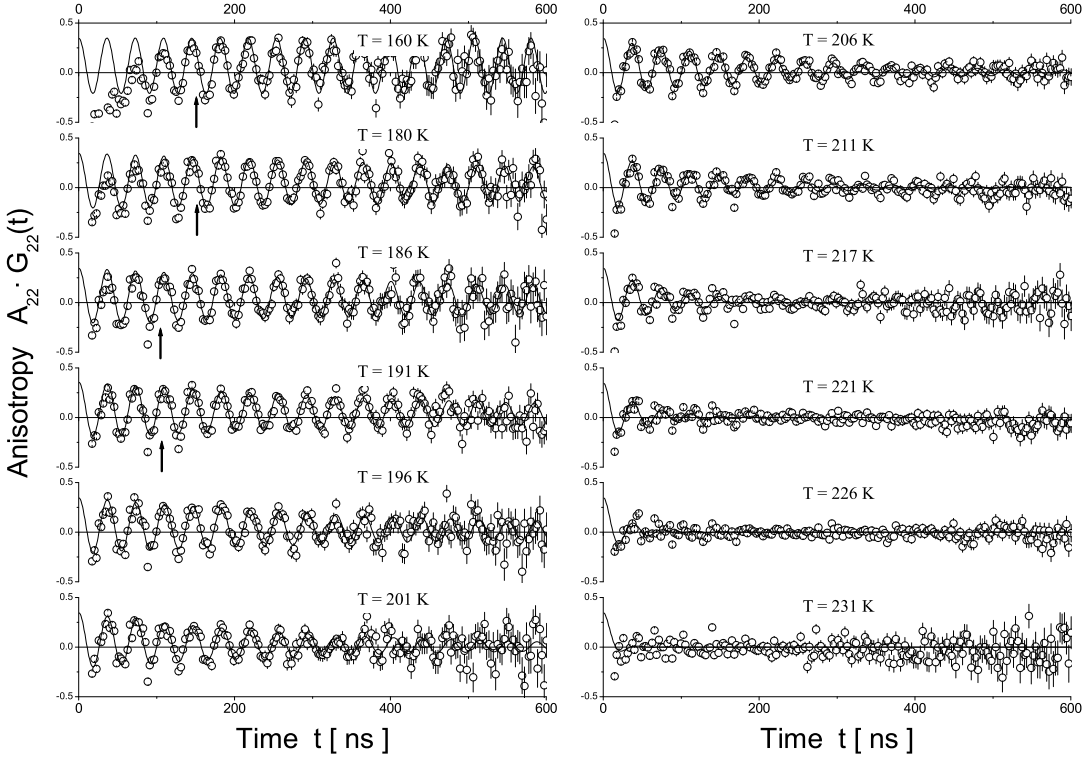

Figure 6.5: Time evolution of the anisotropy for various temperatures in slow relaxation regime. The solid line denotes the fit according to SCM. The arrows show beginning of the fitted time window.

and a 10×10 mm^2 detector. In order to check this value we fit the anisotropy in the fast relaxation regime. This choice of the temperature range is explained as follows. In the slow relaxation regime the time evolution of the anisotropy follows the time evolution of the rotational correlation function, which is unknown in general. Therefore, the value of the initial anisotropy A_{22} depends on the choice of this function. Also, the additional contribution produced by NFS-Rayleigh scattering complicates the extraction of A_{22} from the data. On the other hand, in the fast relaxation regime the anisotropy is well described by the exponential decay independent of the correlation function. The obtained values of A_{22} are shown in Fig. 6.7. One can see that the experimental results coincide with theoretical calculations within the limits of error. This allows us to fix $A_{22} = 0.38$ for all measurements.

In order to fit the SRPAC intensity $I(t)$ in the slow relaxation regime we used numerical calculations of the perturbation factor according to Appendix D. This model assumes an exponential shape of the correlation function and includes three independent parameters: the quadrupole splitting $\hbar\Omega$ which describes the frequency of the quantum beat, the

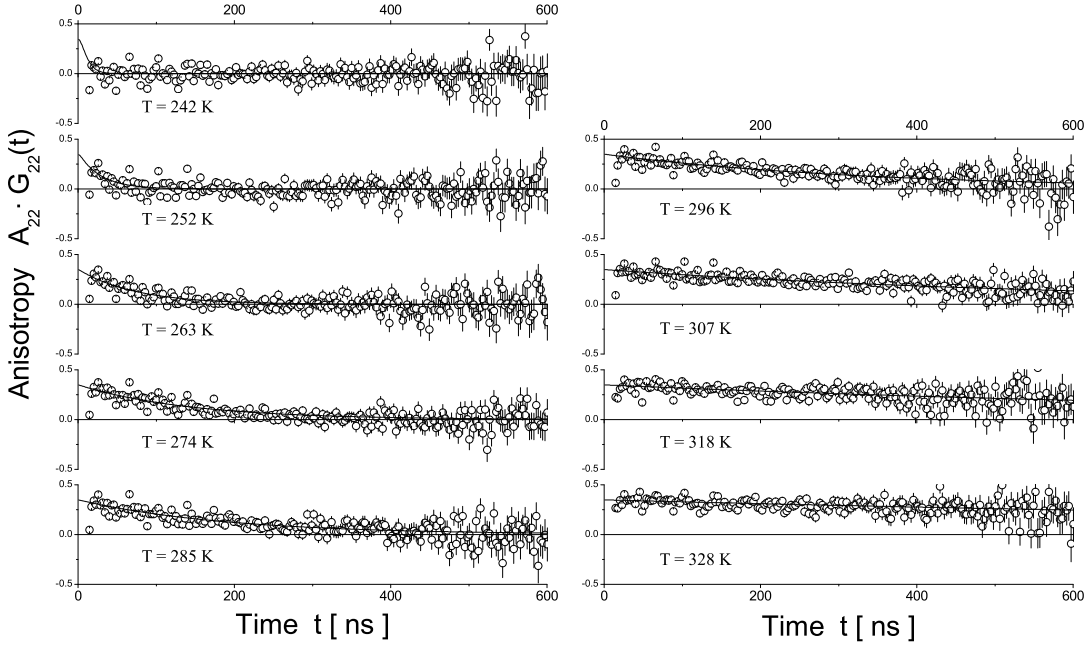

Figure 6.6: Time evolution of the anisotropy for various temperatures in the fast relaxation regime. The solid line denotes the fit by SCM.

relaxation rate λ_2 which describes the characteristic decay rate, and the parameter q which enters into the ratio of decay rates of the QB and of the hard core and which describes the model of rotation.

An attempt to use all three parameters as independent parameters of the fit procedure was not successful. Whereas the decay rate of the quantum beat can be obtained from the fit with reasonable error, the decay rate of the hard core practically can not be obtained with this statistics of the data. In order to overcome this problem we have to introduce the model of rotation a priory. We assume that molecular rotation occurs according to the strong collision model (SCM). There is a good reason to take this model. Consider the dependence of the relaxation rate λ_2 for different values of q on the decay rate p_o of the QB, which can be unambiguously obtained from the fit. According to Fig. 4.6 the possible values of q are restricted to the range $0.4 < q < 3.33$. This restriction leads to (see eq. (4.25))

$$0.54 < p_o/\lambda_2 < 0.7 \tag{6.2}$$

or

$$0.86\frac{p_o}{0.6} < \lambda_2 < 1.11\frac{p_o}{0.6} \tag{6.3}$$

As result we obtain that the relaxation rate λ_2 is situated in the $\pm 15\%$ region around

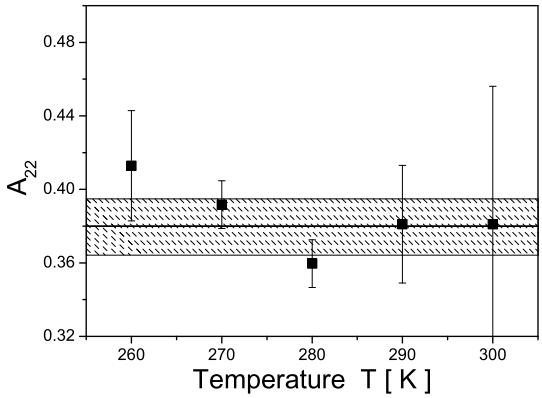

Figure 6.7: The anisotropy coefficient A_{22} obtained from the fit of the SRPAC data. The hatched area denotes the theoretical value $A_{22} = 0.38 \pm 0.015$.

the unambiguously obtained value of $p_o/0.6$ which is the decay rate in the SCM ($q = 1$) according to eq. (4.20). Thus, one can write $\lambda_2 \simeq \lambda_2^{SCM}(1 \pm 0.15)$ which means that independent of the model of rotation, the relaxation rate λ_2 is situated in the $\pm 15\%$ region around λ_2^{SCM}. This conclusion allow us to work in the frame of the SCM. For this model an analytical expression for the perturbation factor exists which is described in Appendix E.

The approach presented above is valid only in the slow relaxation regime and applies only to the relaxation rate λ_2. In order to estimate in general the sensitivity of the relaxation rate and the quadrupole splitting on the choice of the model we have treated the experimental data in addition using the RDM ($q = 20/6$). This treatment uses the numerical procedure of Appendix D. The comparison of the relaxation rate and the quadrupole splitting for the two different models of rotation gives their possible range.

Fig. 6.8 shows the temperature dependence of the quadrupole splitting $\hbar\Omega$ obtained in the SCM and the RDM and of the effective quadrupole splitting $\hbar\Omega_e$ which is the true frequency of the QB. The quadrupole splitting is almost constant up to 180 K and decreases above. The three sets of data are identical up to 200 K and diverge above. It is shown in the theoretical part of this work (see eq. (4.21)) that the effective quadrupole splitting $\hbar\Omega_e$ decreases due to relaxation as $\Delta\Omega_e \propto -\lambda_2^2$. This fact explains the deviation of $\hbar\Omega_e$ from $\hbar\Omega$ obtained in the SCM. On the other hand, the increase of $\hbar\Omega$ obtained in the RDM is artificial, probably, due to the wrong choice of the model of rotation. The coincidence of all data sets below 200 K means that the influence of the relaxation is vanishing below this temperature and that the decrease of $\hbar\Omega$ in the region 180-200 K can not be explained by the influence of slow rotational relaxation. We attribute this decrease to fast librations of the ferrocene molecules in a restricted angular range which

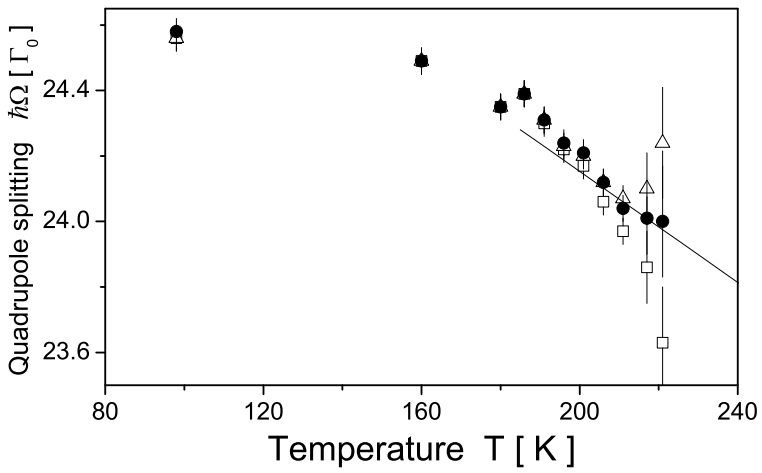

Figure 6.8: Temperature dependence of the effective quadrupole splitting $\hbar\Omega_e$ (□) and of the quadrupole splitting $\hbar\Omega$ obtained by SRPAC using the SCM (•) and the RDM (△). The solid line denotes the extrapolation to high temperatures.

lead to a pre-average of the quadrupole splitting as it is shown in Section 4.4.4. The corresponding interpretation of the data will be given later.

The quadrupole splitting can be obtained as an independent parameter only up to 221 K. At higher temperatures λ_2 and Ω form one parameter, Ω^2/λ_2 and can not be fitted independently. Therefore, in order to extract λ_2 one has to introduce some information about Ω at the temperature range above 225 K. We assume a linear extrapolation of $\hbar\Omega$ as

$$\hbar\Omega = 25.85 \cdot (1 - T/3047) \tag{6.4}$$

This dependence is shown in Fig. 6.8 by a straight line. It reproduces the temperature dependence of $\hbar\Omega$ obtained in the SCM up to 221 K. The real dependence of the quadrupole splitting on temperature can deviate from this linear approximation. However, the possible uncertainties are not significant, because the variation of Ω with temperature is much smaller than that of λ_2.

Fig. 6.9a shows the temperature dependence of the relaxation rate λ_2 obtained using the SCM and the RDM. The relaxation rate increases from $\sim 0.2/\tau_0$, at 160 K up to $5.6 \cdot 10^3/\tau_0$ at 328 K. As a whole, reliable data are obtained within a frequency range covering 5 decades. The data sets obtained using the two different models show similar behaviour. At low temperatures they are shifted by a scaling factor of $1.1 - 1.2$ which is in agreement with our estimation (see eq. (6.3) and discussion). Above 230 K data sets nicely coincide corresponding to the independence of the relaxation rate on the model of rotation in the fast relaxation regime.

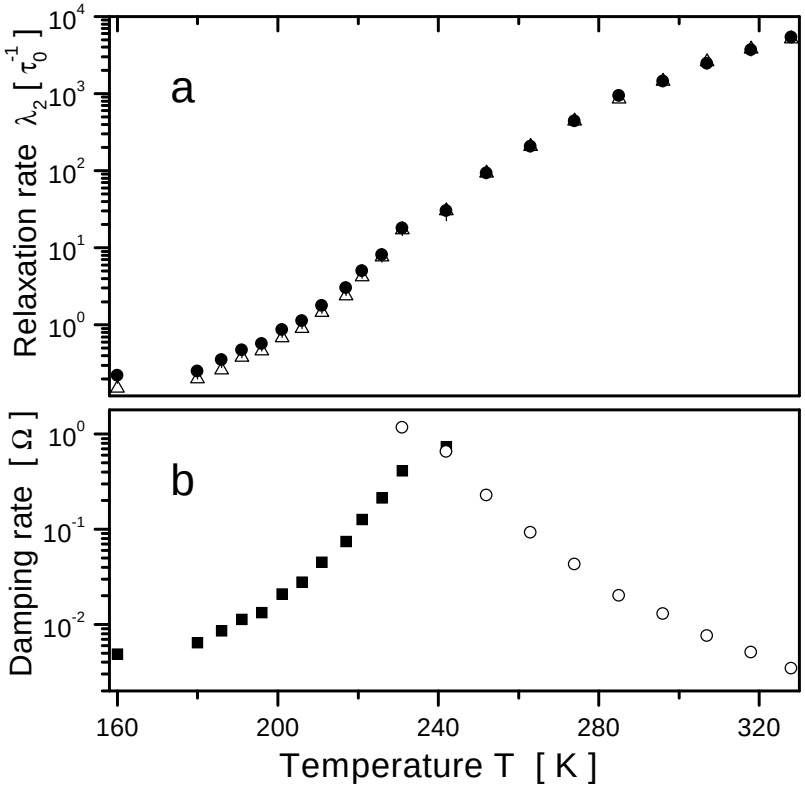

Figure 6.9: a) Temperature dependence of the relaxation rate λ_2 obtained by SRPAC using the SCM (•) and the RDM (△). b) Temperature dependence of the damping rate of the anisotropy in slow relaxation regime (■) and in the fast relaxation regime (○).

In order to see a separation of the whole temperature range into slow and fast relaxation regimes we plot the characteristic damping rate of the anisotropy in Fig. 6.9b. For low temperatures only the damping of the QB contribution in the anisotropy is shown which has the rate $0.6\lambda_2$ (see eq. (4.20)). At high temperatures the damping rate of the anisotropy is given by $0.8\Omega^2/\lambda_2$ (see eq. (4.26)). One can see that the damping increases with temperature in the low temperature region and decreases in the high temperature region. The two curves cross at 230-240 K and in this region $\Omega \sim \lambda_2$. The data sets at 231 and 242 K have maximum damping rate where the anisotropy falls to zero right from early times on.

Fig. 6.9b allows us to define the frequency range which can be investigated by SRPAC. The minimum damping rate is defined by the experimental time window and by the life time τ_0 of the excited state. In the present measurements the minimum damping rate is $\sim 0.1/\tau_0$. This corresponds to $\lambda_2 \sim 0.16/\tau_0$ as a minimum relaxation rate and to $\lambda_2 \sim 8\Omega^2\tau_0$ as a maximum relaxation rate. The separation into the slow and fast relaxation regimes occurs around a maximum damping rate, where $\lambda_2 \sim \Omega$. In the present measurements the temperature range around 230-240 K corresponds to the intermediate

relaxation regime. Accordingly, the slow relaxation regime extends up to ∼230 K and the fast relaxation regime starts at ∼240 K.

6.4 Experiment by NFS

The measurements at low temperatures have been performed in the hybrid bunch mode (time window ∼ 500 ns). In these measurements NFS alone has been observed in the temperature range 25-190 K. The used sample had a thickness of 12 mm. Typical time spectra are shown in Fig. 6.10.

A second set of NFS measurements has been performed in parallel with SRPAC measurements in the temperature range 160-211 K. While SRPAC measurements were continued above 211 K, the countrate of the NFS signal becomes too low due to a vanishing Lamb-Mössbauer factor. The measured time spectra are shown in Fig. 6.11. The detection of the delayed signal starts at ∼20 ns in both sets of measurements due to overload of the detector.

The time evolution of the NFS intensity is defined by a combination of the exponential decay, the QB due to the quadrupole splitting of the excited state and the dynamical beat (DB) due to multiple scattering.

The QB is the most pronounced feature of the data sets. The period of the QB is ∼36 ns and is almost constant with temperature. At low temperatures the QB is strongly perturbed by the interaction with the DB.

The DB is shown by arrows in Fig. 6.10. It follows the Bessel-like dependence in time. Periods of the DB increase with time. A characteristic frequency is proportional to the effective thickness ξ of the sample and to the Lamb-Mössbauer factor f_{LM}. At low temperature the value of ξf_{LM} is so large that six DB minima are seen in the experimental time window up to 500 ns. The Lamb-Mössbauer factor decreases with temperature, which leads to a stretching of the DB in time. Whereas the first minimum is around 20 ns at 50 K, it shifts to 45 ns at 124 K, to 70 ns at 150 K and to 180 ns at 177 K. One can see that the stretching increases drastically between 150 and 180 K, which is connected with a strong decrease of f_{LM} in this temperature region. The second set of measurements uses a sample with 1.2 times smaller thickness which is seen in the comparison of the time spectra at 177 K (Fig. 6.10) and at 180 K (Fig. 6.11). While f_{LM} is almost the same, the position of the first DB minimum is different. This is due to the different value of ξ. Above 190 K no DB minima are observed in the experimental spectra. At these elevated temperatures the effect of the DB reduces to an additional exponential decay with a decay rate proportional to ξf_{LM} according to the quasi-kinematical approximation (see eq. (3.11)).

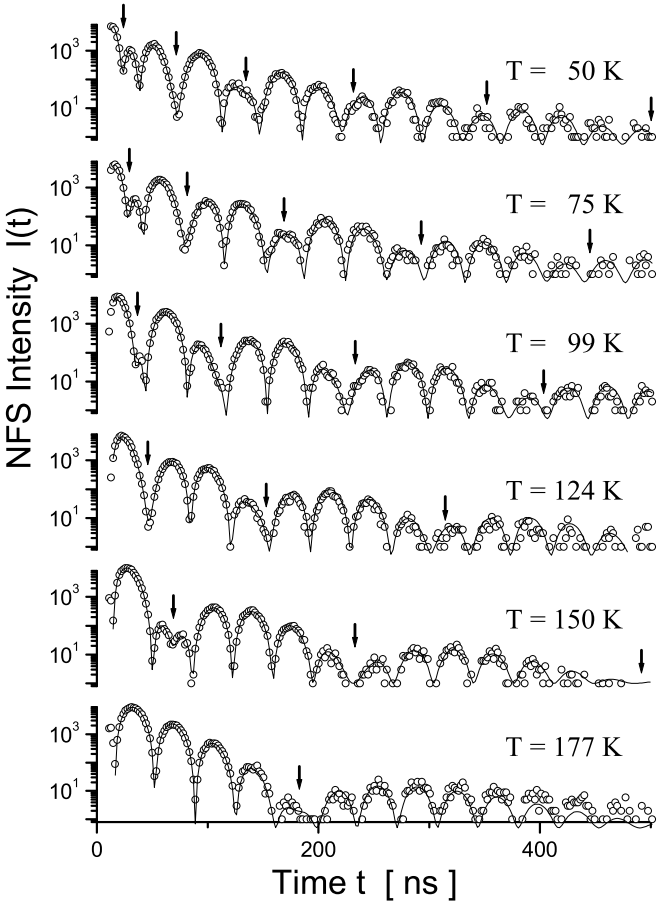

Figure 6.10: Time evolution of the NFS intensity at low temperatures measured in the hybrid bunch mode. The solid line denotes the fit by the model (see text). The arrows show minima of the DB.

The relaxation appears as an additional damping of the intensity. Above 200 K a non-exponential (stretched) decay of the NFS intensity becomes visible.

The treatment of the data measured below and above 160 K has been performed in a different way. Below 160 K relaxation is absent and the numerical calculation of the NFS intensity was used according to eqs. (3.3)-(3.5). The free parameters were the incoming intensity I_0, the effective thickness parameter ξf_{LM} and the quadrupole splitting $\hbar\Omega$. In order to obtain ξ and f_{LM} separately, the obtained values of ξf_{LM} were compared with f_{LM} obtained by nuclear inelastic scattering (NIS) at 25, 50, 100, 150 K on the same sample [Chu03]. As a result, the effective thickness $\xi = 87$ is obtained for the first sample. Comparison of ξf_{LM} of the first and second samples gives $\xi = 73$ for the second sample which corresponds to the ratio of thicknesses of the samples.

The treatment of the data measured above 160 K meets several problems which have to be solved. The first problem is the shape of the relaxation function which has to be

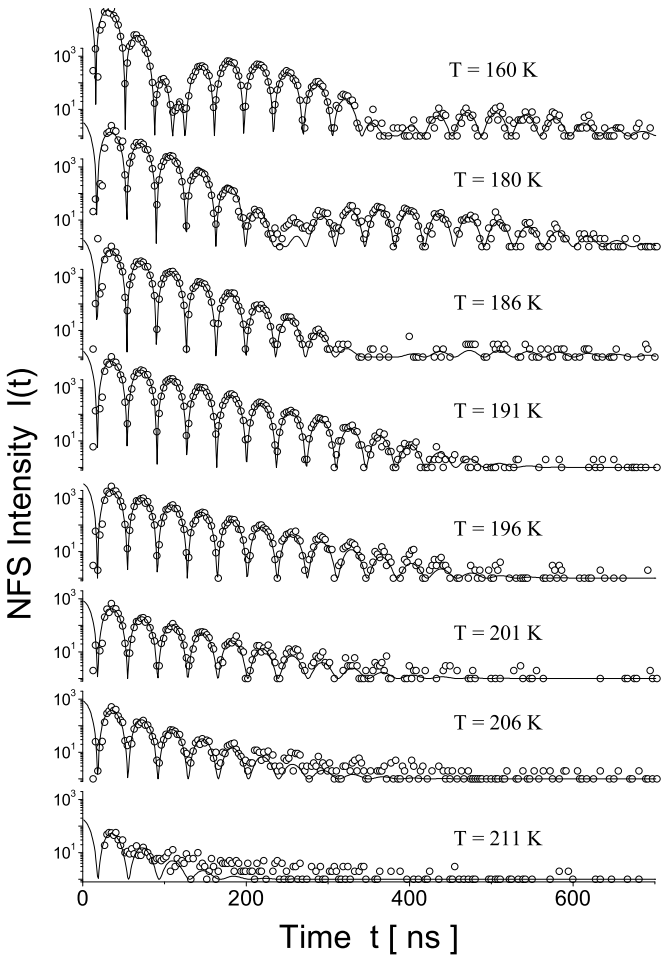

Figure 6.11: Time evolution of the NFS intensity at high temperatures measured in the single bunch mode in parallel with SRPAC. The solid line denotes the fit by the model (see text).

introduced into the theoretical model. The experimental data manifest a non-exponential character of the relaxation above 200 K. On the other hand, the developed general theoretical model for SRPAC and NFS implies an exponential relaxation. In this section we limit the treatment of the data to an exponential shape of the relaxation function taking into account that the same exponential relaxation was used to treat the SRPAC data and that both NFS and SRPAC were measured in the same time region. This fact allows us to compare results obtained in both methods. Later, we consider the treatment of the data by a Kohlrausch relaxation function.

The theoretical expression describing the NFS intensity in the presence of spatial and spin dynamics is developed in Section 4.5. The free parameters here were the incoming intensity I_0, the effective thickness parameter ξf_{LM}, the relaxation rate λ_{NFS} and the effective quadrupole splitting $\hbar\Omega_e$. The relaxation rate λ_{NFS} is the sum of $\lambda_2/2$ which de-

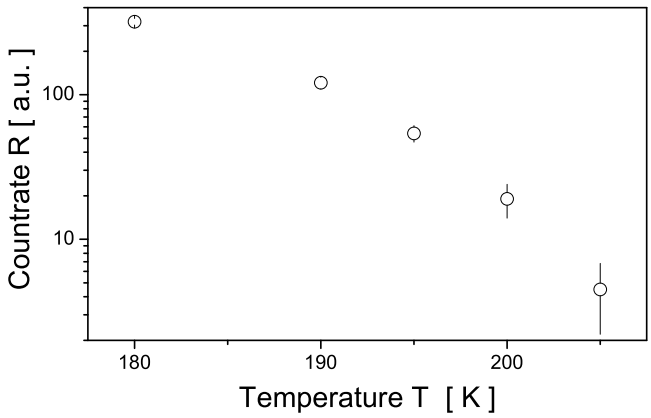

Figure 6.12: Temperature dependence of the countrate R.

scribes molecular rotation and λ_t which describes translational, center-of-mass molecular motion. The effective quadrupole splitting $\hbar\Omega_e$ differs from the quadrupole splitting due to the influence of rotational relaxation.

Above 190 K the DB minima are not seen in the experimental time window and an evaluation of ξf_{LM} from the DB structure is not possible. Moreover, the damping of the intensity is formed by a sum of $\xi f_{LM}/2\tau_0$ and $2\lambda_{NFS}$. In order to separate these two terms we use another way to obtain ξf_{LM}. The scattered intensity at time zero is proportional to $\xi^2 f_{LM}^2$ according to eq. (3.10). Then, by scaling of the obtained data sets to the same incoming intensity one can obtain the dependence of ξf_{LM} on temperature from the value of the intensity at time zero. However, the experimental setup does not provide a long time stability of the incoming radiation level. Therefore, it is very difficult to estimate the intensity incident on the sample during the entire time of measurement (from 0.5 up to 8 hours).

In order to overcome this problem we measure the integrated NFS intensity during a short period of time. We call this value countrate R. During this time the incoming beam is stable and its intensity is measured. The countrate is scaled to the unit of time and to the unit of the incoming intensity. The countrate obtained this way is shown in Fig. 6.12 for temperatures above 180 K. Theoretically, the integral of the NFS intensity in the quasi-kinematical approximation gives

$$R \propto \int I(t)\mathrm{d}t \propto \frac{\xi^2 f_{LM}^2}{1 + \xi f_{LM}/2 + 2\lambda_{NFS}\tau_0} \tag{6.5}$$

The denominator here is the decay rate of the intensity and can be extracted from the time spectra. The proportionality coefficient can be found at 180 K where ξf_{LM} is extracted straightforwardly from the DB structure and where the quasi-kinematical approximation

starts to be valid. The value of ξf_{LM} obtained from the countrate, was used to separate the decay rate of the intensity and to get the relaxation rate λ_{NFS}.

The eq. (6.5) which describes the integral of the NFS intensity does not take into account the QB and the cutoff of the experimental time window below 20 ns. However, both factors lead only to a small correction of the expression. A more important correction can appear if we consider relaxation governed by the Kohlrausch function. Then, the fast decay at early times that is a part of the structural relaxation process is not visible in the experimental time window. The approximation of the visible part of relaxation by exponential function leads to an artificial decrease of the Lamb-Mössbauer factor.

6.5 Results and discussion

In the present measurements nuclear resonant scattering has been applied to study the dynamics of the glass former DBP-FC. In particular, NFS has been studied up to 211 K and SRPAC - up to 330 K. Below 221 K four parameters are obtained: the relaxation rate λ_2 from SRPAC, the relaxation rate λ_{NFS} from NFS, the quadrupole splitting $\hbar\Omega$ from SRPAC and NFS and the Lamb-Mössbauer factor f_{LM} from NFS. The relaxation rates are connected with the slow dynamics which is seen directly in the experimental time window. $\hbar\Omega$ and f_{LM} are influenced by the fast dynamics restricted in space, like vibrations, rattling and librations.

In the 220-330 K temperature range only one parameter is obtained - the relaxation rate λ_2. It gives information about the mean relaxation time for the rotational correlation function $C_2(t)$ (see Section 4.4.2).

6.5.1 Fast dynamics

Fig. 6.13 shows the temperature dependence of the Lamb-Mössbauer factor. The data can be described phenomenologically by a multiplication of two functions: the first one decreases exponentially with temperature; the second function equals unity up to 100 K and decreases faster than exponential above. Such factorization has a physical explanation. The Lamb-Mössbauer factor corresponds to the decay of the self-correlation function due to the fast molecular motions localized in space. Two processes define these motions in glasses: vibration and fast localized relaxation. We assume the independence of these processes. Therefore, the Lamb-Mössbauer factor can be factorized as

$$f_{LM} = f_h \cdot f_r \tag{6.6}$$

where f_h corresponds to the vibrations and f_r to the relaxation.

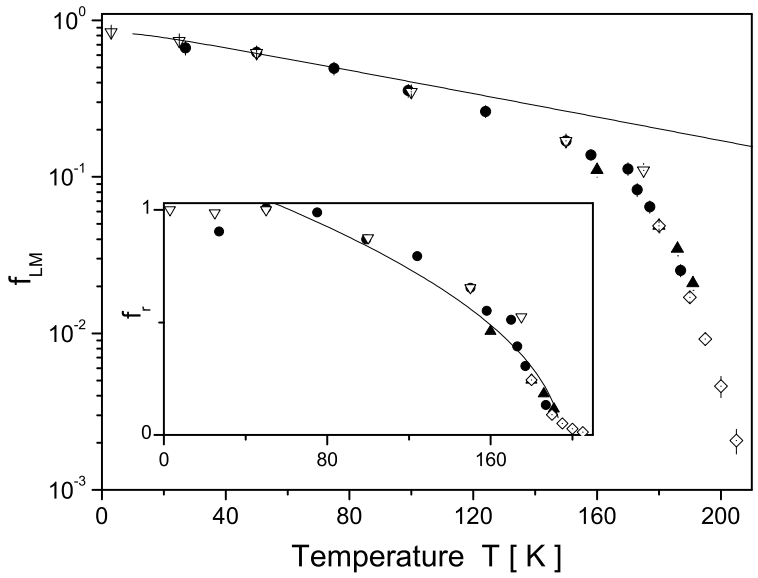

Figure 6.13: Temperature dependence of the Lamb-Mössbauer factor f_{LM} obtained by NFS (•,▲), NIS (▽) and from countrate R (◊). The solid line denotes the vibrational contribution f_h to the Lamb-Mössbauer factor. Inset: temperature dependence of the relaxational contribution f_r to the Lamb-Mössbauer factor obtained by $f_r = f_{LM}/f_h$. The solid line denotes the fit according to the square root dependence of eq. (6.8).

In order to obtain the temperature dependence of f_h we consider the results of NIS on the same sample [Chu03]. This method gives direct access to the density of phonon states. The partial phonon density of states (DOS) $g(E)$ of the iron nuclei in DBP-FC is shown in Fig. 6.14a as measured at 50 K. Above 15 meV, it exhibits three narrow peaks. These are the eigen modes of the ferrocene molecule, which involve displacements of the central iron atom. The vibrational states below 15 meV describe displacements of the rigid FC probe driven by the correlated motions in DBP-FC. The reduced DOS $g(E)/E^2$ of the correlated motions is shown in Fig. 6.14b for various temperatures. This function remains the same up to 100 K. Above, it enhances at low energy with increasing temperature. We identify these additional modes with fast localized relaxation via a rattling of the molecules in cages of their neighbors, which becomes more pronounced with temperature. The identity of the reduced DOS below 100 K allows us to conclude that $g(E)$ here describes the pure vibrational density of states. This function is used to calculate f_h by [SS60]

$$f_h = \exp\left(-E_R \int_0^\infty \frac{g(E)}{E} \cdot \frac{1+\exp(-E/k_BT)}{1-\exp(-E/k_BT)} \mathrm{d}E\right) \tag{6.7}$$

where E_R is the recoil energy and k_B is the Boltzmann constant. The obtained tempera-

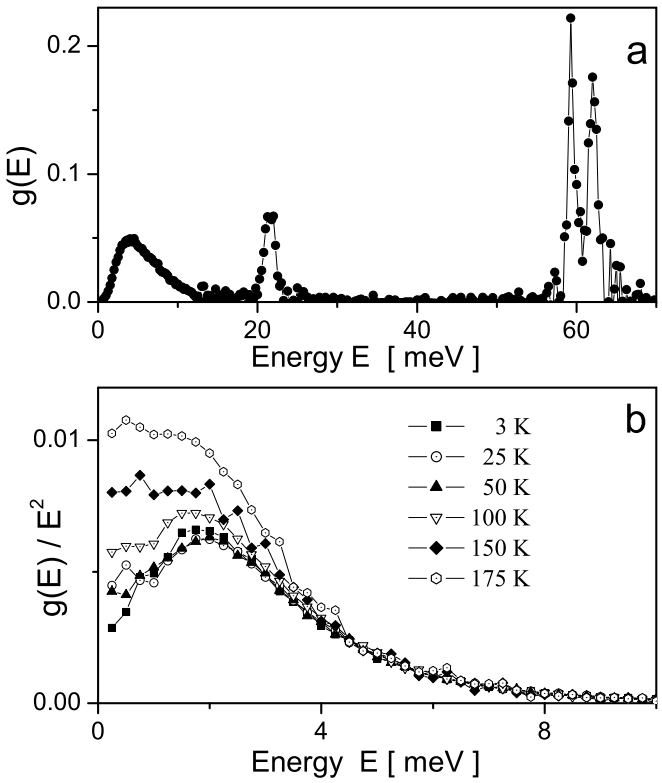

Figure 6.14: a)The partial density of states $g(E)$ of the iron nuclei in DBP-FC at 50 K obtained by NIS [Chu03]. b) The reduced partial density of states $g(E)/E^2$ in DBP-FC for various temperatures obtained by NIS [Chu03].

ture dependence of f_h is shown by the solid line in Fig. 6.13. ln f_h exhibits an almost linear dependence on temperature above ∼50 K which can be easily derived from eq. (6.7). Using f_{LM} and f_h we obtain the relaxational factor f_r which is shown in the inset of Fig. 6.13 as a function of temperature. In the MCT the fast localized relaxation, i.e. fast β relaxation is introduced and f_r is expressed by a square-root dependence (see eq. (3.8))

$$f_r = f_0 + h_r\sqrt{1 - T/T_c} \tag{6.8}$$

where T_c is the crossover temperature where the mechanism of relaxation is changing from thermal activation to liquid-like motion. The fit of the data by this function gives $f_0 = 0$, $h_r = 1.3$ and $T_c = 195$ K. The fit is shown by the solid line in the inset of Fig. 6.13. The curve qualitatively describes the decrease of f_r in the temperature range from 80 up to 195 K. According to MCT f_r above T_c is described by a weak dependence on temperature (see eq. (2.8)). In principle, a similar behaviour of the data is seen above 195 K. This similarity, however, should be considered with care due to the difficulties in evaluation discussed at the end of the Section 6.4. Also, one should remember that the approximation (6.8) is valid only near T_c.

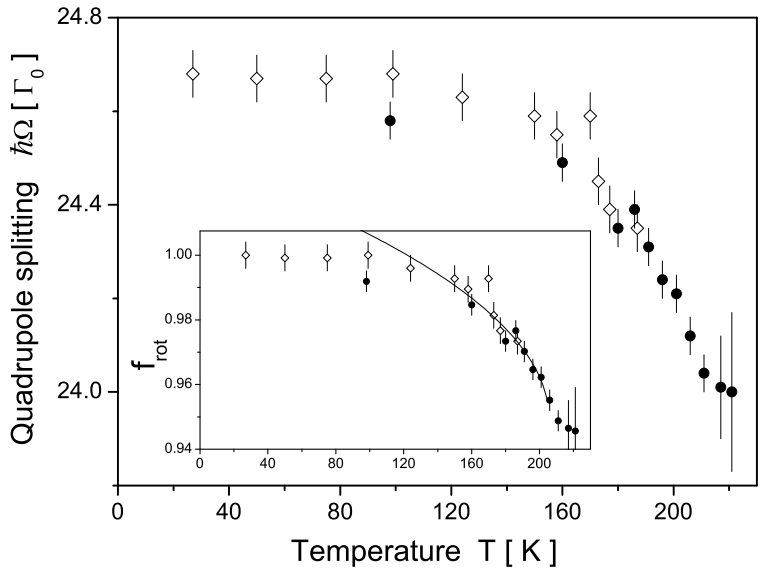

Figure 6.15: Temperature dependence of the quadrupole splitting $\hbar\Omega$ obtained by NFS ($\Diamond$) and SRPAC using the SCM ($\bullet$). Inset: temperature dependence of the rotational factor f_{rot} obtained by $f_{rot} = (\hbar\Omega/24.68\Gamma_0)^2$. The solid line denotes the fit according to the square root dependence of eq. (6.8).

Another interpretation of the Lamb-Mössbauer factor can be given using the mean-square displacement $< r^2 >$ of the iron atom

$$f_{LM} = \exp(-k^2 < r^2 >). \tag{6.9}$$

where the wave vector $k = 7.3$ Å^{-1} corresponds to the resonant energy. Similar to eq. (6.6) the mean square displacement can be presented as a sum of vibrational $< r^2 >_h$ and relaxational $< r^2 >_r$ contributions. The vibrational contribution can be evaluated as before. The temperature dependence of the relaxational contribution is shown in Fig. 6.16 in comparison with the mean square angular displacement.

The temperature evolution of the quadrupole splitting is shown in Fig. 6.15 as obtained by SRPAC and NFS. The quadrupole splitting remains constant up to ∼100 K and decreases above. It was already shown that the slow relaxational process cannot explain this decrease. We rather attribute it to fast librations of the FC molecules in a restricted angular range which leads to an averaging of the electric field gradient and of the quadrupole splitting over angle. It was shown in Section 4.4.4 that these fast librations can be described by the rotational factor f_{rot} which is similar to the Lamb-Mössbauer factor but in the angular space. According to eq. (4.32)

$$\frac{\Omega}{\Omega_0} = \sqrt{f_{rot}} \simeq 1 - \frac{3}{4} < \alpha^2 > \tag{6.10}$$

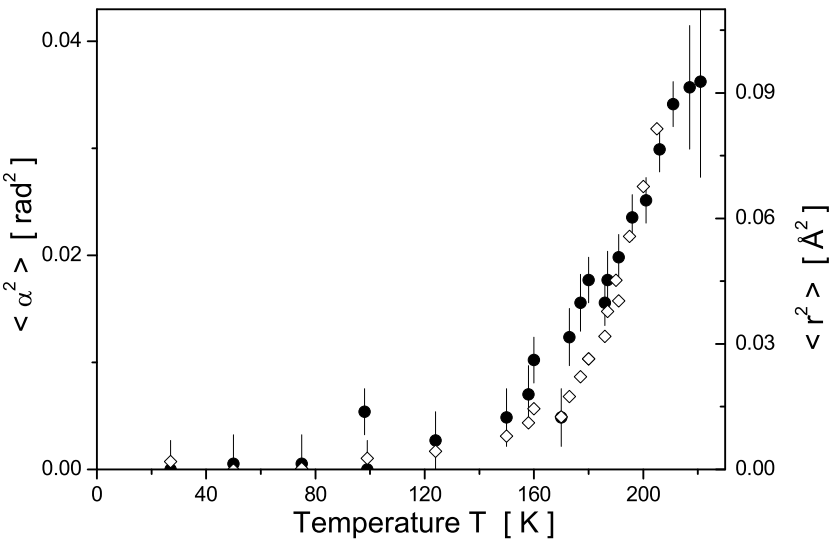

Figure 6.16: Temperature dependences of the relaxational part $< r^2 >_r$ of the mean square displacement ($\Diamond$) obtained from the Lamb-Mössbauer factor and of the mean square angular displacement $< \alpha^2 >$ ($\bullet$) obtained from the quadrupole splitting. The left scale corresponds to $< \alpha^2 >$ and the right scale corresponds to the $< r^2 >_r$. The scaling factor is $< r^2 >_r = < \alpha^2 > \cdot 2.56 \mathring{A}^2$.

where $< \alpha^2 >$ is the mean square angular deviation and the second equality is obtained in the approximation of small $< \alpha^2 >$. The quadrupole splitting exhibits a constant dependence below 100 K, which leads to $f_{rot} = 1$ at those temperatures. Using $\hbar\Omega_0 = 24.68$ we obtain the rotational factor which is shown in the inset of Fig. 6.15. This factor can also be fitted by the square-root dependence of eq. (6.8). The solid line in the inset of the figure shows this fit. The obtained parameters are $f_0 = 0.95$, $h_r = 0.08$ and $T_c = 206$ K. Again, the data show a weak temperature dependence above 206 K which corresponds to the MCT prediction. However, the uncertainty of the data increases drastically above this temperature. Also, $\hbar\Omega$ here strongly depends on the chosen model of rotation as was shown in Fig. 6.8.

The treatment of both f_{LM} and f_{rot} leads to the conclusion that the crossover temperature T_c is in the region of 195-206 K. Also we can use the result of the treatment of NFS measurements on DBP-FC using the Kohlrausch relaxation function [SFA$^+$02]. Here, $T_c = 202$ K has been obtained from the temperature dependence of f_{LM}. Combining the results we obtain $T_c = 201 \pm 6$ K as a good estimate for the crossover temperature.

The rattling contribution to the mean square displacement $< r^2 >_r$ can be compared with the mean square angular displacement $< \alpha^2 >$ which is obtained from f_{rot} according to eq. 6.10. The temperature dependences of both parameters are shown in Fig. 6.16. The

two data sets show similar temperature dependences and mainly coincide when scaled appropriately. This striking similarity proves that the fast angular librations of the FC molecule and the fast spatial displacement of its center of mass are tightly coupled and caused by the same process, the fast β relaxation. The scaling coefficient is

$$\sqrt{< r^2 >_r} = 1.6\mathring{A} \cdot \sqrt{< \alpha^2 >}. \tag{6.11}$$

This coefficient corresponds to the distance between the iron atom and the hydrocarbon rings. A similar coincidence of the temperature behaviour has been observed in [SFS92], where the mean square displacement and the mean square angular displacement of a side group of a molecule have been investigated. The authors identified the coincidence with rotation of the side group around a stiff molecular center of mass. Respectively, the scaling coefficient is the distance between the center of mass and the side group. However, this simple explanation does not work in our case, since we observe formally independent processes of center-of-mass translation and rotation around center of mass.

6.5.2 Slow dynamics

Fig. 6.17 shows the rotational relaxation rate λ_2 obtained from SRPAC as a function of inverse temperature $1000/T$. One can see that λ_2 exhibits a different behaviour above and below 210 K. Whereas a linear Arrhenius dependence is observed below this temperature, a non-Arrhenius viscosity-like behaviour is seen above. According to the MCT we explain this change of behaviour by different mechanisms of relaxation. The thermally activated hopping process drives relaxations at low temperatures and the coupling between modes of motion in the ensemble of molecules defines the structural relaxation at high temperatures. Therefore, we fitted the data by different functions at low and high temperatures. The Arrhenius law was used to fit λ_2 below 210 K

$$\lambda_2 = \lambda_2^0 \exp(\Delta E / k_B T) \tag{6.12}$$

The fit is shown by the solid line in Fig. 6.17 and gives $\lambda_2^0 = 2.4 \cdot 10^{11}$ Hz and $\Delta E = 2130K \cdot k_B = 17.7$ kJ·mol^{-1}.

The data at high temperatures were fitted by the MCT power law (see eq. (2.3))

$$\lambda_2 = \lambda_2^0 \, (T/T_c - 1)^{\gamma} \tag{6.13}$$

The temperature dependence of the relaxation rate here is defined by two parameters: γ and the crossover temperature T_c. They hardly can be fitted together. The fits with T_c chosen as 180, 201 and 220 K are shown in the inset of Fig. 6.17. The obtained γ equals 5.4, 4.4 and 3.3, respectively. One can see that the best fit corresponds to $T_c = 180$ K. However, this result is physically incorrect since T_c must be well above T_g. From the two

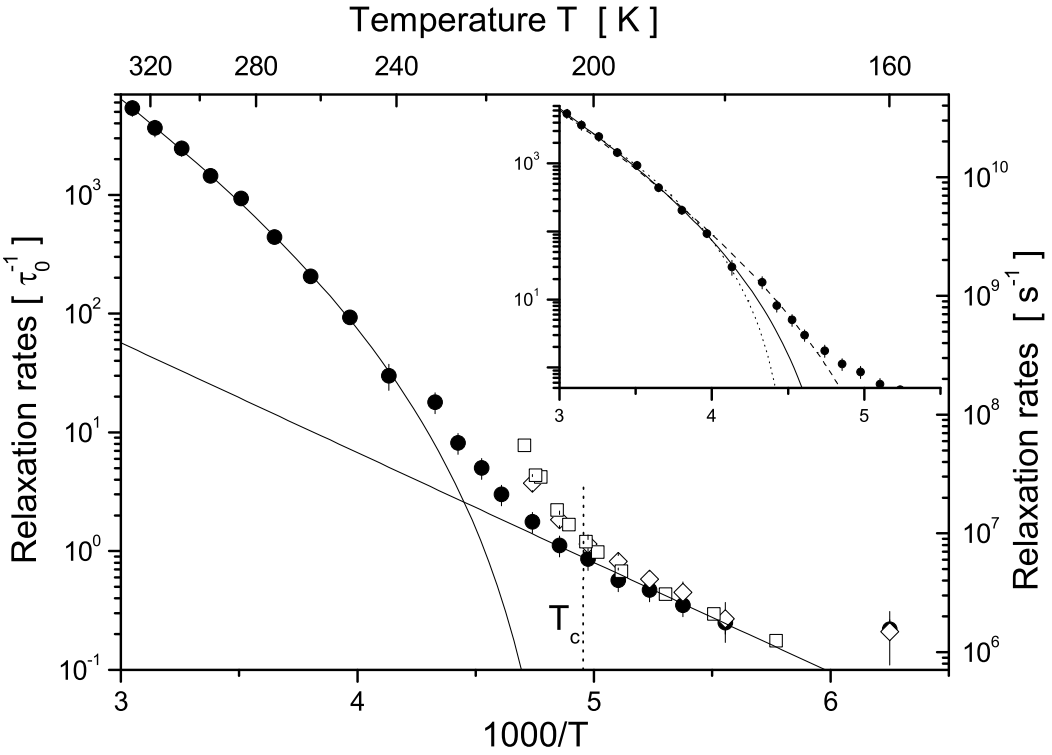

Figure 6.17: Inverse temperature dependence of the rotational relaxation rate λ_2 obtained from SRPAC (•), the relaxational rate $2\lambda_{NFS}$ obtained from NFS (◊) and the line broadening $\Delta\Gamma$ obtained from MS (□) in [RZF76] . The solid lines denote fits by an Arrhenius law above $1000/T = 4.8$ and by a MCT power law below $1000/T = 4.4$. $T_c = 201$ K was chosen for the MCT power law. Inset: fit of λ_2 by the MCT power law with T_c chosen as 180 K (dashed line), 201 K (solid line) and 220 K (dotted line).

other curves we hardly can choose the better one. In order to do so we use the information about T_c which was acquired by the investigation of fast dynamics where $T_c = 201$ K has been obtained. The solid line in Fig. 6.17 shows the MCT power law fit with $T_c = 201$ K, $\gamma = 4.4$ and $\lambda_2^0 = 3.1 \cdot 10^{11}$ Hz.

The fit by those two models allows us to divide the entire temperature region into three parts: above ∼240 K, where supercooled liquid dynamics is observed, below 210 K where thermally activated dynamics is observed and between 210 and ∼240 K where the transition from one to the other dynamics occurs.

Additionally to λ_2, we plot in Fig. 6.17 the relaxation rate $2\lambda_{NFS}$ obtained from NFS and the line broadening $\Delta\Gamma$ obtained by MS on a similar sample in [RZF76]. The last value is equivalent to $2\lambda_{NFS}$ so that the two data sets have to coincide which is indeed realized

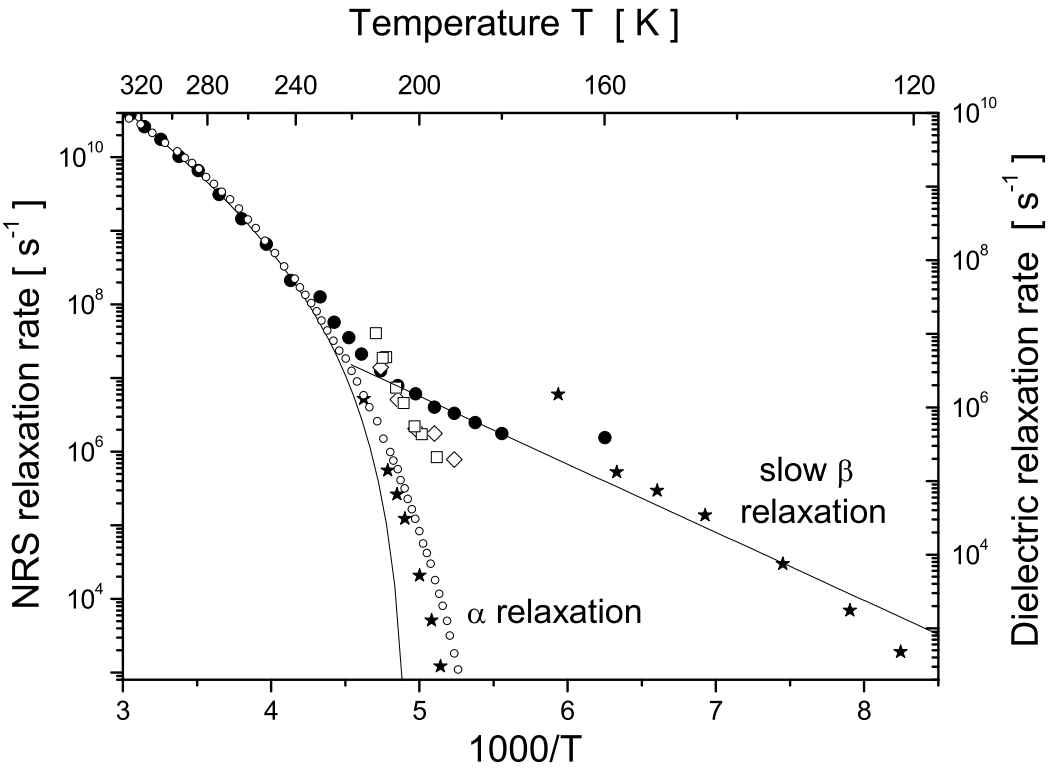

Figure 6.18: Comparison of the rotational, λ_2 (•) and translational, $2\lambda_t$ (◊, □) relaxation rates of the probe FC molecule obtained by nuclear resonant scattering (left scale) to the dielectric spectroscopy data for pure DBP (right scale) from [DWN$^+$90] (○) and [DT87] (★). The solid lines denote the Arrhenius and MCT power dependences; they are the same as in Fig. 6.17.

in our case. It is shown in Section 4.5 that the relaxation rate observed in NFS consists of a rotational and a translational contribution as given by $2\lambda_{NFS} = \lambda_2 + 2\lambda_t$ where λ_2 is the same rotational relaxation rate as in SRPAC and λ_t is the decay rate of the exponential van Hove self correlation function with scattering vector $k = 7.3$ Å^{-1}. Physically it means that de-coherence of NFS in time is produced additively by two contributions: stochastic molecular rotation which is seen via spin dynamics and translational relaxation which is seen due to the collective character of NFS.

From a comparison of the NFS, MS and SRPAC data we see that below ∼195 K all data sets coincide which corresponds to $\lambda_2 \simeq 2\lambda_{NFS}$ and, therefore, $\lambda_t \simeq 0$. More precisely, λ_t is less than the limit of sensitivity of nuclear resonance scattering i.e., $\lambda_t < 7 \cdot 10^5$ s^{-1}. Thus, below 195 K, the position of the FC molecule is frozen on the molecular length scale and ns time scale. Above 195 K, however, $2\lambda_{NFS}$ begins to deviate from λ_2 because

translational dynamics becomes comparable or even faster than rotational dynamics.

The pure translational relaxation rate $2\lambda_t$ can be derived and compared with λ_2. It is done in Fig. 6.18. In the same figure we compare our results for the dynamics of the probe FC molecules in DBP to data on pure DBP available from dielectric spectroscopy (DS) [DT87, DWN$^+$90]. The DS data were scaled by factor of 4 to match our data at room temperature. At high temperatures the relaxation measured by DS consists of a single branch, which coincides with our data for the rotational relaxation of the FC probe molecule. At low temperatures the DS data split into two branches: structural α relaxation and slow β relaxation. The slow β relaxation is followed by our data on rotational molecular dynamics whereas structural α relaxation decreases in parallel with our data on translational dynamics. The coincidence of the slow β relaxation branch of DS and our data allows us to conclude that the rotation of the probe is driven by the same process of slow β relaxation. On the other hand, the FC molecules remain in the same space position on a sub-molecular length scale and on the time scale of slow β relaxation. We can conclude that, probably, the same absence of the translational motion is realized for DBP molecules as well. As a result, slow β relaxation can be identified with a certain mode of non-translational motion which decouples from the structural relaxation below T_c. This mode of motion is molecular rotation in the case of the FC molecules and, probably, for DBP molecules as well. Molecular rotation in the frozen glass structure can explain the origin of slow β relaxation in the rigid molecular glass formers that was discussed in Section 2.5.

We should mention here the result of [FGSF92] where a comparison of rotational dynamics measured by NMR and translational dynamics measured by various tracer techniques has been performed for o-terphenyl. The authors obtained that the rotational relaxation rate increases faster with temperature than the translational one. Whereas at T_c both relaxation rates are comparable, at T_g, the translational relaxation is more than 2 orders of magnitude faster than rotational relaxation. This result looks opposite to that obtained by us. However, whereas we investigate the time scale corresponding to slow β relaxation, in [FGSF92] the time scale of structural α relaxation has been studied. Also, nuclear forward scattering deals with the dynamics on a molecular length scale whereas tracer techniques are sensitive to the translational motions on a macroscale.

In our investigation the rotational dynamics decouples from α relaxation. However, we cannot say that there is no other branch of rotational relaxation which follows the α branch. There are mainly two reasons why this branch is not seen. At first, the SRPAC theory has been developed in the assumption of only one relaxation process. Secondly, nuclear resonant scattering on ^{57}Fe is not sensitive to the relaxation with frequency smaller than $10^5 - 10^6$ Hz.

A crossover temperature $T_c = 220 - 230$ K in DBP has been found in several stud-

ies [BGCF02, Rös90]. This value is significantly larger than our $T_c = 201$ K. However, in [Rös90] T_c has been obtained from the fit of the viscosity by a MCT power equation. As we saw (compare inset of Fig 6.17), without additional independent information this fit is not precise and strongly depends on the chosen temperature region. In [BGCF02], where DBP was studied by the heterodyne detected optical Kerr effect, the fit of the rotational relaxation time has been performed by a MCT power equation. The power parameter γ was fixed there via critical exponent of the fast β relaxation. Whereas qualitatively the obtained curve describes the experimental data, a systematical deviation is seen, which is, probably, due to a incorrect choice of γ and which leads to an artificial increase of T_c. In general, we can conclude that $T_c = 201$ K obtained in our study from the dependence of the Lamb-Mössbauer factor and of the quadrupole splitting on temperature at $T < T_c$ gives a lower limit of the estimation region of T_c while $T_c = 227$ K obtained in [BGCF02] from dependence of the relaxation rate on temperature at $T > T_c$ gives the upper limit of this region.

The above interpretation of the results is restricted by the assumption of an exponential character of relaxation. On the other hand, it is well known that wide frequency distributions describe relaxation processes in glass formers. However, we use the fact that both NFS and SRPAC measurements were done in the same experimental time window. As result, the comparison of the NFS and SRPAC data is hardly sensitive to the choice of the relaxation function. Moreover, in the fast relaxation regime, SRPAC is independent on the relaxation function and gives the mean relaxation rate.

6.6 Stretched exponential relaxation

In the previous section the relaxation which appears in NFS was assumed to be exponential. This allows us to factorize the relaxation into a translational and a rotational contribution and, with the help of SRPAC, to find the rate of each contribution. On the other hand, we can assume that the dynamics which is seen in NFS is described by the generalized self-correlation function which includes both types of motion [GSV00]. This function can be described by a Kohlrausch function (see eq. (3.21)). The two parameters of this function are the relaxation rate λ_t and the stretching parameter β which is the feature of non-exponentiality of this function. In this section we do not take care about the type of motion which is seen in NFS, but will only try to extract information about the parameter β. In order to do so it is helpful to make an additional data treatment.

The QB which is seen in the NFS time evolution occurs with a characteristic time faster than the characteristic times of all other processes. Also, the QB and the relaxation contribution to NFS intensity are independent. Therefore, in order to avoid additional

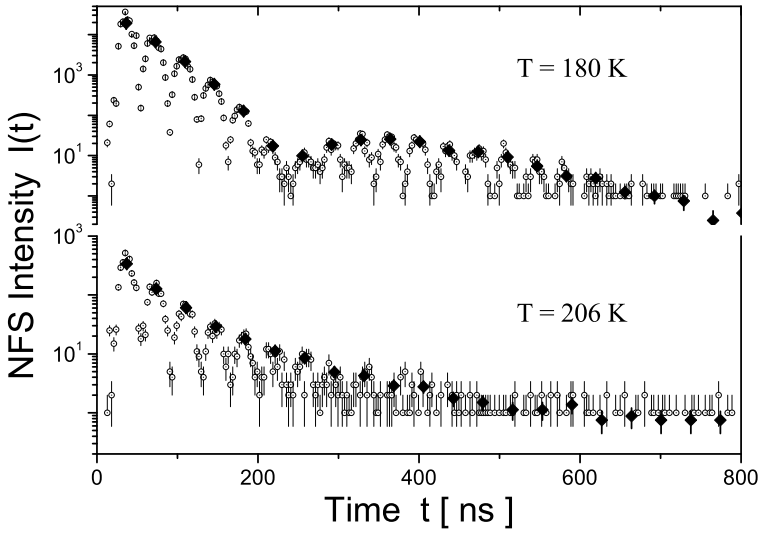

Figure 6.19: Data treatment procedure: original experimental data (⊙), modified data corrected to the average intensity (⧫).

parameters in the fit procedure and to increase the statistics in the long time window the integration of the time spectra over the QB oscillations can be done before fitting. The integration was performed for each beat period and the time abscissa of the integrated data were set to the positions of the maxima of the QB pattern. The resulting set of points can be considered as a response of the ensemble of the nuclei with a single resonance and the theory introduced in Section 3.4.3 can be applied for the treatment of a data.

The correctness of this procedure was checked numerically by the fit of the full and the reduced set of the data measured at 180 K. The comparison of the results shows an agreement within the limit of the experimental error. In Fig. 6.19 the original and the modified data are shown for two temperatures. One can see that for $T = 206$ K the reduced data look more informative in the time region after several τ_0 than the original one.

The left side of Fig. 6.20 shows the time evolution of the reduced NFS intensity for the temperatures 180-206 K. The experimental data were fitted using the numerical calculation of the NFS intensity for a single resonance and a Kohlrausch relaxation function according to Appendix A. The accurate estimation of the stretching parameter β requires the observation of the signal at least over two decades of time [GS92]. The experimental time region is ~ 1.5 decades ($30 \div 800$ ns) and an estimation of β as a free parameter of the fit is difficult. In order to solve this problem, β was chosen as $\beta = 1, 0.8, 0.6, 0.5, 0.4$. For each β the sum of least square residuals χ^2 of the least-squares fit procedure was calculated. χ^2 as a function of β is shown in the right side of Fig 6.20. One can see that

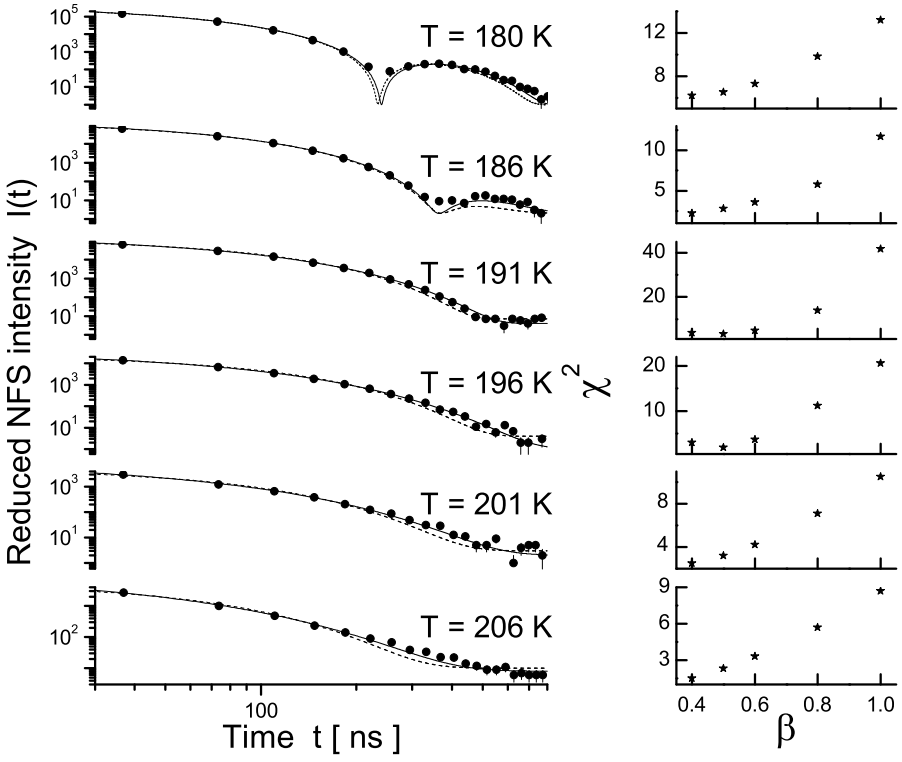

Figure 6.20: Left side: time evolution of the reduced NFS intensity for various temperatures. The lines show the fit with relaxation described by the Kohlrausch function with $\beta = 0.5$ (solid line) and $\beta = 1$ (dashed line). Right side: the sum of least square residuals of the fit χ^2 as a function of parameter β.

χ^2 monotonically decreases with β decreasing from 1 to 0.5. However, the dependence of χ^2 on β becomes less pronounced when β comes to ~ 0.5. This can be explained as follows.

Fig. 3.3 shows the distribution of the Debye (exponential) relaxators corresponding to the Kohlrausch function. The distributions for $\beta = 1, 0.9, 0.7$ extend over ~ 1 decade of frequency (corresponding to one decade of time). Taking the part of the distribution corresponding to one decade, it is possible to restore the full distribution. On the other hand, the distribution for $\beta = 0.3$ can not be restored taking only one decade of frequency range. The one decade part of the distribution near the center is almost constant and hardly gives information about the tails. The value $\beta \sim 0.5$ corresponds to the border value. We can say that the observed experimental data can not be described by $\beta > 0.5$. However, the experimental time window does not allow us to find a precise value of β. Phenomenologically, one can work with the maximal possible β. This value was estimated

as $\beta = 0.47$ in [SFA$^+$02] which roughly corresponds to the presented experimental data.

Chapter 7

Study of LGT dynamics in restricted geometry by NFS

The application of NFS to study dynamics of a glass-forming liquid confined in pores is presented in this chapter. After a brief introduction and a description of the sample the experiment by NFS is described. The obtained results are compared with the results in the bulk case in the last part.

7.1 Dynamics of viscous liquids in restricted geometry

Studying the relaxation dynamics of liquids and glass formers in restricted geometries has attracted much interest recently [FZB00] for mainly two reasons. First, it is obviously important to understand how fluid systems behave on interaction with surfaces, e.g. on a catalyst, in a capillary or in a mesoscopic material, especially with respect to a multitude of applications in chemical and biological sciences. Second, it is believed that confinement may also help to address more fundamental questions about bulk dynamics. For example, the existence of diverging timescales at the glass transition is now widely accepted [Göt99], whereas the question whether there is also an associated characteristic length scale remains an unsolved question up to date. This question can be addressed by introducing the glass former into a geometrically confined environment, in order to test qualitative changes in the glass dynamics when the characteristic length exceeds the size of the confined space. Here, it is mandatory to minimize strength and range of the interaction between the glass and its surrounding matrix, so that purely geometrical constraints dominate the dynamical behavior.

During the last 15 years many different techniques were applied to such systems, for a recent review see [FZB00]. Surprisingly, the obtained results do not give a clear answer at

all. For certain systems the caloric glass transition temperature in the confined system is found to be higher than in the bulk system [SMRF94], whereas in other systems it seems to be lower [JM91].

The experimental investigation of the dynamics of glass formers inserted into a matrix which defines the restricted geometry is often complicated due to a strong background signal from the matrix. The unique advantage of NFS is that this method is a background-free method: only the iron-containing glass former is observed since only the resonant nuclei contribute to the delayed signal. The matrix itself gives a signal at $t = 0$, which is discriminated in the experiment. Another advantage of NFS is that small samples may be used due to the high brilliance of SR.

7.2 The sample

The molecular glass former dibutyl phthalate (DBP) doped by 5% (mol) of ferrocene (FC) enriched by ^{57}Fe was used as a model substance. The study of this glass former in the bulk case was presented in the previous chapter. The preparation of DBP-FC was described in Section 6.2.

The nanoporous samples were prepared from commercially avaliable (Geltech Inc., Orlando, USA) SiO_2 aerogel pellets prepared by a sol-gel process and having pore sizes 25, 50, 75 and 200 Å. In order to optimize the countrate including the influence of photoabsorbtion, pellets having 6 mm diameter and 2 mm thickness were ground down to half-disks of 1.1-1.5 mm thickness.

The loading procedure was performed by T. Asthalter and A. Huwe and is described in [ASF$^+$01, ASG$^+$97]. In order to avoid the chemical coupling between the glass former and the wall, the pore walls were lubricated using hexamethyldisilazane before adding DBP-FC.

7.3 Experiment by NFS

The measurements have been carried out at the ESRF, Nuclear Resonance beamline ID18.

The first measurements have been performed in the 16 bunch mode (time window $\sim$ 171 ns). Pellets with 25, 75 and 200 Å pore sizes were studied in the temperature range 80-200 K. The usual setup for NFS was used. Typical time spectra are shown in Fig. 7.1 for 25 and 200 Å pore sizes. The results of this study have been published in [ASF$^+$01]. The time evolution of the intensity is characterized by an exponential decay modulated by a pronounced QB due to the quadrupole splitting of the iron nucleus in the ferrocene

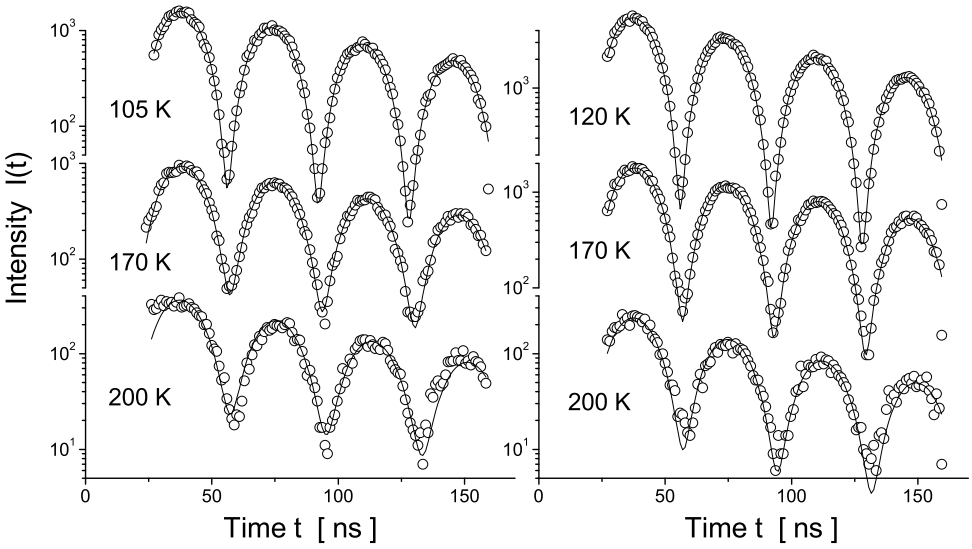

Figure 7.1: Time evolution of the NFS intensity measured in 16 bunch mode for 25 Å (left side) and 200 Å (right side) pore sizes. The solid line shows the fit.

molecule. The decay rate gives information about the rate of relaxation which seems to depend on the pore sizes. The smallest relaxation rate was obtained for the 25 Å pores. However, the relatively short experimental time window and the overlap of the signal from subsequent bunches lead to a uncertainty of the relaxation rates.

In order to increase the sensitivity, the experiment was repeated in the single bunch mode (time window $\sim$2.8 μs), allowing for a large observation window. Samples with pore sizes 25 and 50 Å have been used in this experiment in order to see the largest deviation of the relaxation rate from that in the bulk. In order to get information about the Lamb-Mössbauer factor and about the low-temperature behaviour of the quadrupole splitting the temperature range has been extended to 28-207 K.

The obtained NFS spectra are shown in Fig. 7.2 for several temperatures. For all temperatures except 28 K the time evolution of the intensity is well described by an exponential decay modulated by a QB with a period of about 36 ns. The effect of multiple scattering is limited to a weak acceleration of the natural decay, and the intensity is well described by the quasi-kinematical approximation. The additional decay rate is proportional to ξf_{LM} and decreases with temperature due to the decrease of f_{LM}. The time spectra here differ strongly from those for the bulk (see Fig. 6.10, 6.11) where the DB structure of multiple scattering is observed up to 190 K. The first minimum of the DB structure for the 25 Å and 50 Å samples is at the same time of $\sim$400 ns. On the other hand, the first minimum for the bulk sample at 50 K is at $\sim$20 ns. The position of

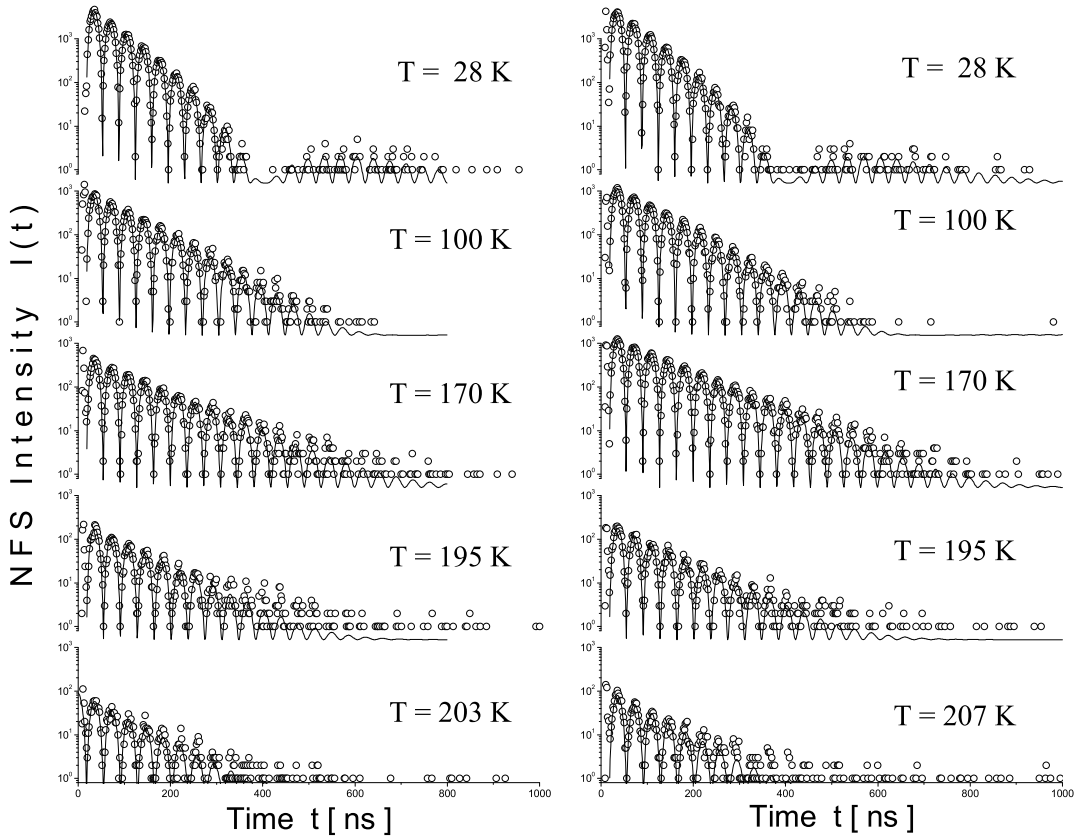

Figure 7.2: Time evolution of the NFS intensity measured in single bunch mode for 25 Å (left side) and 50 Å (right side) pore sizes. The solid line shows the fit.

this minimum is inverse proportional to ξf_{LM}, therefore, ξf_{LM} for the bulk sample is ∼20 times larger than for the nanoporous samples. Assuming roughly the same value of the Lamb-Mössbauer factor, one can estimate that the effective thickness of the bulk sample was ∼20 times larger than for the nanoporous samples.

The relaxation, which appears at temperatures above ∼ 160 K, is seen as an increase of the decay rate. The non-exponential character of relaxation leads to a stretching of the time spectra which is seen at highest temperatures.

The treatment of the data is performed here assuming an exponential relaxation function. In the quasi-kinematical approximation one can define the NFS intensity as

$$I(t) = I_0(\xi f_{LM})^2 \mathrm{e}^{-(1+\zeta)t/\tau_0} \cos^2(\Omega_e t/2\tau_0) \tag{7.1}$$

where the effective quadrupole splitting $\hbar\Omega_e$ and the decay rate ζ is introduced. The decay rate ζ is defined by the combination of the effective thickness parameter and the relaxation rate

$$\zeta = \frac{\xi f_{LM}}{2} + 2\lambda_{NFS}\tau_0. \tag{7.2}$$

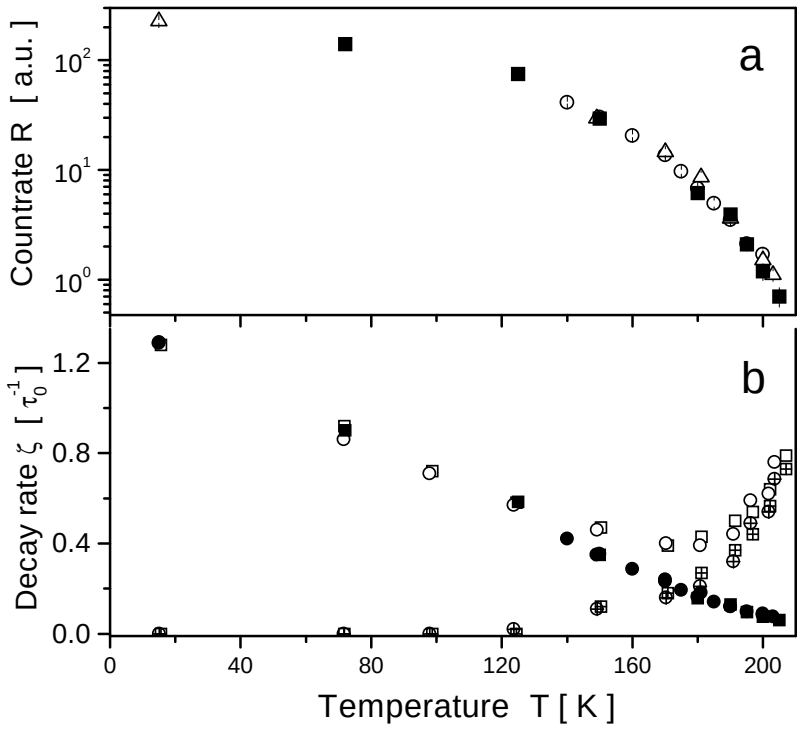

Figure 7.3: a) Temperature dependence of the countrate R for the 25 Å (○,△) and the 50 Å (■) samples. The data were scaled to the same value at 150 K. b) Temperature dependence of the decay rate ζ (○, □), of the effective thickness parameter $\xi f_{LM}/2$ (●, ■) and of the relaxation rate $2\lambda_{NFS}$ (⊕, ⊞) for the 25 Å and the 50 Å samples, respectively.

The data were fitted with 3 independent parameters: I_0, $\hbar\Omega_e$ and ζ. The temperature dependence of ζ for both nanoporous samples is shown in Fig. 7.3b. The data sets for both 25 Å and 50 Å samples almost coincide. ζ decreases with temperature up to 170 K and increases above. Such a behaviour is explained by the opposite temperature dependences of the two contributions in ζ. $\xi f_{LM}/2$ is the major contribution at low temperatures. It decreases with temperature and its contribution at high temperatures becomes negligible. On the other hand, $2\lambda_{NFS}\tau_0$ is zero at low temperatures, but increases with temperature. Its contribution to ζ is dominant at high temperatures.

The separation of these two contributions to ζ requires an additional independent information. In order to obtain it we measured the countrate R. This parameter was introduced in Section 6.4 and is the NFS intensity integrated over the experimental time window observed during a short time of measurement. The temperature dependence of the countrate is shown in Fig 7.3a. The connection between R and the NFS intensity $I(t)$ is given by

$$R = a' \int_{20\ ns}^{\infty} dt \cdot I(t)/I_0 = a\frac{(\xi f_{LM})^2}{1+\zeta} \mathrm{e}^{-0.14\zeta} \tag{7.3}$$

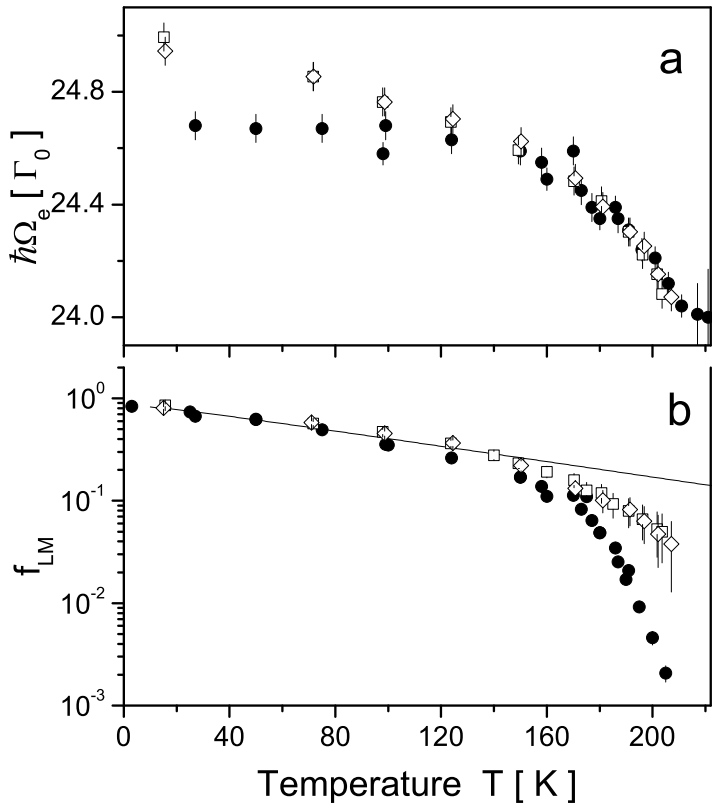

Figure 7.4: Temperature dependence of the quadrupole splitting $\hbar\Omega_e$ (a) and of the Lamb-Mössbauer factor f_{LM} (b) for the 25 Å (□), 50 Å (◊) and bulk (•) samples.

where the lower integration limit, 20 ns, is the beginning of the experimental time window, a' and a are proportionality coefficients. In the last expression ζ can be obtained unambiguously from the NFS intensity and R is directly measured. The proportionality coefficient a is obtained at 75 K, where $\zeta = \xi f_{LM}/2$. By this procedure, we obtain the effective thickness parameter $\xi f_{LM}/2$ which is shown as a function of temperature in Fig. 7.3b. One can see that ζ and $\xi f_{LM}/2$ almost coincide up to $\sim$ 140 K. Above this temperature the relaxation is activated and becomes visible in the experimental time window. Above 190 K the contribution of $\xi f_{LM}/2$ to ζ becomes negligible and the decay is defined mainly by the relaxation. In the temperature range 150-190 K both contributions to ζ are comparable. The correct value of $2\lambda_{NFS}$ here strongly depends on the correct measurement of the countrate R.

7.4 Results

The quadrupole splitting, the Lamb-Mössbauer factor and the relaxation rate are obtained from the fit for both nanoporous samples.

The temperature dependence of the quadrupole splitting $\hbar\Omega_e$ is shown in Fig. 7.4a. The data sets for both nanoporous samples almost coincide. The quadrupole splitting decreases linearly up to ∼160 K and falls down above. The low temperature linear dependence can be approximated as

$$\hbar\Omega_e \simeq 24.99(1 - 0.017 \cdot T/T_g) \tag{7.4}$$

where $T_g = 179\ K$ for DBP.

The quadrupole splitting observed in the bulk sample is also shown in the figure. It is clearly seen that data sets behave differently at low temperatures. The value of $\hbar\Omega_e$ at $T = 0$ K differs by ∼2% for nanoporous and bulk samples. Also the dependence on temperature below 160 K is more pronounced for the nanoporous samples. However, above 160 K all data sets almost coincide and show a characteristic non-linear decrease. This can be identified with fast rotational dynamics in a restricted angular range which leads to the same decrease of the quadrupole splitting for the bulk and nanoporous samples.

The temperature dependence of the Lamb-Mössbauer factor f_{LM} is shown in Fig. 7.4b for the nanoporous and the bulk samples. Absolute values of f_{LM} for the nanoporous samples were obtained from ξf_{LM} using the investigation of the same samples by NIS [ABvB$^+$03], where an absolute value of f_{LM} has been obtained at 85 K. As a result we obtain that the effective thickness ξ equals 3.0 for the 25 Å sample and 3.2 for the 50 Å sample. Using this information we obtain f_{LM}. The temperature dependence of the Lamb-Mössbauer factor for both nanoporous samples is almost the same. The comparison with the bulk sample shows that at low temperatures, where vibrations play a main role, the data sets for bulk and nanoporous samples show the same temperature dependence. However, at higher temperatures, the data sets deviate from each other. f_{LM} for the bulk sample is drastically decreased due to the softening of the glass former connected with fast β relaxation. On the other hand, f_{LM} in nanoporous samples shows a similar behaviour, but the decrease is much smaller. Thus softening also appears in the nanoporous samples but with a much smaller amplitude. The relatively small decrease of f_{LM} in the nanoporous samples is also seen from the following argument. The maximum temperature where experiments can be carried out is defined by a countrate ∼ 1 Hz. The countrate is proportional to the square of ξf_{LM}. For both, bulk and nanoporous samples, the maximum temperature was roughly the same, $205 \div 210$ K, which means that the values ξf_{LM} are the same. However, the effective thickness ξ for the bulk sample is at least 20 times larger than that for the nanoporous samples. Therefore, the Lamb-Mössbauer factor has to be

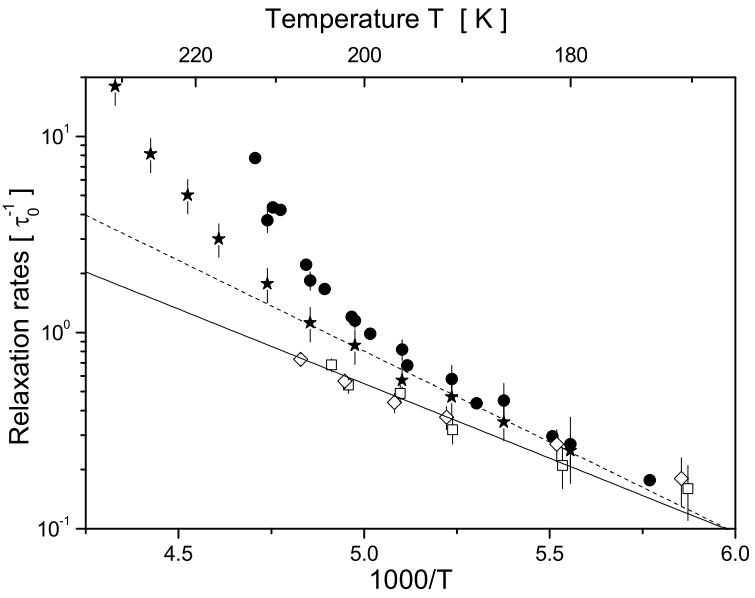

Figure 7.5: Temperature dependence of the relaxation rate $2\lambda_{NFS}$ measured by NFS in the 25 Å (□) and 50 Å (◊) samples and measured by NFS and MS in the bulk (•) sample. The rotational relaxation rate λ_2 measured by SRPAC in the bulk sample is also shown (★). The lines show low temperature Arrhenius behaviour for the nanoporous (solid line) and bulk (dashed line) samples.

20 times smaller. This ratio corresponds to the ratio of f_{LM} for the nanoporous and the bulk samples presented in the figure. Here one should also mention NIS measurements of similar samples [ABvB$^+$03]. The obtained partial density of states at the iron atom is suppressed at low energies as compared to the bulk.

Fig. 7.5 shows the inverse temperature dependence of the relaxation rate $2\lambda_{NFS}$ for the nanoporous and the bulk samples. Below 190 K both data sets follow an Arrhenius dependence on temperature. The slope is less pronounced for the nanoporous samples. The barrier energy ΔE of the Arrhenius law is ∼20% smaller for the nanoporous samples as compared to the bulk sample. We know that below 190 K, relaxation observed by NFS in the bulk sample is fully determined by rotational relaxation which follows an Arrhenius dependence on temperature. It is natural to assume that also in the nanoporous samples the Arrhenius behaviour is defined by rotational relaxation alone. This relaxation process is identified with the slow β relaxation for the bulk sample. The same should be true for the nanoporous samples.

Above 190 K $2\lambda_{NFS}$ observed in the bulk sample changes its behaviour and strongly increases with temperature. Such behaviour is not observed for the nanoporous samples.

Here, the relaxation rate follows the Arrhenius temperature dependence up to the maximal measured temperature. Since the increase of $2\lambda_{NFS}$ for the bulk sample was identified with structural α relaxation, we can say that this relaxational process is suppressed or shifted to higher temperatures for the nanoporous samples.

As conclusion, we do not see any difference in the dynamics of glass former in pores of 25 Å and 50 Ådiameters. As compared to the bulk, the rotational dynamics seen by the quadrupole splitting and by the relaxation rate is almost the same. On the other hand, fast β relaxation seen by the Lamb-Mössbauer factor and structural relaxation seen as the deviation of the relaxation rate from an Arrhenius temperature dependence is largely suppressed for the nanoporous samples. We can say that the restriction of the volume of the glass former leads to the suppression of the fast β relaxation and structural α relaxation while slow β relaxation identified with molecular rotation remains almost the same.

Chapter 8

Conclusion and Outlook

In this work a new method, Synchrotron Radiation based Perturbed Angular Correlation (SRPAC), has been developed theoretically and successfully applied to study dynamics of a glass forming liquid.

The theoretical description of this method is based on the theory of angular correlation which was worked out in the 60's-70's in application to the method of Time Differential Perturbed Angular Correlation (TDPAC). The influence of the rotational motion on SRPAC has been studied theoretically in the stochastic Markov approximation of dynamics and was expressed via rotational correlation functions $C_2(t)$ and $C_4(t)$. It is shown that the full dynamical region can be separated into fast and slow relaxation regimes. In the slow relaxation regime the relaxation is seen directly in time and both $C_2(t)$ and $C_4(t)$ can be obtained from the data. The comparison of the characteristic rates of these two correlation functions gives the possibility to extract information about the type of rotation. In the fast relaxation regime only integrated information about the dynamics can be obtained via the mean relaxation time of $C_2(t)$.

Both methods of nuclear resonant scattering, SRPAC and NFS, were applied to investigate dynamical features of probe ferrocene molecules in the glass former dibutyl phthalate for the transition from the glassy to the liquid state.

The rotational dynamics of the probes was measured by SRPAC in the frequency range of $2{\cdot}10^6 \div 4{\cdot}10^{10}$ Hz. For the temperature range where both SRPAC and NFS are accessible ($0.9T_g - 1.2T_g$, T_g is the caloric glass transition temperature), a separation of the dynamics into pure rotation and into translational motion of the center of mass has been performed. The results show that below $1.1T_g$ these dynamical processes with characteristic times longer than 100 ns decouple and exhibit a different dependence on temperature. The rotational motion has the higher frequencies, it still exists when translational motion is almost frozen out in the experimental time window.

Comparing these results to the data from dielectric spectroscopy, one finds that the

dynamics of the probe molecules reproduces the dynamics of the pure glass former. In particular, the rotational dynamics of the probes slows down along the dielectric spectroscopy data at temperatures down to $1.3T_g$. After a transition regime, it follows below $1.1T_g$ the slow β relaxation branch. On the other hand, the translational dynamics has similarities with the structural α relaxation. Our results support the concept of decoupling of the various types of motion below the critical temperature T_c as defined by mode coupling theory and suggest an identification of the slow β relaxation with non-translational molecular motion.

Together with slow dynamics seen directly in the experimental time window, fast localized motions were observed via the temperature dependence of the Lamb-Mössbauer factor and of the quadrupole splitting. The excess decrease of the Lamb-Mössbauer factor and of the quadrupole splitting with increasing temperature was identified with the appearance of localized relaxations which are interpreted as rattling and libration of the probe molecule, respectively. The obtained mean square displacement and mean square angular displacement show a similar behavior with temperature. Because of the characteristic square-root dependences of these effects we attribute them to fast β relaxation.

NFS was applied also to study dynamics of a glass former confined in nanoporous material with pores size of 25 and 50Å. Again the glass former dibutyl phthalate doped by ferrocene was chosen which gives the possibility to compare data with that obtained in the bulk case. The result shows no particular dependence on the size of the pores. For the used pore sizes the fast localized translational dynamics is suppressed and the fast rotational dynamics is almost the same as in the bulk case. The characteristic rate of the slow dynamics is similar to that obtained by SRPAC in the bulk sample and reduced as compared to the relaxation rate obtained by NFS. All this leads to the conclusion that the dynamics in nanopores is dominated by the rotational molecular motion and the translational dynamics is suppressed as compared with the bulk.

In an outlook, several tasks can be considered. The theoretical model which was used to explain the influence of dynamics on both NFS and SRPAC assumed a Markov character of relaxation. Also, only one relaxation process was taken into account. It would be interesting to consider how a more general model of relaxation would be seen in NFS and SRPAC.

The theoretical analysis of SRPAC shows that one can extract both the characteristic rate of relaxation and the model of rotation from the time evolution of the anisotropy. However, the experimental statistics did not allow us to obtain information about the model of rotation. This interesting task has to be solved in future.

The combination of NFS and SRPAC gives the unique possibility to obtain quantitative information about both the rotational and translational relaxation rates. The values obtained in such way can be compared with the independently obtained transla-

tional relaxation rate from neutron scattering and rotational relaxation rate from NMR. This allows to compare quantitatively the last two rates and gives important information about their coupling. Due to the lack of neutron scattering data on dibutyl phthalate we were not able to make this comparison in this work. In order to do so one can apply the combination of NFS and SRPAC to other glass forming liquids like glycerol or o-terphenyl which were investigated by many different techniques.

Possible applications of SRPAC are not restricted to soft condensed matter and to the ^{57}Fe isotope. The method can be used, in principle, as a high resolution spectroscopy to investigate excited states of other isotopes. SRPAC becomes especially important in the case of absence of or difficulties with the mother isotope, which makes impossible to use traditional TDPAC, or in the case of a high transition energy which restricts the use of NFS or MS to very low temperatures. In particular, the application of SRPAC to ^{61}Ni looks very promising. The appearance of nickel in many magnetic and biological compounds makes it important to obtain information about the hyperfine interactions experienced by the nuclei. First experiments which have been performed at the ESRF Nuclear Resonant beamline on a nickel metal foil enriched in ^{61}Ni demonstrates the principal possibility to observe SRPAC on this isotope. The temperature dependence of the measured magnetic hyperfine interaction reproduces the known decrease of the magnetization with temperature up to the Néel temperature. The relatively high countrate of these measurements allows one to plan investigations of nickel compounds under special conditions: on surfaces, under pressure, in biological compounds and etc.

Appendix A

Calculation of the NFS amplitude

As a basis for the calculation we use the expression obtained by Shvyd'ko [Shv99a] for the NFS amplitude

$$E(t) = \sum_{k=1}^{\infty} (-1)^k \frac{\xi^k}{k!} E^{(k)}(t) \tag{A.1}$$

where the multiple scattering amplitude of order k is formed from the self-correlation function $K(t)$ by the recursion relation

$$E^{(1)}(t) = \frac{E_0}{\tau_0} K(t) \tag{A.2}$$

$$E^{(k+1)}(t) = \frac{1}{\tau_0} \int_0^t \mathrm{d}\tilde{t} \cdot E^{(k)}(\tilde{t}) \cdot K(t - \tilde{t}) \tag{A.3}$$

This expression can be simplified by introducing $\tilde{K}(t)$ and $\psi^{(k)}(t)$ as

$$K(t) = \mathrm{e}^{-t/2\tau_0} \tilde{K}(t) \tag{A.4}$$

$$E^{(k+1)}(t) = \frac{E_0}{\tau_0} \mathrm{e}^{-t/2\tau_0} \left(\frac{t}{\tau_0}\right)^k \frac{1}{k!} \psi^{(k)}(t) \tag{A.5}$$

The recursion relation for $\psi^{(k)}(t)$ can be found by inserting eq. (A.5) into eq. (A.3)

$$\begin{aligned} &\frac{E_0}{\tau_0} \mathrm{e}^{-t/2\tau_0} \left(\frac{t}{\tau_0}\right)^k \frac{1}{k!} \psi^{(k)}(t) = \\ &= \frac{E_0}{\tau_0} \frac{1}{\tau_0} \int_0^t \mathrm{d}\tilde{t} \cdot \mathrm{e}^{-\tilde{t}/2\tau_0} \left(\frac{\tilde{t}}{\tau_0}\right)^{k-1} \frac{1}{(k-1)!} \psi^{(k-1)}(\tilde{t}) \cdot \tilde{K}(t - \tilde{t}) \mathrm{e}^{-(t-\tilde{t})/2\tau_0} \end{aligned} \tag{A.6}$$

$$\begin{aligned} \psi^{(k)}(t) &= \int_0^t \frac{\mathrm{d}\tilde{t}}{t} \left(\frac{\tilde{t}}{t}\right)^{k-1} k \cdot \psi^{(k-1)}(\tilde{t}) \cdot \tilde{K}(t - \tilde{t}) = \\ &= \int_0^1 \mathrm{d}\left(x^{k-1}\right) \psi^{(k-1)}(tx) \cdot \tilde{K}(t(1-x)) \end{aligned} \tag{A.7}$$

Decreasing the index in eq. (A.1) by one we come to the following expression for the NFS amplitude

$$E(t) = E_0 \frac{\xi}{\tau_0} \cdot \mathrm{e}^{-t/2\tau_0} \cdot \tilde{E}(t) \tag{A.8}$$

$$\tilde{E}(t) = \sum_{k=0}^{\infty} (-1)^k \frac{(\xi t/\tau_0)^k}{k!(k+1)!} \psi^{(k)}(t) \tag{A.9}$$

$$\psi^{(0)}(t) = \tilde{K}(t) \tag{A.10}$$

$$\psi^{(k+1)}(t) = \int_0^1 \mathrm{d}\left(x^k\right) \psi^{(k)}(tx) \cdot \tilde{K}(t(1-x)) \tag{A.11}$$

Here $\tilde{E}(t)$ reflects the influence of multiple scattering and relaxation on the NFS amplitude.

The most simple case corresponds to $\tilde{K}(t) = 1$ (no diffusion and no hyperfine splitting). Then $\psi^{(k)} = 1$ for any k and the sum reduces to the well known expression [KAK79]

$$\tilde{E}(t) = \frac{J_1(2\sqrt{\xi t/\tau_0})}{\sqrt{\xi t/\tau_0}} \equiv \sigma(\xi t/\tau_0) \tag{A.12}$$

where $J_1(x)$ is the Bessel function of the first kind and first order.

The second case which we consider here corresponds to the perturbation of the nuclear state by the quadrupole interaction with $\tilde{K}(t) = \cos(\Omega t/2)$. The calculation of $\psi^{(k)}(t)$ up to $k = 4$ using the reccurent eq. (A.11) gives the following expression for $\tilde{E}(t)$

$$\tilde{E}(t) = \sum_{k=0}^{\infty} (-1)^k \frac{(\xi t/2\tau_0)^k}{k!(k+1)!} \left(a_k(\Omega t) \cdot \cos(\Omega t/2) - \frac{\xi}{2\Omega\tau_0} b_k(\Omega t) \cdot \sin(\Omega t/2) \right) \tag{A.13}$$

where

$$\begin{aligned}
a_0(x) &= 1 & b_0(x) &= 1 \\
a_1(x) &= 1 & b_1(x) &= 1 \\
a_2(x) &= 1 & b_2(x) &= 1 + \frac{2}{x^2} \\
a_3(x) &= 1 - \frac{12}{x^2} & b_3(x) &= 1 + \frac{6}{x^2} \\
a_4(x) &= 1 - \frac{60}{x^2} & b_4(x) &= 1 + \frac{8}{x^2} + \frac{48}{x^4}
\end{aligned} \tag{A.14}$$

The deviation of the coefficients $a_k(\Omega t)$ and $b_k(\Omega t)$ from 1 is inverse proportional to $(\Omega t)^2$. If this value is large (large t and Ω not small) we can approximate $a_k(x)$ and $b_k(x)$ by 1, which results in

$$E(t) = E_0 \frac{\xi}{2\tau_0} \mathrm{e}^{-t/\tau_0} \cdot \sigma(\xi t/2\tau_0) \cdot \cos(\Omega t/2 + \xi/4\Omega\tau_0) \tag{A.15}$$

At last, we consider a self-correlation function which corresponds to the unsplit state and to the translational relaxation governed by the von Schweidler function

$$\tilde{K}(t) = 1 - (t\lambda_t)^\beta \tag{A.16}$$

In this case $\psi^{(k)}(t)$ can be presented as

$$\psi^{(k)}(t) = 1 - (\lambda_t t)^\beta \frac{\Gamma(1+\beta)k!}{\Gamma(k+\beta)} \tag{A.17}$$

Here we assume that λ_t is a small value and take into account only the first order of $(\lambda_t t)^\beta$. One can check the correctness of this expression inserting it to eq. (A.11)

$$\begin{aligned}
\psi^{(k+1)}(t) &= \int_0^1 \mathrm{d}\left(x^k\right) \cdot \left(1 - (\lambda_t t)^\beta \frac{\Gamma(1+\beta)k!}{\Gamma(k+\beta)} \cdot x^k\right) \cdot \left(1 - (\lambda_t t)^\beta (1-x)^\beta\right) \simeq \\
&\simeq 1 - (\lambda_t t)^\beta \left(\frac{\Gamma(1+\beta)k!}{\Gamma(k+\beta)} \int_0^1 \mathrm{d}\left(x^k\right) x^\beta + \int_0^1 \mathrm{d}\left(x^k\right)(1-x)^\beta\right) = \\
&= 1 - (\lambda_t t)^\beta \left(\frac{\Gamma(1+\beta)k!}{\Gamma(k+\beta)} \frac{k}{k+\beta} + \frac{\Gamma(1+\beta)k!}{\Gamma(1+k+\beta)}\right) = \\
&= 1 - (\lambda_t t)^\beta \frac{\Gamma(1+\beta)(k+1)!}{\Gamma(k+1+\beta)}
\end{aligned} \tag{A.18}$$

Inserting $\psi^{(k)}(t)$ into eq. (A.9) one obtains

$$\begin{aligned}
\tilde{E}(t) &= \sigma(\xi t/\tau_0) - (\lambda_t t)^\beta \Gamma(1+\beta) \sum_{k=0}^{\infty} (-1)^k \frac{(\xi t/\tau_0)^k}{\Gamma(k+\beta)(k+1)!} = \\
&= \sigma(\xi t/\tau_0) - (\lambda_t t)^\beta \sigma_\beta(\xi t/\tau_0)
\end{aligned} \tag{A.19}$$

where the generalized $\sigma_x(z)$ is introduced as

$$\sigma_x(z) = \Gamma(1+x) \sum_{k=0}^{\infty} (-1)^k \frac{z^k}{\Gamma(k+x)(k+1)!} \tag{A.20}$$

For $x = 1$ this function reduces to $\sigma(z)$.

Let t_i be the roots of $\tilde{E}(t)$ in the static case $\lambda_t = 0$, i.e. $\sigma(\xi t_i/\tau_0) = 0$. One can find the shifts Δt_i of the roots due to relaxation from an equation

$$\tilde{E}(t_i + \Delta t_i) = 0 \tag{A.21}$$

We assume that Δt_i is small, then we can expand the last expression in a Taylor series.

$$\tilde{E}(t_i) + \Delta t_i \tilde{E}'(t_i) = 0 \tag{A.22}$$

$$\Delta t_i \sigma'(\xi t_i/\tau_0) - (\lambda_t t_i)^\beta \sigma_\beta(\xi t_i/\tau_0) = 0 \tag{A.23}$$

Straightforward one can obtain an expression for the relative shift $\Delta t_i/t_i$ as a function of the relaxation rate

$$\frac{\Delta t_i}{t_i} = (\lambda_t t_i)^\beta C_i(\beta) \tag{A.24}$$

$$C_i(\beta) = \frac{\sigma_\beta(\xi t_i/\tau_0)}{\xi t_i/\tau_0 \cdot \sigma'(\xi t_i/\tau_0)} \tag{A.25}$$

Appendix B

Electric quadrupole interaction

The coupling between nucleus and environment is described by the electrostatic interaction of the nuclear charge and the electric and magnetic fields on the nucleus formed by its surroundings (electrons, crystal structure). The interaction Hamiltonian H can be described by [Kop94]

$$H = H_C + H_Q + H_M \tag{B.1}$$

where H_C refers to the Coulomb interaction between the nucleus and the electron density at the nuclear site, H_Q is the interaction between the nuclear quadrupole moment and the electric field gradient at the nucleus (electric quadrupole interaction), and H_M is the interaction between the nuclear magnetic dipole moment and the effective magnetic field at the nucleus (magnetic dipole interaction). Interactions of higher order of multipole expansion can be neglected because their energies are by several orders of magnitude smaller [Kop94].

If the distribution of the nuclear charge deviates from spherical symmetry then the nucleus has a quadrupole moment eQ_{ij} [GLT78], which is a tensor of second order. If the nuclear charge distribution has at least an axial symmetry then only one component of this tensor is nonzero. The quadrupole moment Q is positive for an elongated (cigar-shaped) nucleus, and negative for a flattened (pancake-shaped) nucleus. A quadrupole moment different from zero exists only for nuclear states with spin quantum number $I > 1/2$. The quadrupole moment interacts with a non-spherical electronic charge distribution at the nuclear site. The non-sphericity can be described by the electric field gradient (EFG) tensor, whose components are defined as the second derivatives of the electric potential V produced by extra-nuclear charges at the nuclear site ($V_{ij} = \partial^2 V / \partial x_i \partial x_j$). In contrast to nuclear charge distribution, the electronic charge distribution is generally not axially symmetric. It is nevertheless possible to find a principal axis coordinate system, where all non-diagonal components of V_{ij} vanish. Due to the Laplace's equation ($V_{xx} + V_{yy} + V_{zz} = 0$) and using the assumption $\mid V_{zz} \mid \geqslant \mid V_{xx} \mid \geqslant \mid V_{yy} \mid$ one can choose two independent

parameters to describe the EFG: $q \equiv V_{zz}/e$ and the asymmetry parameter η defined as $\eta = (V_{xx} - V_{yy})/V_{zz}$. The interaction Hamiltonian between the quadrupole moment of the nucleus in state I and the EFG at the site of the nucleus is

$$H_Q = \frac{e^2Qq}{4I(2I-1)}\left(3\hat{I}_z^2 - \hat{I}(\hat{I}+1) + \eta\left(\hat{I}_x^2 - \hat{I}_y^2\right)\right) \tag{B.2}$$

where hats over spins denote the operator nature of these values. Eigenvalues for this Hamiltonian in the case of $I = 3/2$, that is the value of spin for the excited state of ^{57}Fe, are

$$E_Q = \frac{e^2Qq}{12}\left(3m_I^2 - \frac{15}{4}\right)\sqrt{1+\eta^2/3} \tag{B.3}$$

where $m_I = I, I-1, \ldots, -I$ is the magnetic quantum number (projection of the spin to the z axis of the EFG coordinate system). The electric quadrupole interaction causes a splitting of the $(2I+1)$-fold degenerate energy level of a nuclear state into sub-levels characterized by the magnitude of the magnetic quantum number $\mid m_I \mid$. These levels can not be distinguished by the sign of the magnetic quantum number because of the presence of m_I to the second power in eq. (B.3), they are therefore always twofold degenerate. In the case of ^{57}Fe the ground state ($I = 1/2$) is not split by the EFG and the excited state ($I = 3/2$) splits into two twofold degenerate sublevels with $m_I = \pm 1/2$ and $m_I = \pm 3/2$. It is convenient to introduce the angular frequency Ω that is equivalent to the energy splitting between these states and also called the quadrupole splitting:

$$\hbar\Omega = e^2Qq/2 \tag{B.4}$$

where we assume that the EFG is axially symmetric ($\eta = 0$).

As the nuclear quadrupole moment is constant for each nuclear level, changes of the quadrupole splitting observed for the same compound under different experimental conditions result from changes of the EFG at the nucleus. One can consider two sources which contribute to the EFG [GLT78]: charges on distant ions which surround the Mössbauer atom in a non-cubic symmetry, called lattice contribution, and anisotropic electron distribution in the valence shell of the Mössbauer atom, called valence electron contribution.

Appendix C

Calculation of the SRPAC intensity

The probability of the incoherent scattering of a SR pulse is proportional to the angular correlation function for two successive radiations emitted from an initial random state with the perturbing interactions acting on the intermediate state. An expression for the general form of this function was derived by R. M. Steffen and K. Alder (see eq. (13.137) in [SA75]).

For the incoherent NRS of SR we can make some assumptions. First, we assume that the multipolarity of the photon which accompanies to the nuclear transitions is fixed to one value (M1 for the $1/2 \rightarrow 3/2$ transition of ^{57}Fe). Second, the incoming beam is assumed to be polarized in the horizontal plane, whereas the polarization of the scattered photon is not observed. Third, we assume that the perturbing interactions on the ensemble of nuclei are isotropic, i.e. the overall effect on the ensemble is such that it does not introduce a privileged direction in space.

Using eqs. (13.137,12.293,13.107) of [SA75], the probability of incoherent NRS of the incoming photon with direction $\mathbf{k}_{in}$ and polarization σ_{in} scattered into the direction $\mathbf{k}_{out}$ and divergence $d\Omega_{out}$ is:

$$dW(\mathbf{k}_{in}\sigma_{in}, \mathbf{k}_{out}; t) = \frac{d\Omega_{out}}{4\pi} \sum_{l,q,q'} B^*_{lq}(\gamma_{in}, \sigma_{in}) \cdot D^{(l)}_{qq'}((\mathbf{k}_{in}\sigma_{in} \rightarrow S_k) \cdot G_{ll}(t) \cdot A_l(\gamma_{out}) \cdot D^{(l)}_{q'0}(S_k \rightarrow \mathbf{k}_{out}) \tag{C.1}$$

Here $G_{ll}(t)$ is a perturbation factor which completely describes the dynamics of the nucleus, $D^{(l)}_{qq'}(\mathbf{k}_{in}\sigma_{in} \rightarrow S_k)$ is the matrix element of the rotation from the coordinate system connected with the incoming photon ($\mathbf{k}_{in}$ - Z-axis and σ_{in} - X-axis) to the coordinate system connected with nucleus (S_k), $D^{(l)}_{q'0}(S_k \rightarrow \mathbf{k}_{out})$ is the matrix element of the rotation from the coordinate system S_k to the coordinate system connected with the outcoming photon ($\mathbf{k}_{out}$ - Z-axis), and coefficients A and B will be defined below. This expression

can be simplified further to

$$dW(\mathbf{k}_{in}\sigma_{in},\mathbf{k}_{out};t)=\frac{d\Omega_{out}}{4\pi}\sum_{l,q}B^{*}_{lq}(\gamma_{in},\sigma_{in})A_l(\gamma_{out})G_{ll}(t)\cdot\sqrt{\frac{4\pi}{2l+1}}Y^{*}_{lq}(\phi',\vartheta') \qquad (C.2)$$

where we use the relation:

$$\sum_q D^{(l)}_{qq'}(\Omega_1)D^{(l)}_{q'0}(\Omega_2)=D^{(l)}_{q0}(\Omega_1\Omega_2)=\sqrt{\frac{4\pi}{2l+1}}Y^{*}_{lq}(\phi',\vartheta') \qquad (C.3)$$

Here ϕ' and ϑ' are the angles that define the direction of the scattered beam in the coordinate system connected with the incoming beam. The coefficients $B_{lq}(\gamma,\sigma)$ and $A_l(\gamma)$ are (see eqs. (12.232) and(12.182) in [SA75]):

$$B_{l0}(\gamma,\sigma) = A_l(\gamma)=F_l(L,L,I_g,I_e) \qquad (C.4)$$

$$B_{l\pm1}(\gamma,\sigma) = 0 \qquad (C.5)$$

$$B_{l\pm2}(\gamma,\sigma) = \frac{1}{4}\sqrt{\frac{(l+2)!}{(l-2)!}}F_l(L,L,I_g,I_e) \qquad (C.6)$$

where L is the multipolarity of radiation, I_g and I_e are the spins of the ground and excited states, and $F_l(L,L,I_g,I_e)$ is given by eq. (12.168) in[SA75]

$$F_l(L,L,I_g,I_e)=(-1)^{I_g+I_e-1}(2L+1)\sqrt{(2l+1)(2I_e+1)}\begin{pmatrix}L & L & l\\ 1 & -1 & 0\end{pmatrix}\begin{Bmatrix}L & L & l\\ I_e & I_e & I_g\end{Bmatrix} \qquad (C.7)$$

The sum over q in eq. (C.2) can be taken in the following way:

$$\begin{aligned}
&\sqrt{\frac{4\pi}{2l+1}}\sum_q B_{lq}\cdot Y^{*}_{lq}(\phi',\vartheta')=\\
&\sqrt{\frac{4\pi}{2l+1}}\cdot\left(B_{l0}\cdot Y^{*}_{l0}(\phi',\vartheta')+B_{l2}\cdot Y^{*}_{l2}(\phi',\vartheta')+B_{l-2}\cdot Y^{*}_{l-2}(\phi',\vartheta')\right)=\\
&B_{l0}P_l(\cos\vartheta')+\sqrt{\frac{4\pi}{2l+1}}B_{l2}\cdot 2Re(Y_{l2}(\phi',\vartheta'))=\\
&A_l\left(P_l(\cos\vartheta')+\frac{1}{2}P_{l2}(\cos\vartheta')\cdot\cos 2\phi'\right)
\end{aligned} \qquad (C.8)$$

where $P_l(x)$ is a Legendre polynomial and $P_{l2}(x)$ is an associated Legendre polynomial [AS70]. Using this relation the probability of the scattering can be written as

$$dW(\mathbf{k}_{in}\sigma_{in},\mathbf{k}_{out};t)=\frac{d\Omega_{out}}{4\pi}\sum_l A^2_l(\gamma)\cdot G_{ll}(t)\cdot\left(P_l(\cos\vartheta')+\frac{1}{2}P_{l2}(\cos\vartheta')\cdot\cos 2\phi'\right) \qquad (C.9)$$

where the coefficient l varies in the region $0\leqslant l\leqslant min(2L,2I_e)$.

For many isotopes (^{57}Fe, ^{119}Sn, ^{61}Ni) the multipolarity L equals 1. Then, the sum in eq. (C.9) is restricted by two terms with $l=0$ and 2. The first term equals 1. The

term for $l = 2$ simplifies turning to another coordinate system, where the z-axis coincides with the vertical direction. We define ϑ and ϕ as a polar and azimuthal angles in this coordinate system. Then

$$P_2(\cos\vartheta') + \frac{1}{2}P_{22}(\cos\vartheta') \cdot \cos 2\phi' = -2P_2(\cos\vartheta) \tag{C.10}$$

Finally the angular probability can be written as

$$\frac{dW(\vartheta;t)}{d\vartheta d\phi} = \frac{1}{4\pi}\left(1 - 2A_2^2(\gamma)P_2(\cos\vartheta)G_{22}(t)\right) \tag{C.11}$$

The result obtained for SRPAC can be compared with the angular probability for the directional TDPAC, which for $L = 1$ can be written as [SA75]

$$\frac{dW(\vartheta';t)}{d\vartheta' d\phi'} = \frac{1}{4\pi}\left(1 + A_2(\gamma_1)A_2(\gamma_2)P_2(\cos\vartheta')G_{22}(t)\right) \tag{C.12}$$

In application to the ^{57}Fe isotope the spin transition $1/2 \rightarrow 3/2$ is observed by SRPAC and a cascade of spins $5/2 \rightarrow 3/2 \rightarrow 1/2$ is observed by TDPAC. The values of the anisotropy coefficients are $A_2(\gamma) = 1/2$ for SRPAC and $A_2(\gamma_1) = 1/10$, $A_2(\gamma_2) = 1/2$ for TDPAC. The corresponding angular probabilities reduce to

$$\frac{dW(\vartheta;t)}{d\vartheta d\phi} = \frac{1}{4\pi}\left(1 - \frac{1}{2}P_2(\cos\vartheta)G_{22}(t)\right) \tag{C.13}$$

for SRPAC and

$$\frac{dW(\vartheta';t)}{d\vartheta' d\phi'} = \frac{1}{4\pi}\left(1 + \frac{1}{20}P_2(\cos\vartheta')G_{22}(t)\right) \tag{C.14}$$

for TDPAC. One can see that the coefficient before the perturbation factor is 10 times larger for the SRPAC. This difference partly appears due to the polarization and partly due to the low spin of the ground state.

Appendix D

Calculation of $G_{22}(t)$ by the eigensystem method

The time evolution of the nuclear state driven by quadrupole interaction and stochastic reorientation is described by eq. (4.10). Additionally one needs to introduce a representation of the nuclear and stochastic states in order to get an expression for the perturbation factor. It was found by Winkler [Win76] that the coupled representation $\mid x(Ff, Jk; \kappa))$ is quite convenient for this purpose:

$$\mid x(Ff, Jk; \kappa)) = \sum_{N\mu} \langle J\mu kN \mid Ff\rangle \mid J, \mu\kappa) \mid kN) \tag{D.1}$$

where angular brackets denote Clebsch-Gordan coefficient, $\mid J, \mu\kappa)$ describes the molecular orientation in angular momentum space and $\mid kN)$ is the density matrix of the nuclear state in the spherical tensor representation (for an explanation of this representation see [Blu81]).

Then the perturbation factor is given by projection of the operator $\hat{U}(t)$ to the element $|X(k0, 0k, 0))$ of the X representation (see eqs.(42) and(44) in [Win76])

$$G_{kk}(t) = (x(k0, 0k, 0)| \exp\left[\left(-\frac{i}{\hbar}\mathcal{H}^{\times} + \hat{R}\right)t\right] |x(k0, 0k, 0)) \tag{D.2}$$

Using information about the projection of the operator $\hat{R}$ to $\mid J, \mu\kappa)$ (see eq. (4.17)) one can rewrite eq. (34) in [Win76] as

$$(x(F_2f_2, J_2k_2; \kappa_2)|\hat{R}|x(F_1f_1, J_1k_1; \kappa_1)) = -\lambda_{J_1} \cdot \delta_{J_1J_2}\delta_{f_1f_2}\delta_{F_1F_2}\delta_{k_1k_2}\delta_{\kappa_1\kappa_2} \tag{D.3}$$

and for the Liouville operator of the quadrupole interaction (eqs. (39) and (40) in [Win76])

$$\begin{aligned}(x(F_2f_2, J_2k_2; \kappa_2)|\mathcal{H}^{\times}|x(F_1f_1, J_1k_1; \kappa_1) &= \delta_{F_1F_2}\delta_{f_1f_2}\delta_{\kappa_1\kappa_2} \cdot \hbar\Omega\sqrt{5} \cdot \\ \cdot (-1)^{F_1+\kappa_1+1} &\cdot \left((-1)^{k_1+k_2} - 1\right) \cdot \sqrt{(2J_1+1)(2k_1+1)(2J_2+1)(2k_2+1)} \cdot \\ \cdot \begin{pmatrix} J_1 & J_2 & 2 \\ -\kappa_1 & \kappa_1 & 0 \end{pmatrix} &\cdot \begin{Bmatrix} k_1 & k_2 & 2 \\ J_2 & J_1 & F_1 \end{Bmatrix} \cdot \begin{Bmatrix} k_1 & k_2 & 2 \\ 3/2 & 3/2 & 3/2 \end{Bmatrix}\end{aligned} \tag{D.4}$$

where figure brackets denote a 6j-symbol and, as compared with [Win76], we take into account the quadrupole character of the hyperfine interaction.

The next step is to build the matrix $\hat{A}$

$$\hat{A} = -\frac{i}{\hbar}\mathcal{H}^{\times} + \hbar R \tag{D.5}$$

in the x-representation. To decrease the dimension of this matrix one can use the property that only states which couple with the state $|x(k0,0k;0))$ have to be taken into account where $k = 2$ since we are interested in the calculation of $G_{22}(t)$. It follows immediately that $F_1 = F_2 = 2$, $f_1 = f_2 = 0$ and $\kappa_1 = \kappa_2 = 0$. Looking to the indexes J and k we obtain that only 5 states are coupled with $\{J,k\} = \{0,2\}$. Therefore the matrix $\hat{A}$ is a 6×6 matrix in the representation $\{J,k\} : \{0,2\},\{2,1\},\{2,2\},\{2,3\},\{4,2\},\{4,3\}$. Below we give a precise expression for this matrix.

$$\hat{A} = \hbar\Omega \cdot \begin{pmatrix} 0 & i\sqrt{\frac{6}{25}} & 0 & -i\sqrt{\frac{14}{25}} & 0 & 0 \\ i\sqrt{\frac{6}{25}} & -\frac{\lambda_2}{\hbar\Omega} & -i\sqrt{\frac{3}{35}} & 0 & -i\sqrt{\frac{48}{175}} & 0 \\ 0 & -i\sqrt{\frac{3}{35}} & -\frac{\lambda_2}{\hbar\Omega} & -i\sqrt{\frac{64}{245}} & 0 & -i\sqrt{\frac{18}{49}} \\ -i\sqrt{\frac{14}{25}} & 0 & -i\sqrt{\frac{64}{245}} & -\frac{\lambda_2}{\hbar\Omega} & i\frac{3}{35} & 0 \\ 0 & -i\sqrt{\frac{48}{175}} & 0 & i\frac{3}{35} & -\frac{q\lambda_2}{\hbar\Omega} & -i\sqrt{\frac{10}{49}} \\ 0 & 0 & -i\sqrt{\frac{18}{49}} & 0 & -i\sqrt{\frac{10}{49}} & -\frac{q\lambda_2}{\hbar\Omega} \end{pmatrix} \tag{D.6}$$

Here we introduce the parameter $q = \lambda_4/\lambda_2$.

The next step will be to diagonalize this matrix, i.e. to find a set of eigenvalues $\varepsilon^{(j)}$ and normalized eigenvectors $\vec{v}^{(i)}$ which solve the equation

$$\hat{A}\vec{v}^{(j)} = \varepsilon^{(j)}\vec{v}^{(j)} \tag{D.7}$$

After this set is found the perturbation factor is calculated as

$$G_{22}(t) = \sum_{j=1}^{6} |v_0^{(j)}|^2 \mathrm{e}^{\varepsilon^{(j)}t} \tag{D.8}$$

In Fig. D.1 we give a program code written in "Mathematica-2.4" software which calculates $G_{22}(t)$

The presented method gives the numerical solution of the perturbation factor for any values of the parameters of the relaxation λ_2 and q. An analytical solution can not be obtained in the general case. However, an analytical approximation of the perturbation factor for the case of a small value of the relaxation rate λ_2 can be found.

The set of eigenvalues $\varepsilon^{(i)}$ is the solution of the equation

$$det|\hat{A} - \varepsilon\hat{1}| = 0 \tag{D.9}$$

Simulation of the perturbation factor $G_{22}(t)$

Initial parameters of the model are $\lambda 2$, q and Ω.

```
Ω = 24; λ2 = 5; q = 3;
```

Definition of the matrix A

$$\mathbf{A} = \Omega * \mathbf{N}\left[\begin{pmatrix} 0 & \frac{1}{5}i\sqrt{6} & 0 & -\frac{1}{5}i\sqrt{14} & 0 & 0 \\ \frac{1}{5}i\sqrt{6} & \frac{-\lambda 2}{\Omega} & -i\sqrt{\frac{3}{35}} & 0 & -\frac{4}{5}i\sqrt{\frac{3}{7}} & 0 \\ 0 & -i\sqrt{\frac{3}{35}} & \frac{-\lambda 2}{\Omega} & -\frac{8i}{7\sqrt{5}} & 0 & -\frac{3}{7}i\sqrt{2} \\ -\frac{1}{5}i\sqrt{14} & 0 & -\frac{8i}{7\sqrt{5}} & \frac{-\lambda 2}{\Omega} & \frac{3i}{35} & 0 \\ 0 & -\frac{4}{5}i\sqrt{\frac{3}{7}} & 0 & \frac{3i}{35} & \frac{-\lambda 2\, q}{\Omega} & -\frac{1}{7}i\sqrt{10} \\ 0 & 0 & -\frac{3}{7}i\sqrt{2} & 0 & -\frac{1}{7}i\sqrt{10} & \frac{-\lambda 2\, q}{\Omega} \end{pmatrix}\right];$$

Solution of the eigensystem problem

```
{ϵ, v} = Eigensystem[A];
```

Normalization of the vectors v and extracting $\left| v_1^{(j)} \right|^2$

```
u = Table[v[[j,1]]^2 / Σ_{i=1}^{6} v[[j,i]]^2, {j, 1, 6}];
```

Calculation of the perturbation factor

```
G[t_] = Re[Σ_{j=1}^{6} u[[j]] * e^(ϵ[[j]] t)];
```

Simulation of the perturbation factor and saving data

```
DataSim = Table[{t, G[t]}, {t, 0, 3, 0.01}];
ListPlot[DataSim, PlotJoined → True, PlotRange → All]
SetDirectory["./science/srpac/Theory"];
Export["g-rdm-d2-Q24.dat", DataSim, "Table"];
```

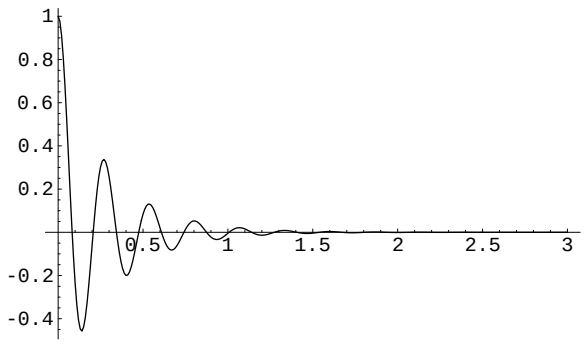


```
- Graphics -
```

Figure D.1: "Mathematica-2.4" program code for the simulation of the perturbation factor.

which is an equation of 6-th power and can not be solved analytically in general. For the static case when $\lambda_2 = 0$, this equation degenerates and gives the roots:

$$\begin{aligned} \varepsilon_0^{(1)} &= \varepsilon_0^{(4)} = 0 \\ \varepsilon_0^{(2)} &= \varepsilon_0^{(5)} = i\Omega \\ \varepsilon_0^{(3)} &= \varepsilon_0^{(6)} = -i\Omega \end{aligned} \tag{D.10}$$

which correspond to the exponent indexes of the statical perturbation factor

$$G_{22}(t) = \frac{1}{5} \cdot \mathrm{e}^{0 \cdot t} + \frac{2}{5} \left(\mathrm{e}^{i\Omega t} + \mathrm{e}^{-i\Omega t} \right) \tag{D.11}$$

In order to solve eq. (D.9) for small λ_2 we consider the roots in the shape of a Taylor series

$$\varepsilon^{(i)} = \varepsilon_0^{(i)} + a^{(i)}\lambda_2 + b^{(i)}\lambda_2^2 \tag{D.12}$$

up to the second order of λ_2. Then eq. (D.9) has to be equivalent to $\prod_{i=1}^{6}(\varepsilon - \varepsilon^{(i)})$. The equivalence implies that the coefficients of any power of ε have to be the same up to the second order of λ_2. The obtained system of equations can be solved and gives the following roots (up to the first order of λ_2)

$$\varepsilon^{(1)} = -\frac{2}{35}(5 + 9q)\lambda_2 \qquad \varepsilon^{(4)} = -\frac{1}{7}(4 + 3q)\lambda_2 \tag{D.13}$$

$$\varepsilon^{(2)} = i\Omega - (A - B)\lambda_2 \qquad \varepsilon^{(5)} = i\Omega - (A + B)\lambda_2 \tag{D.14}$$

$$\varepsilon^{(3)} = -i\Omega - (A - B)\lambda_2 \qquad \varepsilon^{(6)} = -i\Omega - (A + B)\lambda_2 \tag{D.15}$$

where

$$A = (75 + 37q)/140 \tag{D.16}$$

$$D = \sqrt{1009q^2 - 450q + 225}/140 \tag{D.17}$$

Six roots appear in this common solution which is valid for any q. However, looking to the analytical solution for the SCM with $q = 1$ (see eq. (E.17)) we can conclude that only three roots are physical and have to be taken into account. In the SCM the eigenvalues are: $-4\lambda_2/5$ and $\pm i\Omega - 3\lambda_2/5$. Comparing these values with $\varepsilon^{(1)}$-$\varepsilon^{(6)}$ at $q = 1$ we obtain that $\varepsilon^{(1)}$, $\varepsilon^{(2)}$ and $\varepsilon^{(3)}$ have to be taken as exponent indexes. Using the obtained eigenvalues one can find the deviation of the coefficients $v_0^{(j)}$ from the static case using eq. (D.7). Here we will not do it and use the static values. Then the perturbation factor can be written as

$$G_{22}(t) = \frac{1}{5}\mathrm{e}^{-p_h t} + \frac{4}{5}\mathrm{e}^{-p_o t}\cos(\Omega_e - \phi) \tag{D.18}$$

$$p_h = \lambda_2 \frac{2}{35}(5 + 9q) \tag{D.19}$$

$$p_o = \lambda_2 \frac{75 + 37q - \sqrt{1009q^2 - 450q + 225}}{140} \tag{D.20}$$

The shift of the precession frequency Ω to Ω_e and phase shift ϕ are not calculated precisely here. The solution of eq. (D.9) up to the third order of λ_2 is necessary for this purpose.

Appendix E

Calculation of $G_{22}(t)$ by the resolvent method

The calculation of the perturbation factor in the SCM can be done in the resolvent formalism that was developed by Blume and Dattagupta in application to TDPAC and MS [Dat87, Dat81].

This method considers the Laplace image of the perturbation factor

$$G_{22}(\lambda) = \int_0^\infty \mathrm{d}t G_{22}(t) \mathrm{e}^{-\lambda t} \tag{E.1}$$

In the static case the Laplace transformation of eq. (4.6) leads to

$$G_{22}^0(\lambda) = \frac{1}{5}\left(\frac{1}{\lambda} + \frac{4\lambda}{\lambda^2 + \Omega^2}\right) \tag{E.2}$$

The theory predicts that the modification of the perturbation factor due to relaxation can be expressed in the frame of SCM as (see eq. (4.27) in [Dat81])

$$G_{22}(\lambda) = \frac{G_2^0(\lambda + \lambda_2)}{1 - \lambda_2 G_2^0(\lambda + \lambda_2)} \tag{E.3}$$

where λ_2 is the SCM jump rate introduced in eq. (4.16). After inserting the expression for the static perturbation factor this equation can be written as

$$G_{22}(p) = \frac{1}{\Omega} \frac{p^2 + 2pp_2 + p_2^2 + 1/5}{p^3 + 2p^2 p_2 + p(p_2^2 + 1) + 4p_2/5} \tag{E.4}$$

where $p = \lambda/\Omega$ and $p_2 = \lambda_2/\Omega$. To make the inverse Laplace transform to the time variable one has to expand this expression in simple fractions and has therefore to find the roots of the denominator. This can be performed analytically for an equation of the third power. Notice that for TDPAC and SRPAC the power of the denominator is equal $2L$ where L is the spin of the excited state. $L = 3/2$ in the case of ^{57}Fe and $L = 5/2$ for

the usual TDPAC isotopes. This leads to the third and fifth power of the denominator, correspondingly. In the TDPAC case only a numerical solution is possible [Dat81].

Expanding eq. (E.4) and making the inverse Laplace transformation we get the expression for the perturbation factor in the time domain

$$G_{22}(t) = A\mathrm{e}^{-\alpha\Omega t} + B\mathrm{e}^{-\beta\Omega t}\cos(\gamma\Omega t) + C\mathrm{e}^{-\beta\Omega t}\sin(\gamma\Omega t) \tag{E.5}$$

where

$$\begin{aligned}
\alpha &= \frac{2}{3}p_2 - s && \text{(E.6)}\\
\beta &= \frac{2}{3}p_2 + \frac{1}{2}s && \text{(E.7)}\\
\gamma &= \frac{\sqrt{3}}{2}r && \text{(E.8)}\\
A &= \frac{4}{135}\frac{9 + 45s^2 + 30sp_2 + 5p_2^2}{r^2 + 3s^2} && \text{(E.9)}\\
B &= \frac{1}{135}\frac{135r^2 + 225s^2 - 120sp_2 - 4(9 + 5p_2^2)}{r^2 + 3s^2} && \text{(E.10)}\\
C &= \frac{\sqrt{3}}{135}\frac{-45s^3 + 60r^2p_2 + 60s^2p_2 + s(45r^2 - 4(9 + 5p_2^2))}{r(r^2 + 3s^2)} && \text{(E.11)}\\
s &= u + v && \text{(E.12)}\\
r &= u - v && \text{(E.13)}\\
u &= \left(\frac{p_2^3}{27} - \frac{p_2}{15} + w\right)^{1/3} && \text{(E.14)}\\
v &= \left(\frac{p_2^3}{27} - \frac{p_2}{15} - w\right)^{1/3} && \text{(E.15)}\\
w &= \sqrt{\frac{5p_2^4 - 22p_2^2 + 25}{675}} && \text{(E.16)}
\end{aligned}$$

The dependence of the coefficients α, β, γ and A, B, C on λ_2/Ω is shown in the Fig. E.1.

This rather complicated expression for $G_{22}(t)$ strongly simplified in the case of slow and fast relaxation.

The slow relaxation regime is defined by $\lambda_2/\Omega << 1$. Then, up to the second order of λ_2/Ω, the perturbation factor can be written as

$$\begin{aligned}
G_{22}(t) &\simeq \frac{1}{5}\mathrm{e}^{-4\lambda_2 t/5} + \frac{4}{5}\mathrm{e}^{-3\lambda_2 t/5}\cos(\Omega_e t - \phi) && \text{(E.17)}\\
\Omega_e &= \Omega\left(1 - \frac{4\lambda_2^2}{25\Omega^2}\right) && \text{(E.18)}\\
\phi &= \frac{4\lambda_2}{5\Omega} && \text{(E.19)}
\end{aligned}$$

The fast relaxation regime is defined by $\lambda_2/\Omega >> 1$ and, up to the first order of Ω/λ_2,

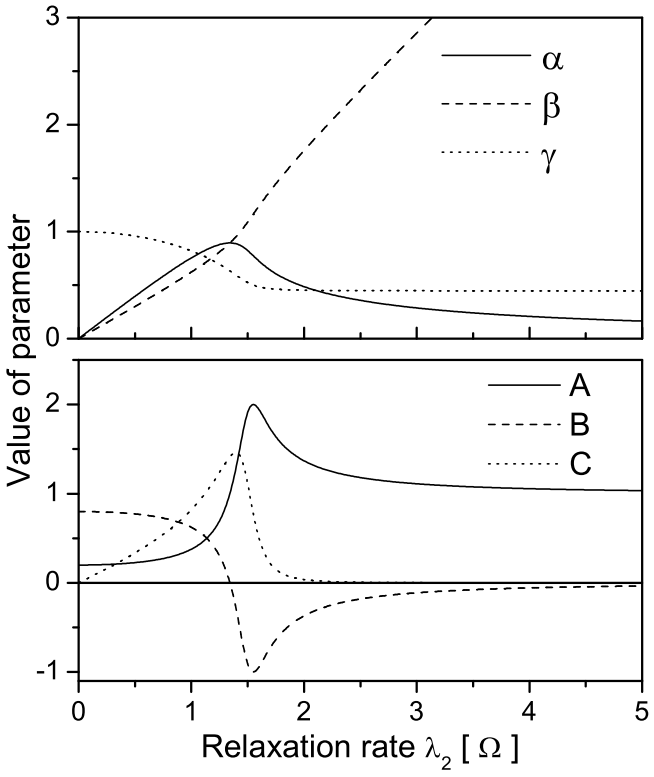

Figure E.1: Dependence of the coefficients A, B, C and α, β, γ in eq. (E.5) on λ_2/Ω.

the perturbation factor is expressed as

$$G_{22}(t) \simeq \exp\left(-\frac{4\Omega^2}{5\lambda_2}t\right) \tag{E.20}$$

Bibliography

[ABvB+03] T. Asthalter, M. Bauer, U. van Bürck, I. Sergueev, H. Franz, and A. I. Chumakov. *Hyp. Int.*, 144/145:77, 2002.

[AK64] A. M. Afanas'ev and Yu. Kagan. *Soviet Physics JETP*, 18:1139, 1964.

[AM72] A. Abras and J. G. Mullen. *Phys. Rev. A*, 6:2343, 1972.

[And72] J. E. Anderson. *Faraday. Symp. Chem. Soc.*, 6:82, 1972.

[Ang91] C. A. Angell. *J. Non-Cryst. Solids*, 131-133:13, 1991.

[Ang95] C. A. Angell. *Science*, 267:1924, 1995.

[ANM+00] C. A. Angell, K. L. Ngai, G. B. McKenna, P. F. McMillan, and S. W. Martin. *J. Appl. Phys.*, 88:3113, 2000.

[AP53] A. Abragam and R. V. Pound. *Phys. Rev.*, 92:943, 1953.

[ARCF96] A. Arbe, D. Richter, J. Colmenero, and B. Farado. *Phys. Rev. E*, 54:3853, 1996.

[AS70] M. Abramowitz and I. A. Stegun. *Handbook of Mathematical Functions*. Dover Publications, 9 edition, 1970.

[ASF+01] T. Asthalter, I. Sergueev, H. Franz, R. Rüffer, W. Petry, K. Messel, P. Härter, and A. Huwe. *Eur. Phys. J. B*, 22:301, 2001.

[ASG+97] M. Arndt, R. Stannarius, H. Groothues, E. Hempel, and F. Kremer. *Phys. Rev. Lett.*, 79:2077, 1997.

[Bar01] A. Barla. PhD Thesis. University of Cologne, 2000.

[BCR+96] A. Q. R. Baron, A. I. Chumakov, R. Rüffer, H. Grünsteudel, H. F. Grünsteudel, and O. Leupold. *Europhys. Lett.*, 34:331, 1996.

[BDHR01] R. Böhmer, G. Diezemann, G. Hinze, and E. Rössler. *Prog. Nucl. Magn. Reson. Spectrosc.*, 39:191, 2001.

[BEHW63] D. St. P. Bunbury, J. A. Elliott, H. E. Hall, and J. M. Williams. *Physics Letters*, 6:34, 1963.

[BFM+97] A. Q. R. Baron, H. Franz, A. Meyer, R. Rüffer, A. I. Chumakov, E. Burkel, and W. Petry. *Phys. Rev. Lett.*, 79:2823, 1997.

[BGCF02] D. D. Brace, S. D. Gottke, H. Cang, and M. D. Fayer. *J. Chem. Phys.*, 116:1598, 2002.

[BGS84] U. Bengtzelius, W. Götze, and A. Sjölander. *J. Phys. C*, 17:5915, 1984.

[BHS94] U. Bergmann, J. B. Hastings, and D. P. Siddons. *Phys. Rev. B*, 49:1513, 1994.

[Blu68] M. Blume. *Phys. Rev.*, 174:351, 1968.

[Blu81] K. Blum. *Density matrix theory and applications*. Plenum Press, 1981.

[BNAP93] R. Böhmer, K. L. Ngai, C. A. Angell, and D. J. Plazek. *J. Chem. Phys.*, 99:4201, 1993.

[BRM97] A. Q. Baron, R. Rüffer, and J. Metge. *Nucl. Instr. and Meth. A*, 400:124, 1997.

[But96] T. Butz. *Z. Naturforsch. A*, 51:396, 1996.

[CBR+98] A. I. Chumakov, A. Barla, R. Rüffer, J. Metge, H. F. Grünsteudel, and H. Grünsteudel. *Phys. Rev. B*, 58:254, 1998.

[Cha79] D. C. Champeney. *Rep. Prog. Phys.*, 42:1017, 1979.

[CHK+96] I. Chang, H. Hartmann, Yu. Krupyanskii, A. Zharikov, and F. Parak. *Chem. Physics*, 212:221, 1996.

[CHR75] D. C. Champeney, E. S. M. Higgy, and R. G. Ross. *J. Phys. C: Solid State Phys.*, 8:507, 1975.

[Chu03] A. I. Chumakov, 2003. Private communication.

[CLH+97] H. Z. Cummins, Gen Li, Y. H. Hwang, G. Q. Shen, W. M. Du, J. Hernandez, and N. J. Tao. *Z. Phys. B*, 103:501, 1997.

[CRG+95] A. I. Chumakov, R. Rüffer, H. Grünsteudel, H. F. Grünsteudel, G.Grübel, J. Metge, and H. A. Goodwin. *Europhys. Lett.*, 30:427, 1995.

[CS63] P. P. Craig and N. Sutin. *Phys. Rev. Lett.*, 11:460, 1963.

[CSZ+92] A. I. Chumakov, G. V. Smirnov, M. V. Zelepukhin, U. van Bürck, E. Gerdau, R. Rüffer, and H. D. Rüter. *Europhys. Lett.*, 17:269, 1992.

[Dat75] S. Dattagupta. *Phys. Rev. B*, 12:47, 1975.

[Dat76] S. Dattagupta. *Phys. Rev. B*, 14:1329, 1976.

[Dat81] S. Dattagupta. *Hyp. Int.*, 11:77, 1981.

[Dat87] S. Dattagupta. *Relaxation Phenomena in Condensed Matter Physics.* Academic Press, 1987.

[DB74] S. Dattagupta and M. Blume. *Phys. Rev. B*, 10:4540, 1974.

[Deb13] P. Debye. *Ber. Deut. Phys. Ges.*, 55:777, 1913.

[DOR56] J. D. Dunitz, L. E. Orgel, and A. Rich. *Acta Cryst.*, 9:373, 1956.

[DT87] S. A. Dzyuba and Yu. D. Tsvetkov. *J. Struct. Chem.*, 28:343, 1987.

[DWN+90] P. K. Dixon, L. Wu, S. R. Nagel, B. D. Williams, and J. P. Carini. *Phys. Rev. Lett.*, 65:1108, 1990.

[Dzu96] S. A. Dzuba. *Phys. Lett. A*, 213:77, 1996.

[EAN96] M. D. Ediger, C. A. Angell, and S. R. Nagel. *J. Phys. Chem.*, 100:13200, 1996.

[Fer50] J. D. Ferry. *J. Am. Chem. Soc.*, 72:3746, 1950.

[FFG+97] T. Franosch, M. Fuchs, W. Götze, M. R. Mayr, and A. P. Singh. *Phys. Rev. E*, 55:7153, 1997.

[FGSF92] F. Fujara, B. Geil, H. Sillescu, and G. Fleischer. *Z. Phys. B*, 88:195, 1992.

[FPB99] H. Franz, W. Petry, and A. Q. R. Baron. *Hyp. Int.*, 123/124:865, 1999.

[FS65] H. Frauenfelder and R. M. Steffen. Chapter xix. In K. Siegbahn, editor, *Alpha-, Beta- and Gamma-Ray Spectroscopy.* North-Holland, 1965.

[FZB00] *Proceedings of the International Workshop on Dynamics in Confinement.* edited by B. Frick, R. Zorn and H. Büttner, J. Phys. IV Colloq. France, **10**, Pr7 (2000).

[GH68] V. I. Goldanskii and R. H. Herber, editors. *Chemical Applications of Mössbauer spectroscopy.* Academic Press, 1968.

[GHL+98] A. Gahl, M. Hillberg, F. J. Litterst, T. Pöhlmann, O. Nuyken, F. Garwe, M. Beiner, and E. Donth. *J. Phys.:Condens. Matter*, 10:961, 1998.

[GLT78] P. Gütlich, R. Link, and A. Trautwein. *Mössbauer Spectroscopy and Transition Metal Chemistry*. Springer-Verlag, 1978.

[Gol69] M. Goldstein. *J. Chem. Phys.*, 51:3728, 1969.

[Göt99] W. Götze. *J. Phys.: Condens. Matter*, 11:A1, 1999.

[GRW+85] E. Gerdau, R. Rüffer, H. Winkler, W. Tolksdorf, C. P. Klages, and J. P. Hannon. *Phys. Rev. Lett.*, 54:835, 1985.

[GS92] W. Götze and L. Sjögren. *Rep. Prog. Phys.*, 55:241, 1992.

[GSV00] W. Götze, A. P. Singh, and Th. Voigtmann. *Phys. Rev. E*, 61:6934, 2000.

[HRBL69] C. Hohenemser, R. Reno, H. C. Benski, and J. Lehr. *Phys. Rev.*, 184:298, 1969.

[HSvB+91] J. B. Hastings, D. P. Siddons, U. van Bürck, R. Hollatz, and U. Bergmann. *Phys. Rev. Lett.*, 66:770, 1991.

[HT99] J. P. Hannon and G. T. Trammell. *Hyp. Int.*, 123/124:127, 1999.

[Iol96] E. M. Iolin. *Hyp. Int. (C)*, 1:513, 1996.

[Iva64] E. N. Ivanov. *Sov. Phys. JETP*, 18:1041, 1964.

[IYI+92] T. Ishikawa, Y. Yoda, K. Izumi, C. K. Suzuki, X. W. Zhang, and M. Ando. *Rev. Sci. Instr.*, 63:1015, 1992.

[JG70] G. P. Johari and M. Goldstein. *J. Chem. Phys.*, 53:2372, 1970.

[JM91] C. L. Jackson and G. B. McKenna. *J. Non-Cryst. Solids*, 131-133:221, 1991.

[Joh73] G. P. Johari. *J. Chem. Phys.*, 58:1766, 1973.

[Kag99] Yu. Kagan. *Hyp. Int.*, 123/124:83, 1999.

[KAK79] Yu. Kagan, A. M. Afanas'ev, and V. G. Kohn. *J. Phys. C*, 12:615, 1979.

[Kau48] W. Kauzmann. *Chem. Rev.*, 43:219, 1948.

[KF01] V. Krishnan and M. Feth. Unpublished.

[KGNP90] Yu. E. Krupyanskii, V. I. Goldanskii, G. U. Nienhaus, and F. Parak. *Hyp. Int.*, 53:59, 1990.

[Koh47] R. Kohlrausch. *Ann. Phys.(Leipzig)*, 12:393, 1847.

[Kop94] M. Kopcewicz. *Encyclopedia of Applied Physics*, chapter Mössbauer effect. VCH Publishers, 1994.

[KS98] V. G. Kohn and G. V. Smirnov. *Phys. Rev. B*, 57:5788, 1998.

[KS99] V. G. Kohn and G. V. Smirnov. *Hyp. Int.*, 123/124:327, 1999.

[LB71] R. M. Lynden-Bell. *Mol. Phys.*, 21:891, 1971.

[LB73] R. M. Lynden-Bell. *Mol. Phys.*, 26:979, 1973.

[Leu84] E. Leutheusser. *Phys. Rev. A*, 29:2765, 1984.

[LFC02] L. Liu, A. Faraone, and S.-H. Chen. *Phys. Rev. E*, 65:041506, 2002.

[LRK77] F. J. Litterst, R. Ramisch, and G. M. Kalvius. *J. Non-Cryst. Solids*, 24:19, 1977.

[LW99] O. Leupold and H. Winkler. *Hyp. Int.*, 123/124:571, 1999.

[Mah89] H.-E. Mahnke. *Hyp. Int.*, 49:77, 1989.

[MFW+97] A. Meyer, H. Franz, J. Wuttke, W. Petry, N. Wiele, R. Rüffer, and C. Hübsch. *Z. Phys. B*, 103:479, 1997.

[Mös58] R. Mössbauer. *Z. Phys.*, 151:124, 1958

[NFP91] G. U. Nienhaus, H. Frauenfelder, and F. Parak. *Phys. Rev. B*, 43:3345, 1991.

[PBF+91] W. Petry, E. Bartsch, F. Fujara, M. Kiebel, H. Sillescu, and B. Farago. *Z. Phys. B*, 83:175, 1991.

[RC96] R. Rüffer and A. I. Chumakov. *Hyp. Int.*, 97/98:589, 1996.

[Rös90] E. Rössler. *J. Chem. Phys.*, 92:3725, 1990.

[Rub74] S. L. Ruby. *J. Phys.*, 35:C6–209, 1974.

[RZF76] S. L. Ruby, B. J. Zabransky, and P. A. Flinn. *J. Phisique*, 37:C6–745, 1976.

[SA75] R. M. Steffen and K. Alder. Chapters 12,13. In W. D. Hamilton, editor, *Electromagnetic Interactions in Nuclear Spectroscopy*. North-Holland, 1975.

[SF64] R. M. Steffen and H. Frauenfelder. Chapter i. In E. Karlsson, E. Matthias, and K. Siegbahn, editors, *Perturbed Angular Correlations*. North-Holland, 1964.

[SFA+02] I. Sergueev, H. Franz, T. Asthalter, W. Petry, U. van Bürck, and G. V. Smirnov. *Phys. Rev. B*, 66:184210, 2002.

[SFS92] W. Schnauss, F. Fujara, and H. Sillescu. *J. Chem. Phys.*, 97:1378, 1992.

[Shv99a] Y. V. Shvyd'ko. *Phys. Rev. B*, 59:9132, 1999.

[Shv99b] Y. V. Shvyd'ko. *Hyp. Int.*, 123/124:275, 1999.

[Sil71] H. Sillescu. *J. Chem. Phys.*, 54:2110, 1971.

[SK68] H. Sillescu and D. Kivelson. *J. Chem. Phys.*, 48:3493, 1968.

[SK95] G. V. Smirnov and V. G. Kohn. *Phys. Rev. B*, 52:3356, 1995.

[SK99] W. Sturhahn and V. G. Kohn. *Hyp. Int.*, 123/124:367, 1999.

[SKP01] G. V. Smirnov, V. G. Kohn, and W. Petry. *Phys. Rev. B*, 63:144303, 2001.

[Smi86] G. V. Smirnov. *Hyp. Int.*, 27:203, 1986.

[SMRF94] J. Schüller, Yu. B. Mel'nichenko, R. Richert, and E. W. Fischer. *Phys. Rev. Lett.*, 73:2224, 1994.

[SQTA96] W. Sturhahn, K. W. Quast, T. S. Toellner, and E. E. Alp. *Phys. Rev. B*, 53:171, 1996.

[SS60] K. S. Singwi and A. Sjölander. *Phys. Rev.*, 120:1093, 1960.

[STA+95] W. Sturhahn, T. S. Toellner, E. E. Alp, X. W. Zhang, M. Ando, Y. Yoda, S. Kikuta, M. Seto, C. W. Kimball, and B. Dabrowski. *Phys. Rev. Lett.*, 74:3832, 1995.

[SYK+95] M. Seto, Y. Yoda, S. Kikuta, X. W. Zhang, and M. Ando. *Phys. Rev. Lett.*, 74:3828, 1995.

[TH78] G. T. Trammell and J. P. Hannon. *Phys. Rev. B*, 18:165, 1978.

[TSWF97] A. Tölle, H. Schober, J. Wuttke, and F. Fujara. *Phys. Rev. E*, 56:809, 1997.

[TW99] A. X. Trautwein and H. Winkler. *Hyp. Int.*, 123/124:561, 1999.

[vB99] U. van Bürck. *Hyp. Int.*, 123/124:483, 1999.

[vBSH+92] U. van Bürck, D. P. Siddons, J. B. Hastings, U. Bergmann, and R. Hollatz. *Phys. Rev. B*, 46:6207, 1992.

[VF80] A. Vasquez and P. A. Flinn. *J. Chem. Phys.*, 72:1958, 1980.

[vH54] L. van Hove. *Phys. Rev.*, 95:249, 1954.

[vK81] N. G. van Kampen. *Stochastic Processes in Physics and Chemistry.* North-Holland, 1981.

[VS99] G. Vogl and B. Sepiol. *Hyp. Int.*, 123/124:595, 1999.

[WA76] J. Wong and C. A. Angell. *Glass: structure by spectroscopy.* Marcel Dekker, 1976.

[WBM69] R. Weiler, S. Blaser, and P. B. Macedo. *J. Phys. Chem.*, 73:4147, 1969.

[WG73] H. Winkler and E. Gerdau. *Z. Physik*, 262:363, 1973.

[Win76] H. Winkler. *Z. Physik A*, 276:225, 1976.

[Wu91] L. Wu. *Phys. Rev. B*, 43:9906, 1991.

[ZRFM03] V. Zöllmer, K. Rätzke, F. Faupel, and A. Meyer. *Phys. Rev. Lett.*, 90:195502, 2003.

Acknowledgments

I thank all persons who have supported me during this thesis work.

I would like first of all to thank Prof. Winfried Petry who made this thesis possible. He has invited me to the TU München, gave me the freedom to develop my own ideas and was ready always to discuss them.

I am very grateful to Dr. Uwe van Bürck who supervised me during the last two years of my thesis. He made a huge contribution to this work. A lot of questions was solved during our discussions and I really enjoyed the teamwork with him. I also would like to thank him for the enormous job in correction of this thesis.

I thank Dr. Sasha Chumakov who also strongly contributed to this thesis. The experiments presented here would have been impossible without his help. Also, many of the ideas presented here were born during our "fresh air" brainstorms.

I would like to thank Dr. Tanja Asthalter, who supervised me during the first two years of my PhD study and introduced me into the technical and operational aspects of the beamline. Also I thank her for the reading and correction of this thesis.

I want to express my gratitude to Dr. Rudolf Rüffer, who hosted me in his group at the ESRF and provided in-house beamtime to perform the experiments. Also I appreciated the beautiful atmosphere in the group created by Dr. Alessandro Barla, Dr. Bryan Doyle, Dr. Hans-Christian Wille, Dr. Helge Thieß, Thomas Roth, Jean-Philippe Celse and other former and present colleagues. Especially, I would like to thank Dr. Olaf Leupold for many discussions and for help at any time.

I thank Dr. Hermann Franz for the possibility to perfom experiments at Petra I and for many useful remarks. I also would like to thank Kirill Messel and Gerd Wellenreuther who participated in some of the experiments presented here.

Special thanks I would like to give to Prof. Gennadii V. Smirnov and Dr. Valentin G. Semenov who helped me to come to Munich and were always ready for discussion and help.

Several discussions with Prof. S. Dattagupta have been useful to clarify theoretical aspects of this work. I also thank him for the preliminary reading of this manuscript.

Thanks to Dr. P. Härter, Dr. H. Schottenberger and Dr. A. Huwe for the preparation

of the samples.

I would like also to thank my colleagues in E13, especially Dr. Nils Wiele, Dr. Walter Schirmacher, Dr. Joachim Wuttke and Dr. Andreas Meyer for interesting and useful discussions.

I would like to thank Edith Lubitz and Elke Fehsenfeld who helped me to s olve many administrative problems.

I would like to thank my family and especially my father. His words that Mössbauer spectroscopy is impossible in liquids became the starting point of this work.

Finally thanks to Anja for the encouragement and patience, especially during the last few months of this work.